BIOPRINTING CELL LADEN STRUCTURES WITH CHITOSAN-GELATIN FOR NEURAL TISSUE APPLICATIONS

By
KEVIN D. ROEHM
Bachelor of Science in Biosystems Engineering
Oklahoma State University
Stillwater, Oklahoma
2013

Master of Science in Chemical Engineering
Oklahoma State University
Stillwater, Oklahoma
2014

Submitted to the Faculty of the
Graduate College of the
Oklahoma State University
in partial fulfillment of
the requirements for
the Degree of
DOCTOR OF PHILOSOPHY
July, 2018

BIOPRINTING CELL LADEN STRUCTURES WITH

CHITOSAN-GELATIN FOR NEURAL

TISSUE APPLICATIONS

Dissertation Approved:

Dr. Sundar Madihally

Dissertation Adviser

Dr. Yu Feng

Dr. James Smay

Dr. Kenneth Miller

ACKNOWLEDGEMENTS

I would like to express my heartfelt thanks to Dr. Sundar Madihally, who has always been available to discuss my research, helped me keep the bigger picture in mind, and infused me with enthusiasm. He has been instrumental in my growth as a researcher, and as a person. I would also like to thank Dr. Jim Smay, Dr. Yu Feng, and Dr. Ken Miller for their insight and for graciously agreeing to be on my committee. This document has been enhanced thanks to their involvement. I want to thank my wife Andrea, as well as the many family and friends that have supported me throughout my Ph.D. I also want to thank my current and former lab mates Dr. Jimmy Walker, Dr. Lukasz Witek, Dr. Carrie German, Dr. Jose Tormos, Tina Al Attar, Ben Strickfaden, and David Ede for their insights and assistance.

In addition, I would like to thank Jeff and Mike at Maker's Tool Works for generously gifting me the 3D printer and assisting with the first print head design and manufacturing. I would also like to thank Dr. Peter Clark and Dr. Mehdi Habibpour for their insight into and assistance with rheological studies. In addition, my generous thanks go to Eileen Nelson for proof reading much of my work, for handling so many exams and homework, and for the many other ways in which she has supported myself, and continues to support all of the chemical engineering graduate students at OSU. I also thank Carolyn Sanders for assistance and advise on purchasing and invoicing, especially when items got lost in the mail, Shelley Potter for safety advice and the loan of a multitude of tools, and Paula Kendrick for mentoring me through my first experience interviewing candidates for a position. Finally, I would like to thank the Oklahoma Center for Advancement of Science and Technology (HR15-142), the Edward Joullian Endowment for funding, and the OSU graduate and professional student government for awarding me travel grants to present my research.

Name: KEVIN D. ROEHM

Date of Degree: JULY 2018

Title of Study: BIOPRINTING CELL LADEN STRUCTURES WITH CHITOSAN GELATIN FOR NEURAL TISSUE APPLICATIONS

Major Field: CHEMICAL ENGINEERING

Abstract: Nearly 1 billion people suffering from neurological disorders and approximately 400,000 patients require surgical intervention to repair damaged peripheral nerves every year. There is a need, therefore, for three-dimensional synthetic tissues to serve as both models and regenerative structures. Primary human neural cells are not directly obtainable. Differentiated, patient specific adult adipocyte stem cells would offer a non-immunogenic, abundant source of cells for regenerative implant applications and in vitro models. However, mature, differentiated cells are difficult to obtain reproducibly. Bioprinting is an attractive approach to building 3D tissues. However, bioinks that transform into stable solids in physiologically conducive environments are needed. Also, cell survival post-printing is an issue, and printing processes effect on cell responses need to be investigated. I developed a preparation process that allows for continuous, consistent printing of a chitosan-gelatin (CG) hydrogel that does not require post-processing. I investigated the effect of print bed temperature, feed rate, flow rate, and needle height on fiber sizes. Further, I designed and developed a compact electrical stimulation device to investigate cell response post-printing. I used computer modeling to ensure I obtained a constant electrical field, similar to traditional devices. Using the developed device, I investigated the response and expression of β-III-tubulin of human neuroblasts (NBs) and human adipocyte stem cells (hASCs) to electrical stimulation and to the bioprinting process, separately and in combination. The CG hydrogel was successfully bioprintined: the bed temperature had the greatest effect on fiber size (resolution), followed by feed rate and cells were well distributed when printed, maintained viability, and no contamination was observed after 5 days. A compact device was designed with a constant electric field that could be maintained sterile during microscopic observation for 6 days post-stimulation. Both NBs and hASCs showed differentiation towards a neural lineage when electrically stimulated. NBs were more sensitive to the printing process than hASCs losing actin polymerization when printed through a 34g needle. Finally, hASCs exhibit significant β-III-tubulin and neuron-like cell morphology 6-days after printing through a 34g needle.

TABLE OF CONTENTS

Chapter Page

Chapter Page

LIST OF TABLES

Table Page

LIST OF FIGURES

Figure Page

CHAPTER I

INTRODUCTION

An estimated 1 billion people suffer from neurological disorders [1] and cost the US nearly $800 billion US a year (adjusted to 2014 dollars) [2]. While work has long been conducted in animal models [3] and in two-dimensional *in vitro* culture models, there is a need for more complex and relevant tools [4-6] to study diseases including Alzheimer's, Parkinson's, and debilitating conditions, such as migraines. In addition, there are an estimated 400,000 procedures to repair peripheral nerve damage each year [7], and neural tissue has very little repair capability. Combined there is a significant need for synthetic, 3D tissues utilizing human cells for both *in vitro* models and regenerative applications.

Neural cells are terminally differentiated, and are non-proliferative. For many years, sources of neural cells for study of physiology, disease, or drug effects were limited to, cancerous neural precursors, and fetal animal ganglia. Both sources have limited relevance to normal human neurons and are unsuited to neural regeneration applications. Human stem cells, especially human adult stem cells from patients suffering from these diseases, offer the only avenue for the creation of *ex vivo* models to study these diseases and are currently being used for this purpose to determine pathways and therefore potential therapeutic molecules to influence these pathways [8]. However, in addition to difficulty obtaining mature cells, there is a lack of

reproducibility of these results. This lack could be attributed to multiple factors including the influence of 3D space, and difficulty scaling these systems to clinical settings.

In combination with differentiated stem cells, bioprinting cells is seen as an attractive approach to spatially locate multiple cell types and build 3D tissues, such as nerves, layer-by-layer. To accomplish this, cells are suspended in biomaterials, which are used as inks to write on various surfaces [9-11]. Moreover, by spatially depositing cell laden inks layer-by-layer, bioprinting can create reproducible structures. A variety of bioprinting technologies have been explored. Among explored bioprinting technologies, microextrusion bioprinters which extrude viscous polymeric solutions (up to $6x10^7$cP) using a mechanical or pneumatic system, are popular [12-16]. Many open-source software packages are available that can be used to render 3D designs into forms that can be interpreted by the printers [17]. Since seeding cells post-printing would limit the precision of placing different cell types in the required spatiotemporal location [18], bioprinting incorporating cells into the printing process is of significant interest. However, a major caveat is the lack of biocompatible inks which transform into mechanically stable solids in physiologically conducive environments [19]. In addition, cell survival post-printing is an issue. This issue is attributed to unfavorable printing conditions such as solvents and other gelation mechanisms required to mechanically stabilize gels, printing temperature, and shear stresses [20, 21]. Current hydrogel inks need crosslinking agents (ultraviolet, pH or chemical) to gel (transition from liquid to solid). I propose using, chitosan-gelatin -β-glycerophosphate (2GP) hydrogels, which exhibit thermogelation at physiological temperature (gelation occurs when the temperature is increased to 37 °C. My work focuses on exploring the printability and obtainable resolution of a hydrogel that has a unique gelation mechanism and does not require post-processing. Further, I explore the effect of the bioprinting processes on cellular response to electrical stimulus using two different cell types and a compact device. Cells respond more drastically to electrical stimulus; these responses would be

much less evident in the presence of a chemical stimulus. To examine cell electrical stimulus response, I developed a compact device to maintain sterility during observation while isolating the electrodes from culture medium. These activities are grouped into three specific aims.

1.1 Aim 1: Create a Bioprinting Process for Chitosan-Gelatin-β-glycerophosphate Thermogelling Hydrogel

The goal of this aim was to evaluate the printability of the chitosan-gelatin-β-glycerophosphate hydrogel and the effect of printing on cell viability using a low cost microextrusion printer. Towards this, I investigated i) the effect of concentration of chitosan-gelatin on gelation characteristics, ii) solution preparation steps (centrifugation, mixing, and degassing) on printability and fiber formation, iii) the print bed temperature profiles via IR imaging and grid-based assessment using thermocouples, iv) the effect of feed rate (10 to 480 cm/min), flow rate (15 to 60 μL/min) and needle height (70 to 280μm) on fiber size and characteristics, and v) the distribution of neuroblasts in printed fibers, and the viability after five days in culture. I used agarose gel to create uniform print surfaces to maintain a constant gap with the needle tip. These results showed that degassing the solution, and precooling the solution was necessary for obtaining continuous fibers. Fiber size decreased from 760μm to 243μm as the feed rate increased from 10cm/min to 100cm/min. Bed temperature played the greatest role in fiber size, followed by feed rate. Cells were well distributed within the fibers and exhibited excellent viability and no contamination after 5 days. Findings are described in Chapter III in detail.

1.2 Aim 2: Develop a Compact Electric Stimulation Device and Test the Response of Neuroblasts and Human Adipocyte Stem Cells

The goal of this aim was to develop and validate a compact electrical stimulation device to assess alterations in cell responses to electric fields, similar to traditional devices [22-24]. Three criteria

were used in designing a galvanotaxis device: i) obtaining a constant EF so that all cells are subjected to the same stimulus; ii) isolating ionic products generated by the electrodes; and iii) increasing portability while maintaining sterility. I constrained the overall device dimensions to match the footprint of a standard microscope slide (75mm long×25 mm wide, and, 13mm height) so that the device is compatible with inverted microscopes. I tested devices with and without physical barriers separating the electrodes from cell culture area, two type of electrodes i.e., point electrodes and disk electrodes, and location of the disk electrode on electrical field. These designs were first generated in SolidWorks and then imported into COMSOL simulation to evaluate electrical field distribution. The same design was imported into a 3D printer for manufacturing of the device. Based on these analyses, I selected one device for examining whether neuroblasts would respond similar to other neural cells when stimulated by exhibiting morphological alignment or galvanotaxis [23]. Neuroblasts cells were seeded on gelatin coated glass coverslips one or six days prior to electrical stimulation. Cell area, shape factor (circularity), major length, minor length, and cell height were determined to quantify morphological changes. The field effect was evaluated on human adipocyte stem cells (hASCs) to determine the response of a clinically relevant cell type. Further, some have demonstrated that stimulating cells with an electric field can result in adult stem cell differentiation towards a neural lineage [25, 26]. Therefore, in addition to evaluating morphological changes, I stained some samples for the nucleus with DAPI, for actin with phalloidin, and for β-III-tubulin with TUJ1 clone anti-β-III-tubulin antigen to understand potential differentiation of both the NB and hASCs towards a neural lineage. Findings from these studies are described in Chapter IV.

1.3 Aim 3: Evaluate the Effect of Bioprinting and Electrical Stimulation Separately and Jointly on NBs and hASCs

The goal of this aim was to evaluate the combined and separate effect of bioprinting and electrical stimulation on NB and hASC response. Towards this, I investigated morphological changes of

NBs and hASCs printed in: i) in medium through a 34g (60 μm internal diameter) or 32g needle (120 μm internal diameter) and ii) mixed into chitosan-gelatin hydrogel. I also evaluated the conductive properties of the hydrogel to understand changes it could induce in the electrical field. Printing conditions were selected from aim 1. Further, I evaluated changes in morphology of NBs stimulated 6 days post printing and hASCs stimulated 1 day after printing, concurrent with aim 2 results (Chapter IV). Cell area, shape factor (circularity), major length, minor length, and cell height were determined to quantify morphological changes. In addition, cells were stained for the nucleus with DAPI, for actin with phalloidin, and for β-III-tubulin with TUJ1 clone anti-β-III-tubulin antigen to understand potential differentiation of both the NBs and hASCs towards a neural lineage and whether the printing process, electrical stimulation, or both altered expression of β-III-tubulin, which would indicate a difference in differentiation. I cultured these cells up to six days post-printing and show that printed hASCs differentiate towards neurons using beta-III tubulin and actin. These cells showed an increase in beta-III tubulin expression when analyzed immediately after printing and when cultured an additional 6-days. Findings from these studies are described in Chapter V.

1.4 Summary

This investigation focused on evaluating a novel bioprinter ink with a unique gelation mechanism. I demonstrated that multi-level structures can be printed from cell laden CG hydrogels. Further, I evaluated and demonstrated that the temperature and gelation of the hydrogel had the greatest effect on fiber size. These results give needed insight into a previously unexplored gelation mechanism: irreversible thermal gelation with increasing temperature and some of the challenges and advantages of printing hydrogels with this gelation mechanism. In addition, I find that culture time affects cell response differently. Also, I find that hASCs may differentiate toward a neural lineage with electrical stimulation but that the short term shear stress experienced during bioprinting with 6-day culture significantly increases β-III-tubulin expression. This indicates that bioprinting might

be leveraged for neural differentiation. These results emphasize the need to evaluate bioprinting process effects on cell response and expression to give a more complete picture of the processes' effects, beyond cell viability. Moreover, these results provide insight into culture time as a factor that should be accounted for in stem cell differentiation protocols. Eventually bioprinting may enable the creation of functional 3D pseudo-tissues with spatially controlled multicellular placement. These tissues could be used for regeneration, as in the case of neural damage that requires grafting and exploration of diseases and potential treatments, possibly on a patient-by-patient basis, for personalized medicine.

CHAPTER II

BACKGROUND

2.1 Tissue Engineering

Tissue engineering seeks to create synthetic tissues by combining patient cells, typically stem cells from a patient, with scaffolds, structures that impart a three-dimensional, relevant geometry, as well as cues for differentiation and growth, sufficient porosity for cellular infiltration, and cell binding domains for those cells to attach to the scaffold. Over time, as cells deposit extra cellular matrix (ECM), the scaffold degrades and is replaced by ECM. At the end of the process, a tissue is comprised of cells and their generated ECM. Scaffolds must also be biocompatible and have mechanical properties sufficient to the stresses they experience during and after implantation.

Moreover, tissue engineering requires stem cells to create complex tissues and organs. Since many cell types are terminally differentiated, small samples cannot be expanded into useful cell numbers. However, stem cells are pluripotent progenitors. With careful culturing, autologous adult stem cells can be expanded to useful numbers and then differentiated into non-replicating cell types.

Therefore, tissue engineering requires both 3D scaffolds to guide cell growth, and well understood methods to obtain specific cell types from adult stem cells. This work describes the evaluation of a new ink for the creation of these scaffolds and describes the effect the printing process has on cells, including differentiation of human adipocyte stem cells, and changes in cell response post printing. The work demonstrates the utility of a previously unexplored ink for bioprinting, one that utilizes

a previously unutilized gelation method. Further this work explores a novel compact electrical stimulation device and demonstrates the printing process itself can be used to cause stem cell differentiation towards a neural cell linage, and affects cell response to electrical stimulation.

2.1.1 Pre-made Scaffolds and Their Limitations

Many pre-made scaffolds have been investigated and used clinically. These scaffolds are either naturally derived, from decellularized xenogeneic or allogenic sources, produced from synthetic polymers, or some combination of the two. Scaffolds derived from porcine small intestine submucosa and dermis from human, porcine, and bovine sources are clinically available [27]. In multiple cases, decellularized cadaver tissue has also been used as grafts. These scaffolds are either seeded exogenously by introducing suspended cells to the scaffold, or implanted without seeding. This allows the endogenous cell population to infiltrate and remodel the tissue post-implantation.

Most pre-made scaffolds are limited by homogeneity of the source tissue and thickness. My master's thesis work focused on the development of a scaffold from porcine adipose tissue that maintained the source tissue's inherent vascular network. Prepared acellular scaffolds, as well as those available clinically, are flat sheets. Forming them into specific geometries is difficult and time consuming, requiring a surgeon to suture them into the desired shape; this affects the reliability and quality of the regenerated tissue.

Pre-made scaffolds have been shown to aid in functional peripheral nerve restoration. Several scaffolds from natural polymers, such as collagen, and decellularized nerve tissue have been FDA approved for clinical use [28]. These guides are promising and can repair gaps up to 2 cm by protecting the nerve tissue from undesirable cell infiltration and providing guidance to the regenerating nerve [29]. However, there is a need for guides that can repair longer gaps. Pre-conditioning of scaffolds for nerve guides [30], utilizing Schwann cells combined with external mechanical stimulus to pre-align the support-cells [31], and utilizing scaffolds with growth factors and other

assistive molecules [32] have been investigated. More recently, it has been shown that nerve guides with multiple micro-channels provide better outcomes: micro-channels are on the correct scale to provide mechanical cues to cells, similar to micro-patterning while also reducing unwanted responses, such as inflammation. Producing these scaffolds with the proper size architecture is difficult and has required new 3D bioprinting technologies [33].

2.2 Three-Dimensional Printing

As it has for other industries, 3D printing has drawn significant interest as a method of precisely and economically controlling scaffold geometry. Significant research has investigated producing scaffolds from synthetic polymers, ceramics (specifically for bone), and even metals. Using data obtained from magnetic resonance imaging (MRI) or computed tomography (CT) scanning, a detailed, three-dimensional model of a patient's bone can be created and used to produce a scaffold that precisely fits each, individual patient. This is known as personalized medicine—people are so varied that a 'one size fits all' solution often falls far short of the optimum solution. Therefore, using technologies, such as 3D printing, which can quickly and precisely produce patient specific solutions is of significant interest.

2.2.1 3D Printer Hardware

There are two basic types of 3D printers. The first deposits material onto a bed through a print head. The second type selectively solidifies material contained in a container from which the final part is removed. All printers have common elements. First, a microprocessor is required; it must be able to take a set of instructions and correctly control the various parts of the printer. Second, printers require motors to direct the material or solidifying agent in the x and y directions and a motorized system to sequentially move in the Z direction to create additional layers. Additionally, using electric heating coils to control material temperature is very common.

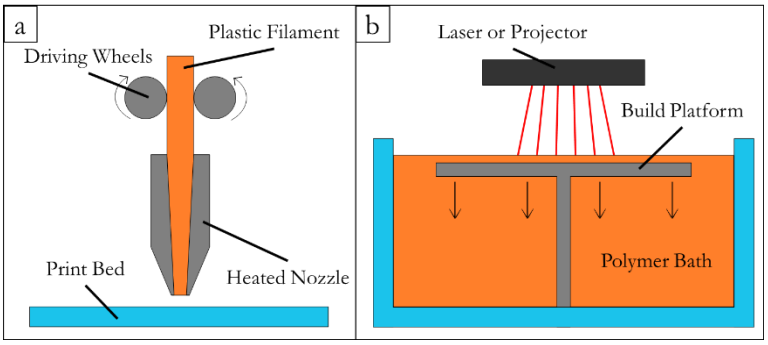

Figure 2.1: Illustrations of 3D Printers. Diagrams of (a) a FDM printer and (b) a SLA printer

Fused deposition modeling (FDM) is an example of the first type and is the most common 3D printing technology due to inexpensive platforms and material. An FDM printer consists of a heated nozzle mounted to a motion platform that controls movement of the nozzle with respect to a build plate. Plastic, typically acrylonitrile butadiene styrene (ABS) or polylactic acid (PLA), is fed from a spool, melted by the nozzle, and deposited on to the build plate in specified patterns, creating a part from the bottom up layer-by-layer (**Figure 2.1**a). FDM is the least expensive technology; many do-it-yourself kits exist allowing enthusiasts to build printers for under $1,000 [34]. The expense and availability of FDM has catalyzed a thriving enthusiast community and the creation of numerous open source tools and printer designs.

Stereolithography (SLA) is an example of the second type of printer. It was the first commercially available 3D printing technology (produced by 3D Systems in 1986). SLA uses a photo initiator, either a laser or projector to photolitically crosslink a liquid polymer contained within a bath (**Figure 2.1b**). After each layer is hardened, it is either pulled down into the bath or up out of it, depending on the location of the light source. Unlike FDM, SLA, and other printers of this second type, cannot print parts with hollow, enclosed spaces without encapsulating unhardened material. In addition, although SLA printer costs have decreased, they are still costly enough to be limited to commercial applications, partly because of the initial printer cost but mostly due to the cost of the proprietary liquid polymers required. However, SLA offers very high resolution (which I define as the smallest feature that can be reproduced). Finally, like FDM, SLA printers are slow, usually

because a wiper must spread the liquid across the part each time it is drawn further into the bath. However, an exciting new development in SLA technology, called continuous liquid interface production (CLIP), has demonstrated vastly greater production speed than previous methods by utilizing a polymer with an oxygen inhibited photo polymerization reaction and an oxygen permeable, optically transparent window in the bottom of the bath. This window prevents adhesion of cured polymer to itself, allowing the part to be built at the bottom of the liquid well and raised out of it [35].

Selective laser sintering (SLS) is another example of the second type of printer. It uses a high powered laser to melt metal powder, fusing the particles into the desired form. The particles are held in a container and a wiper spreads a new layer of particles over the part after each layer is completed and the part is pulled down into the container. SLS is the only widely used technology that can print metals such as steel and aluminum. However, SLS is one of the most expensive 3D printing technologies.

2.2.2 Controlling a printer with G-Code

The multi axis motion platform used by most open source printers, utilizes a machine instruction language created for automated mills and lathes. Called G-Code, the language was originally developed in the 1950s for machine tool computer control. As CNC mills and lathes have many similarities to 3D printers, this language have been adapted for 3D printing [34]. In the course of using a 3D printer, the user will rarely, if ever, actually see or write G-Code. Instead, a 3D model is typically converted into G-Code by an accompanying piece of software called a slicer. Slicers generate a series of linear interpolation commands (G1 commands) that move the print head in the X and Y axis to deposit the required material for each layer. The G1 command requires a point (given by Cartesian coordinate values X, Y, and Z), an extrusion parameter (E), a feed rate (F), and an end stop check command (S), in the form G1 X Y Z E F S. The command will move the print head, called the extruder, along the linear path between its current position and the specified point.

Feed rate is a term adopted from milling where it describes the rate material is fed into the milling head. In the case of 3D printers, this parameter is the velocity the extruder moves in relation to the print bed. Extrusion rate on the other hand, is the rate at which material is fed into the extruder as a function of distance. It is a length term, in mm, that specifies the length of filament that will be fed into the extruder between the current position and specified position. Printer commands will typically leave off one or more parameters from movement commands, which indicates no movement in that axis (typically the z axis) or to use the previous value in case of the feed rate. Both the Z and F values are commonly missing from movement commands Z changes only between layers and F changes only for non-printing moves. There are numerous other G-Code commands utilized by 3D printers; some of the most commonly used commands are listed in **Table 2.1.**

Table 2.1: Common G-Code Commands. Parameters are followed by numerical values (i.e. G1 X120 Y15 Z0.01 E2.56 F1000). See [36] for a g-code reference with detailed documentation of many more command parameters

Command	Parameters	Action
;	None	Makes anything to the right of the character on the same line a comment, which is ignored by the printer.
M109	S	Instructs printer to set temperature and wait until temperature is reached before continuing
M82	None	Sets extruder to absolute mode: E values are related to the initial filament position, not the current position
M101	None	Turn extruder on/prepare extruder for printing
G28	None	Home the print head to the origin (X,Y,Z)=(0,0,0)
G90	None	Set printer to absolute positioning: (X,Y,Z) relative to origin instead of current position
G21	None	Set units to millimeters
G20	None	Set units to inches
G92	X Y Z E	Sets the absolute position at the current location (i.e. G92 X0 Y0 Z0 E0 would make the current position the origin).
G1	X Y Z E F S	Straight line move to (X,Y,Z), extrude E mm of material, move at feed rate F, and check for end stop S1=yes S0=no
G2	X Y I J E F	Movement from the current position to (X,Y) along an arc centered at (I,J) clockwise while extruding E mm of material and moving with feed rate F
G3	X Y I J E F	Movement from the current position to (X,Y) along an arc centered at (I,J) counterclockwise while extruding E mm of material and moving with feed rate F

2.2.3 Slicers

Generally, Slicers produce all of the required G-code for printing from 3D models created through a variety of means (**Figure 2.2**). For complex 3D models, slicers are absolutely necessary to generate the code required: **Figure 2.2c** represents almost 250,000 lines of code. Slicers allow the user to change a variety of parameters that affect the printing. Many of these parameters are determined experimentally and vary by material. Parameters which work well for common materials have been found and added into the software to allow users to print good-quality parts without trial-and-error. Other parameters are frequently changed based on desired outcomes. Some important parameters include: 1) How much of the part to infill and with what pattern (e.g. fill 50% of the interior volume with a honeycomb structure). Infill allows parts to be printed faster with less material, however it reduces mechanical strength. Further, it is thought that completely filling the interior (100% infill) improves the water retention of printed parts. 2) The number of Skirts, which are concentric rings printed to establish steady-state flow prior to printing (**Figure2.2b and c**) show skirts around the part). 3) Rafts, which are support material created below a part and can help reduce warping, especially on unheated print beds). 4) Whether or not to use support material, and the angle past which it is required. This is used to tell the program to generate columns to prevent parts that get larger in x and y with z from slumping, and or provide a surface above the build plate on which to print (layers can typically be printed up to 45% degrees without support material).

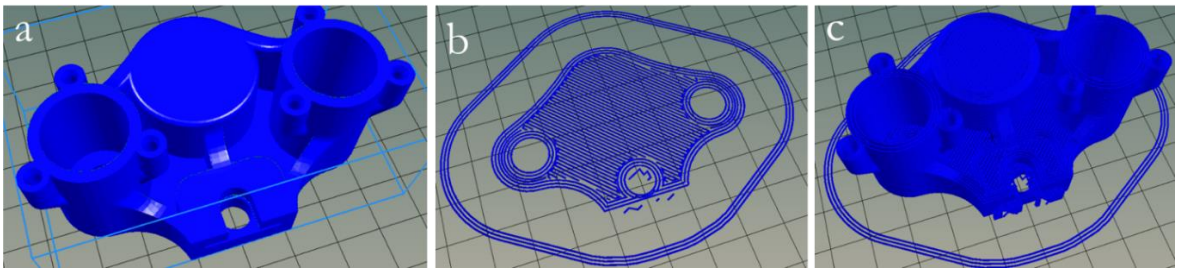

Figure 2.2: Slicing a model. The initial 3D model (a), visual depiction of material deposited for the first layer of the model as described by autogenerated G-Code (b), and a visual representation of the 247,000 lines of G-Code generated to build the part (c).

2.2.4 3D Printing for Medical Applications: Personalized Medicine

3D Printing is being widely explored as an avenue to produce personalized devices. Personalized medicine, the concept of addressing individual patients instead of averages, has been shown to be more effective. While one-on-one solutions have required hand shaping in the past, making them costly, new technologies are making one-on-one personalized medicine a more widely obtainable goal. Instead of either creating uniform devices modeled around an average patient, or hand crafting each device by hand, 3D printing allows existing designs to be modified slightly for each patient or customized designs to be created from CT or MRI scans. Devices have been historically designed around the average adult male. This results in devices suited to most male patients but also tends to result in devices that are poorly suited to women and especially children.

So far, a variety of hand prostheses have been 3D printed, the first 3D printed pill has been approved by the FDA [37], a woman's skull was replaced with a 3D printed implant in the Nederlands [38], and research is ongoing on numerous 3D printed devices and 3D printing platforms. 3D printing has found its way into hospitals to create 3D, graspable organs and tissues for diagnosis and preplanning purposes. Using 3D printed mimics for pre-surgical planning has shown improved outcomes in craniofacial and maxillofacial surgeries, and is being applied to many other surgical procedures [39]. 3D printing has also been widely accepted for dental medicine, especially orthodontics [40]. Medical 3D printing has examined a number of biocompatible polymers including polycaprolactone (PCL) [41] and blends of PCL and poly-lactic-co-glycolic acid (PLGA) [42]. Overall, while 3D printing has had a significant, positive impact on the medical industry, many see significantly greater potential for 3D fabrication technologies that is yet to be achieved.

2.3 Bioprinting

Both endogenous and exogenous cell population of scaffolds is random. Cells infiltrate from the surrounding environment into the scaffold and their arrangement, distribution, and orientation are

either random or factors of the scaffold's properties (i.e. porosity). However, tissue morphologies are non-random and show distinct arrangement. The ability to place multiple-cell types in the same arrangement as natural tissue morphology is expected to lead to more functional tissues. 3D bioprinting is of significant interest as an avenue to accomplish this by adding cells to inks prior to printing.

2.3.1 Bioprinting Technologies: Advantages and Disadvantages

Incorporating cells into the 3D printing process is a significant challenge requiring modifications to 3D printing technologies developed for non-living materials or the creation of new processes. Since cells cannot withstand heating, FDM cannot be used for bioprinting. However, microextrusion printers are a straightforward modification of FDM technology requiring only that the print head be modified to feed a liquid polymers extruded at room temperature and crosslinked using chemicals, UV light, laser, thermal mechanisms, or by taking advantage of shear thinning materials. Modifying a print head requires producing a device to hold a syringe and drive the material. This can be as simple as a mechanical device to drive a syringe plunger or use much more complicated systems, depending on the material [43, 44]. The polymer is extruded using a mechanical or pneumatic system. For pneumatic systems, the polymer can either be continually extruded or sheared into drops using a micro-valve. Droplet printing is often used to print patterns of cells into a substrate where the end result is the injection of cells into an already present material [45-47].

SLA translates directly from traditional printing using cells encapsulated in biocompatible, crosslinkable polymers [48, 49]. SLS systems require photoinitiators and UV light exposure which damages cells. Bryant et al. examined several photoinitiators. Darocur 2959, used to manufacture contact lenses, demonstrated the best cytocompatability with cell viability of 75% compared to control cultures [50]. This viability is lower than other methods, including microextrusion which can demonstrate viabilities near 100% [10]. The greatest advantage offered by SLA is the achievable accuracy. Accuracies as high as 200 nm have been reported [51].

Two dimensional inkjet technology has also been adapted to 3D printing. By replacing the ink with a hydrogel and adding z axis movement to the print head, a commercial inkjet printer can be converted into a bioprinter. This technology requires a crosslinking agent to solidify the printed material and inks must be non-viscous (less than 10 centipoise) prior to expulsion. Moreover, there is concern that the piezoelectric ejection systems used in inkjet printers might severely decrease cell viability. This problem is increased by the difficulty printing high cell density droplets. However, they are attractive because they are inexpensive and fast [52].

The last major technology used in bioprinting is laser assisted bioprinting (LAB). This technology uses two parallel surfaces, the upper surface coated with a layer of gold and a layer of cell containing material. A laser system pulses specific locations on the upper, donor surface. When the light interacts with the gold layer it is vaporized, creating a localized high pressure region which propels the cell containing material onto the receiving surface below (**Figure 2.3**) [53]. LAB printers have a generally low flow rate, are costly, and require changing the donor slide to change cell type or material [52].

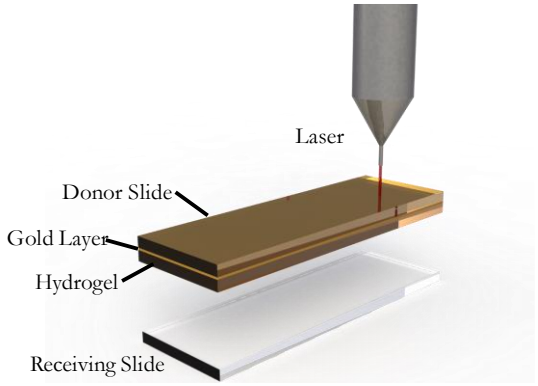

Figure 2.3: Laser Assisted Bioprinting Diagram

2.3.2 Choosing a Microextrusion Bioprinter

Ideally, the bioprinting process must maintain cells at physiological condition throughout the process. As shown in **Table 2.2**, SLS utilizes a bath of polymer crosslinked by UV light, inkjet technology cannot print viscous inks, and while they have excellent precision, LAB printers are costly

and unsuited for large-scale printing. Because of the viscosity of our hydrogel, and to investigate the most economically viable option, I chose to use a microextrusion bioprinter.

Table 2.2: Comparison of Bioprinting Processes

Process	Advantages	Disadvantages
Microextrusion	• Inexpensive • Can handle viscous inks • Open Source Platforms	• Moderate resolution • Slow Print Speed
SLA	• Very Good Resolution • Potentially rapid, printing	• Requires photo crosslinking • Expensive components
Inkjet	• Fast • Inexpensive	• Cannot handle viscous inks
LAB	• Excellent Resolution	• Expensive • Slow • Unsuited to print many layers

2.4 Hydrogels as Inks

In addition to reducing shear stresses and maintaining cells close to physiological norms, bioprinting processes require non-toxic, biocompatible inks that transition from liquid to solid. The phase transition must also be accomplished without killing the cells in the system.

2.4.1 Introduction to Hydrogels

Hydrogels, like tissues, are highly hydrated polymer compounds with unique properties suitable for tissue engineering. Only a fraction of a hydrogel's weight is contributed by the polymer, sometimes as little as 0.1% [54]. The remainder of the hydrogel is water. Their water content makes them highly permeable, allowing nutrients and waste to diffuse easily into and out of the gel. Further, many hydrogels can be prepared as liquid solutions that undergo phase transition through chemical, irradiative, or thermal mechanisms.

2.4.2 Hydrogel Mechanical Properties

Hydrogels can be difficult to handle because they are generally mechanically weak. However, hydrogel mechanical properties are comparable to many soft tissues; mimicking these native mechanical properties leads to the best functional outcome [55]. Our hydrogel's mechanical strength can be tuned to match tissue mechanical properties by varying the concentration of polymer, and adding crosslinking agents such as hyaluronic acid and transglutaminase. Thus far, members of our laboratory have matched our hydrogel to both cartilage [56] and cardiac tissue [57].

2.4.3 Hydrogels in 3D Printing

3D printing using hydrogels is a recent development; however, hydrogels have gained significant interest as bioprinting inks. Early 3D printing results using an alginate hydrogel were published in 2002 [58]. Cells were incorporated into the printing process using hepatocytes incorporated into gelatin crosslinked with glutaraldehyde in 2006 [59]. A literature review suggested sodium alginate is still the most commonly used ink (**Table 2.3**). Cell printed viabilities range from 68% to 92%.

Table 2.3: An overview of microextrusion printing processes investigated in literature.

Print Heads	Nozzle Apparatus	Cells	Ink Material	Viability (%)		Nozzle Diameter (μm)	Ref
				Printed	Control		
4	Custom Nozzle	HepG2 liver cells	Alginate	85±9	—	400	[60]
	Custom Nozzle			68±6	—	150	[60]
1	Coaxial nozzle	Bovine Cartilage Progenitor Cells	Alginate	92	—	730*	[61]
—	3 ml syringe	Human fetal cardiomyocyte progenitor cells	Alginate	92	—		[62]
—	Pneumatic syringe	Mesenchymal Stem Cells (MSCs)	Alginate	~85	—	210-1610	[63]
—	Pneumatic syringe	Bone Marrow Stromal Cells	Alginate	~95	~95	100-450 (fiber diameter)	[64]
—	Syringe pump	—	Crosslinked 75 kDa Alginate	~90	95	28 gauge (180)	[65]
—	—	Porcine aortic valve interstitial cells	Alginate, PEG-DA, gelatin	57-70 @ 6 hr	—	400-1200	[66]
—	1 ml Syringe	HEK 293FT	Gelatin-Alginate	92.25±1.813	—	260	[67]
—	1 ml Syringe	Hela Cells	Gelatin-Alginate	90	—	260	[68]
—	—	Hepatocytes	Gelatin-Chitosan	>98 inside walls	—	—	[69]
6	Syringe	hASCs and hTMSCs	PCL-Decellularized ECM	>95 @ 24 hr	—	—	[70]
4	Nozzle	C3H/10T1/2, Clone 8 cells	Gelatin-Methacrylate	~60±20	~78±18	30-200	[71]
4	Nozzle	GFP human neonatal dermal fibroblasts	Gelatin Methacrylamide	~70±10	~77±15	30-200	[71]

Print Heads	Nozzle Apparatus	Cells	Ink Material	Viability (%)		Nozzle Diameter (μm)	Ref
				Printed	Control		
—	Syringe and needle	HepG2 Liver Cells	Gelatin Methacrylamide	>97 @ <1 bar	—	200	[10]
2	'permanent syringe/capillary'	HEPG2 and NIH3T3	Gelatin Methacrylamide	~91±9	~88±8	500	[72]
4	10 ml syringe	Hepatocytes	HA, Gelatin and atelocollagen	97.8±1.6 @ 4 days	—	—	[42, 73]
—	Custom Nozzle	Osteoblasts and human fibroblasts	Spider Silk Protein	70.1±7.6 @ 48 hr	—	300	[74]

Sodium alginate is chemically cross-linked by calcium ions (Ca^{2+}). Crosslinking is typically accomplished by immersion of the structure in a solution of calcium chloride [60-63, 66]. The best resolution and viability have been reported using alginate with no viability loss extruding mesenchymal stem cells through a 210 μm nozzle [63]. However, calcium is a cell signaling molecule and may cause unwanted changes in functionality [75]. As can be seen in **Table 2.4**, many bioprinting inks require a chemical or irradiative crosslinker. The exception was spider silk protein. However, a 70% viability was reported when extruding through a 300μm nozzle [74], much lower than for alginate results (~100%) [63]

Table 2.4: Gelation mechanisms of investigated Hydrogels.

Material	Gelation Method	Ref(s)
Alginate	Calcium Chloride Solution	[60-66]
Alginate-Gelatin	Calcium Chloride Solution	[67, 68]
Methacrylate Gelatin	Ultraviolet Light	[10, 71, 72]
Chitosan-Gelatin	Sodium Tripolyphosphate snd gluteraldyhyde	[69]
Spider Silk Protein	—	[74]

In addition, some groups seek to use multi-material hybrid bioprinting processes which utilize traditional biocompatible polymers, such as PCL, with hydrogels. In many cases, the hydrogels are not cross-linked since the system's mechanical strength is provided by the polymer [66, 70, 76]. These systems provide the advantages of PCL and of hydrogel systems. Utilizing multiple materials in this manner vastly increases production time as the print head must be switched from hydrogel to PCL on every layer. This hybrid approach is restricted bone tissue engineering because the mechanical properties of PCL are significantly greater than soft-tissue properties.

2.4.4 Our Hydrogel

In contrast, our group has developed a gelatin-chitosan-β-glycerophosphate hydrogel that spontaneously transitions from liquid to solid at physiological temperature. The solution spontaneously forms hydrogels at 37°C [77] Our group has demonstrated unique advantages of chitosan in tissue

engineering: chitosan gelatin hydrogels are conducive for adhesion of various cell types [78, 79]. No post-processing steps are required. Long-term stability and mechanical properties can be tailored by selectively cross-linking gelatin after gelation using transglutaminase [80, 81], and the hydrogel has been shown to be non-immunogenic in a transdermal mouse model.

2.5 External Stimuli for Cellular Alignment

Many cells types have distinct, aligned structures in the body. Nerves, muscles and blood vessels are all examples of tissues with aligned cells. Moreover, cellular alignment in these structures is often crucial to proper cell function. One clear example is vascular smooth muscle cell contraction. These cells contract uniaxially, and therefore must be aligned concentrically around the lumen to cause vasoconstriction. Further, alignment within the cell is important even before the first division of an embryo [82]. In the context of tissue engineering, cellular alignment is effected by flow induced shear stress, micro-patterns, chemical gradients, mechanical stresses, and electrical gradients.

2.5.1 Shear Stress—Reproducing an Endogenous Environment

Reproducing *in vivo* stresses reproduces *in vivo* morphology—endothelial cells have long been known to align in the presence of shear imparted by flow [83]. Similarly, vascular smooth muscle cells align perpendicular to fluid flow [84] and cardiomyocites and their fibers align in the presence of mechanical loading [85]. This produces a more physiologically relevant cell morphology and is usually coupled with positive changes in cytoskeletal arrangement and expression. For example, endothelial cells have been shown to align F-actin stress fibers in the direction of flow [86].

2.5.2 Micro patterns

Cell alignment via micro patterns has been widely investigated. Micro-architecture has been created through a variety of methods. Patterns created with selective ultraviolet gelation of cell laden

photocurable hydrogels using masks has been shown to align encapsulated human umbilical vein endothelial cells, rodent myoblasts, and rodent cardiac side population cells [87], compression molding and solvent casting using silicon templates created with lithographic reactive ion etching [88], and by electrospinning using a rotating collector plate to create aligned fibers [89]. In addition, lithographic techniques have been used to create nanoscale patterns [89]. Many of these techniques combine additional signaling, such as patterning the ECM protein laminin in the microgrooves. Generally, axon alignment is affected more by pattern depth than width [88]. I will also create a hydrogel micro pattern on a coverslip, similar to [87], using bioprinting. That work provides a non-shear example of a similar setup utilizing a different gel. However, the work also found that significant cellular alignment only occurred in hydrogel fibers with widths of 50-100 μm, which needs to be considered. In addition, significant work has been conducted on neural alignment in grooves. Neurites, immature axonal growths typically from 'young' axons isolated from unborn rat pups, tend to align with laminin patterned in grooves [88].

I investigate micro-architecture similar to that of cast, parallel hydrogel fibers through bioprinting. These size of these fibers compared to those investigated by others need to be kept in mind during investigation. It is worth noting that fiber sizes greater than 200 μm failed to elicit alignment from cells in hydrogels [87] and alignment pattern widths are usually in the tens of microns; many bioprinted fibers are well over 200 μm. Therefore, the effect of patterning with a bioprinting may not be significant.

2.5.3 Chemical Patterns and Gradients

As mentioned, patterns of laminin, the second most prevalent protein in the basal lamina (part of the ECM), have been combined with microgrooves to assist in cell alignment. Laminin has also been patterned without microgrooves using various techniques, typically stereolithographic. A microgrooved template created via Stereolithography to localize laminin in a desired pattern and then attaching the protein via solvent (cell culture medium/water) evaporation created laminin gradients

[90]. Inkjet bioprinting technologies have been used to pattern growth factors onto hydrogel surfaces [91]. Many expect that future bioprinting platforms will use multiple technologies—I anticipate the combination of microextrusion to extrude cell-laden hydrogels might be combined with injet printing to pattern growth factor gradients onto printed structures. If this were done in a layer-by-layer manner, with a sufficiently small layer height, the gradient could be user controlled in all three spatial dimensions.

2.5.4 Mechanical Stress

Induced stretch, or uniaxial stress has been shown to align cells. In one case, cells were encapsulated in a hydrogel and then the hydrogel was constrained at two of its ends. It was found that Schwann cells created uniaxial stress in the hydrogel and caused alignment within 12 hours [31]. Others have shown that recreating the cyclical, uniaxial stress similar to that experienced by the heart, aligns cardiomyocytes contained in a hydrogel [85]. Further, cyclical stress causes fibril alignment in a tendon construct [92].

2.5.5 Cell Alignment During Bioprinting

It has been shown that cells align and may differentiate after bioprinting [93]. However, due to the influence of multiple mechanisms, no more in-depth cause has been determined. During the bioprinting process, cells are experiencing shear stresses in the needle that can be many times those experienced by most cells *in vivo*. Cells may also respond to created micropatterns, depending on their width. Finally, adhesion can stretch fibers, possibly inducing a residual axonal prestress caused by the opposing adhesion and cohesion forces within a stretched fiber deposited on a printing platform.

2.5.6 Electrical Stimulation

Electrical stimulation has long been investigated *in vivo* for a variety of neurological clinical applications, including treatment for Parkinson's disease [94]. Moreover, electrical stimulation is

known to drive cell movement (cell movement in response to electrical fields is known as galvanotaxis) for a variety of cell types including neurites, myoblasts, fibroblasts, and epithelial cells [95]. Endogenous electric fields are present during embryonic development and guide cell arrangement and alignment [96]. These fields are also present during wound healing where they direct the orientation and growth of cells [97]. Further, it has been demonstrated that neuronal cells align in the presence of electric fields generated by constant direct current *in vitro* [23].

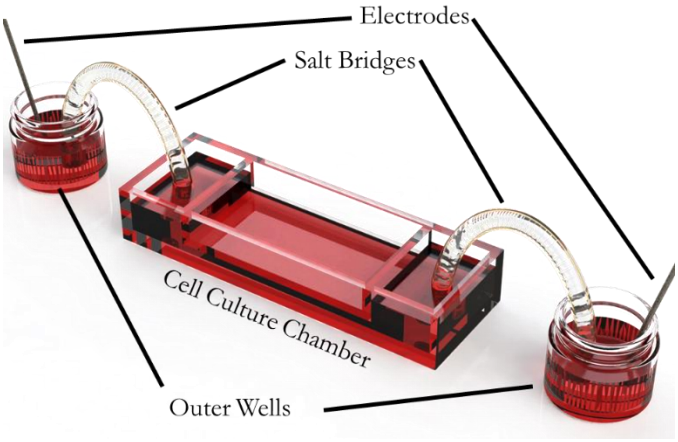

Figure 2.4: A traditional, multicomponent galvanotaxis device. Outer wells isolate electrode products from the cell culture chamber while transmitting current

Traditional devices for *in vitro* electrical stimulation are cumbersome, consisting of electrolyte filled beakers connected to a central cell culture chamber via agar filled tubes (i.e. salt bridges) (**Figure 2.4**). However, they are also relatively easy to produce utilizing typical laboratory glassware and culture dishes (although a custom made central cell chamber is sometimes utilized) [22-24, 98]. In addition to the need for multiple components to isolate the electrodes and their electrochemical products from cells, most of these devices are open to air, making them non-sterile if routine light-microscopic observation is required or they otherwise need to be removed from a sterile hood. This reduces the opportunity for long-term culture.

To overcome the limitations of these traditional devices, many have sought to utilize electrodes placed directly into culture dishes. Platinum electrodes have been used for both *in vivo* and *in vitro* electrical stimulation, are biocompatible, and are available for clinical epilepsy treatment [99, 100].

Moreover, carbon nanofibers [101] and conductive polymers [102] have been used. Since the devices are placed directly in the culture medium, care must be taken to ensure evaluation occurs where the electric field is constant, and not near electrodes where cells would experience significantly different fields [95], and that electrode products do not affect cell response. In this work, I investigate a compact electrical stimulator that miniaturizes the traditional electrical stimulation device while still permitting sterile observation and ease of transportation. Further, I describe a device that is produced by 3D printing, which is increasingly routinely available to laboratories, or can be obtained at low cost.

2.6 Stem Cell Differentiation

Stem cells are cells that have the ability to differentiate into one or more cell types. Increasing understanding of adult stem cell plasticity and the possibility of developing patient-specific, induced pluripotent stem cells has rekindled hope in the development of various tools and therapies relevant to health-care. Moreover, evaluating cellular differentiation *in vitro* has gained significant attention. As mentioned previously, many cells types are terminally differentiated. Not only do they have extremely limited self-repair capability, but these cells are difficult to obtain and culture *in vitro* because they do not divide. Stem cells create the opportunity to obtain these cells for *in vitro* culture studies, opening up a world of investigation previously closed off by the inability to culture these cells. Moreover, especially with neural cells, the only source of human neural cells is from stem cells and has proven to be a powerful tool. For example, utilizing adult cells from patients with and without various neurodegenerative diseases has indicated that a lack of proper neural differentiation may contribute to the disease and has presented a potential therapeutic molecule [8].

While work with pluripotent embryonic stem cells has declined significantly due to ethical concerns, multipotent adult stem cells have gained increasing interest. Adult stem cells can be obtained

from most human tissues. However mesenchymal stem cells (MSCs), obtained from bone marrow, and adipocyte stem cells, obtained from adipose tissue are the most investigated due to their multipotency (ability to differentiate into multiple cell types), and due to ease of harvest without causing significant harm. Moreover, human adipocyte stem cells (hASCs) are of particular interest because they can be obtained from routine liposuction, an elective procedure routinely undertaken for cosmetic purposes, and have shown potency similar to MSCs [6].

Stem cell differentiation protocols overwhelmingly utilize chemical signals (**Table 2.5**), typically provided by growth factors, to induce differentiation. In addition, evidence demonstrates that inhibition of several key Wnt pathways lead to the differentiation of stem cells [103, 104]. These pathways, which include the entire Wnt family are often targeted for differentiation of stem cells towards numerous lineages, and recent work has supported that Wnt pathways are involved in differentiation towards a neural lineage [8].

Table 2.5: Human adipocyte differentiation protocols.

Differentiation Factors	Duration	Eff,	Evaluation Criteria	Ref.
Isobutylmethylxanthine, indomethacin, and insulin	14 days	20%-25%	NSE, NeuN	[105]
Neural basal medium, b-FGF, VEGF, B-27, NGF-β	37 days	89.1±8.67 [3]	TUJ1 [1]	[8]
bFGF, forskolin	14 days	-	-	[104]
Neurogenic Diff. Medium. & Electrical Stimulation	10 days	-	Gene Expression: Ngn2, NeuroD1, NSE, and TAU	[106]
Fibroblast and epidermal GFs neurobasal medium followed by NGF-β & BDNF or forskolin and heregulin β-1	28 days	-	Nestin, SOX-2, aquaporins	[107]
B-27, N1, fibroblast, and epidermal GFs followed by NGF-β &BDNF or forskolin and heregulin β-1	28 days	-	TUJ1 [2]	[107]
Poly-D Lysin/laminin B-27, FBS, L-Glutamine, none essential amino acid, SB-431542, IGF-1	2 days	83±2.49 [3]	TUJ1, PAX6	[108]
Hanging drops	2 days	91.8±0.73 [3]	TUJ1, PAX6	[108]

Basic fibroblast growth factor (b-FGF), vascular endothelial growth factor (VEGF), neuronal growth factor β (NGF-β), growth factor (GF), brain derived neurotrophic factor (BDNF), fetal bovine serum (FBS), Neuron-specific enolace (NSE), and insulin-like growth factor (IGF-1). 1. other criteria were used for oligodendrocytes. 2. Many used, main focus of paper to show novel detection targets. 3. Flow cytometry for β-III-tubulin/TUJ1 positive cells

Based upon evidence that both chemical and electrical signals likely control cell patterning and differentiation during embryonic development, some have investigated electrically mediated cell differentiation. Electric stimulation has been shown to improve the differentiation of already fated cells: neural stem cells [109], osteoblasts [4], and cardiomyocytes [110]. In addition, electrical stimulation of embryoid bodies, formed of embryonic stem cells, has been shown to cause significant expression of TUJ1/β-III-tubulin, indicating differentiation of the embryoid bodies towards a neural cell line, although stem cells not inducted to form embryoid bodies did not show differentiation [111]. Further, human adipocyte stem cells were shown to differentiate toward a neural lineage in the presence of copper and electrical stimulation. In the case of electrical stimulation alone, hASCs showed slight expression of β-III-tubulin 14 days post stimulation. However, stimulation alone failed to cause cells to express MAP2, an indicator of differentiation into mature neurons [112].

As shown in **Table 2.5**, TUJ1, which stains for neuron specific β-III-tubulin is widely used to assess neuronal differentiation of hASCs. For this reason, I chose to assess the differentiation towards a neural lineage of both human neuroblasts and hASCs using TUJ1.

I found that electrical stimulation alone slightly promotes hASC differentiation, similar to previous work. However, I also found that stresses imparted during bioprinting hASCs strongly promote the expression of β-III-tubulin after 6 days without induction medium. Therefore, I observed differentiation much sooner than expected, based upon the length of chemically mediated protocols. In addition, I did not use a neuron specific culture medium containing additives such as B-27 at any time during the experiment. This indicates that both electrical and mechanical signals may cause differentiation of hASCs, which has been poorly explored compared to chemically mediated differentiation.

CHAPTER III

BIOPRINTED CHITOSAN-GELATIN THERMOSENSITIVE HYDROGELS USING AN INEXPENSIVE 3D PRINTER

3.1 INTRODUCTION

Incorporating cells into the printing process requires a non-toxic, biocompatible ink that transitions from a liquid to a solid and maintains cells close to physiological norms. Hydrogels have been attractive candidates because of their high water content and excellent permeability for transport of nutrients [113-115]. There have been many attempts to print using hydrogels from natural polymers such as gelatin and alginates [116]. Many studies are very short term (within couple of hours of printing) [117]. Many groups use higher concentration (6 to 10% wt/v) of gelatin as the ink to print cells which then can form capillaries [18]. Due to their weak stability post-printing, hydrogels are prepared after chemically modifications along with post-processing techniques to improve stability [118-121] I propose using a chitosan-gelatin (CG) biocompatible ink that allows processing in a physiological environment and does not need post-processing. CG solutions with β-glycerophosphate (2GP) spontaneously form hydrogels at body temperature [77]; the solution (pH=7.4) remains in the liquid phase at room temperature and irreversibly forms a hydrogel at body temperature. Chitosan shares many features with glycosaminoglycans present in the extracellular matrix. Since chitosan alone does not support cell adhesion, I blend it with gelatin to support cell adhesion [122]. The gelatin component promotes cell adhesion in the absence of serum proteins.

CG hydrogels are conducive for adhesion of various cell types [78, 79], degrade [123], and phase transition into a hydrogel at 37°C without needing post-processing [124]. CG blends support matrix synthesis [78], and are non-immunogenic in a mouse-transdermal model [124]. CG blends' mechanical properties can be tailored by altering gelatin concentration and selectively cross-linking gelatin post-gelation using transglutaminase (TG) [80, 81], instead of toxic glutaraldehyde.

In this study, I evaluated CG hydrogels as ink using microextrusion bioprinting technology. My custom-built bioprinter is compact, contains a hot plate for gelation of thermosensitive gels, and allows sterile processing inside a biosafety cabinet. Printing at higher resolutions (smaller fiber sizes) while maintaining cell viability and decreasing the time required to finish a print are major hurdles microextrusion printers face [125]. Hence, I evaluated various printing parameters such as speed rate, volumetric flow rate, needle height, temperature distribution and solution composition and preparation. These results show the possibility of printing cell-laden structures using CG with high viability even after five days and the suitability of my inexpensive bioprinter for initial evaluation of novel bioprinter inks.

3.2 MATERIALS AND METHODS

3.2.1 Materials

Low molecular weight chitosan (50 kDa and 75-85% deacetylation), and gelatin (300 bloom, Type A, from porcine skin), were purchased from Sigma Aldrich Chemical (St. Louis, MO). β-glycerophosphate (2GP) was purchased from Santa Cruz Biotechnology, Dallas TX. Vybrant CFDA SE Cell Tracer Kit and Live/Dead Cell Vitality Assay Kit (C_{12} Resazurin/SYTOX) were purchased from ThermoFisher Scientific (Waltham, MA). IMR-32 Neuroblasts, Eagle's minimum essential medium (EMEM), and 0.05% Trypsin-EDTA were purchased from The American Type Culture Collection (ATCC – Manassas, VA).

3.2.2 Bioprinter

Maker's Tool Works (MTW, Oklahoma City, OK) kindly donated a motion platform kit which was assembled in the laboratory. Stepper motors control movement of the bed in the x axis and the print head in the y and z axes (**Figure 3.1a**). According to the manufacturer, the minimum movement resolution (x and y axes) is 12.5µm, the z axis has significantly greater movement resolution. A fourth stepper motor (Kysan NEMA 17) depresses the syringe plunger, at a controlled rate, using a 5mm linear screw with a minimum step angle of 1.8° and holding torque of 4.7in-lb. Combined, the printer can deposit as little as 0.0043µL of material in a single step. Sterile, 1mL disposable syringes with 34g needles (1/4" long) were used with the print head to maintain sterility. However, the prototype extruder originally provided by MTW had significant problems holding syringes in the appropriate orientation during printing. Hence, the extruder was redesigned to maintain the syringe perpendicular to the plate. (**Figure 3.1c**), printable .STL files of the extruder are available in the online version of the article as supplementary material). Further, to provide a level printing substrate, a 1.0% (w/v) agarose solution was prepared and autoclaved for sterilization. The solution was cooled for 10min and 10mL of agarose was aliquoted into 10-cm petri dishes in a sterile hood. The dishes were stored at 4°C until use. Before printing, petri dishes were exposed to UV light to eliminate surface contamination.

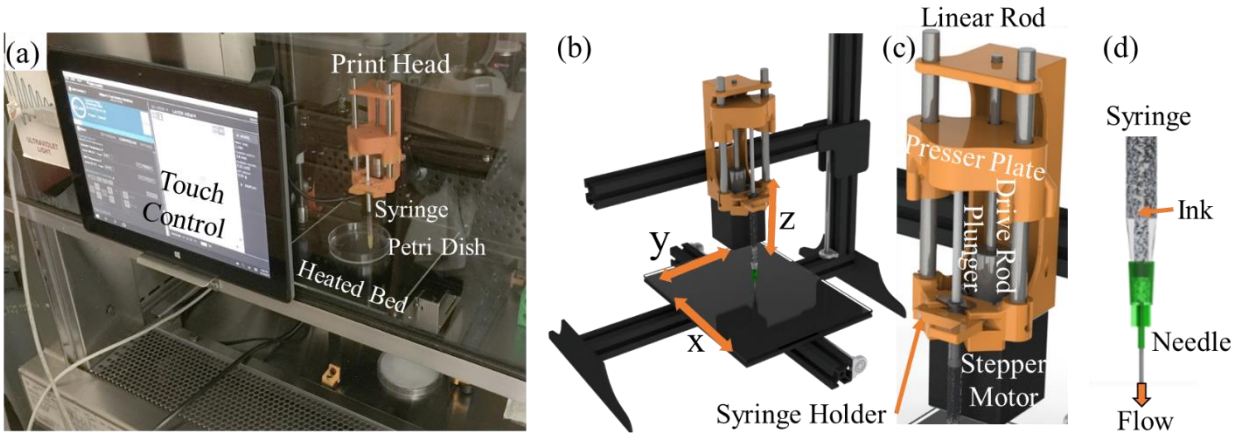

Figure 3.1. Bioprinting parts description: a) Complete cell printing setup for printing of cell laden ink. b) CAD assembly of bioprinter. c) Custom print head and d) close up of syringe.

3.2.3 Software

Open source Slic3r software used in conjunction with the printer did not generate models of the size and type desired. Hence, custom Python code was written to start flow and create a multi-layered square grid (modified from code available at http://www.thingiverse.com/thing:747). The layer height, z offset, skirt radius, number of skirts, fiber spacing, number of fibers, number of layers, flow rate, feed rate (both during printing and during movement), and the bed temperature are parameters input by the user. Unless stated otherwise, general printing conditions used were as follows: 13 layers were printed 70μm above one another, 4 skirts (initial 50mm diameter) to all steady state ink flow, each layer with 20 fibers spaced 1mm apart and successive layers printed orthogonally to the layer below. The feed rate was 100cm/min during printing and 360cm/min when not printing, the bed temperature was set to 37°C, and the code moved the print head vertically at the beginning and at the end of the print to avoid collision with the petri dish sidewall.

The code maintained a consistent flow rate from the extruder (Q) by controlling the distance the nozzle moved (L, cm), the feed rate (V, cm/min), and the distance the plunger moved (E, cm). The program continually computed the distance the syringe should be depressed via $E = LQ/VA_s$, where A_s is the cross-sectional area of the inner syringe barrel. G-code created by the Python script was imported into MatterControl, an open source software available from MTW's website, which controlled the printer.

3.2.4 Preparing and Printing Chitosan-Gelatin Solutions

Chitosan-gelatin mixtures (from 2 wt% to 4 wt% of each component) in deionized water were heated to 120°C for 30 min in a closed container. Then, 0.4 mL of hydrochloric acid (37%) was added per gram of chitosan under sterile conditions. Since bioinks require uniform solution, a sequence of steps were evaluated to obtain uniformity (**Figure 3.2a).** First, 1.9 mL was transferred to a microcentrifuge tube and centrifuged at 14,000×g for 90s. The pH was adjusted to 7.4 by adding 2GP (0.56% w/v) with a custom sprinkler needle (**Figure 3.2b**) to evenly distribute 2GP.

After mixing, the solution was centrifuged at 3,000×g for 60s (similar to conditions reported for epoxy degassing [126]), in some cases cells were encapsulated, the solution loaded into a 1mL syringe without introducing air, a 34g needle attached, and the solution cooled for 5 min prior to printing.

Alternately, after the addition of 2GP, vacuum degassing was attempted by placing the open 2mL centrifuge tube in a holder and placing the holder in a vacuum desiccator without desiccant. The port on the desiccator was connected to vacuum and the atmosphere drawn down.

The printer was placed in a biological safety cabinet, cleaned with isopropanol while unpowered and exposed to UV light. Then the syringe assembly was loaded into the printer with the needle shield in place to prevent contact between the needle and printer housing. The presser plate was lowered until solution was expelled, the petri dish was moved into place and the Z-datum was calibrated to place the needle at the print surface using a small, sterilized Teflon disk with known thickness (0.85mm) placed on the print surface: The needle was lowered until contact was made and the Z-datum set 0.85mm below the reported location by altering the z offset parameter in the

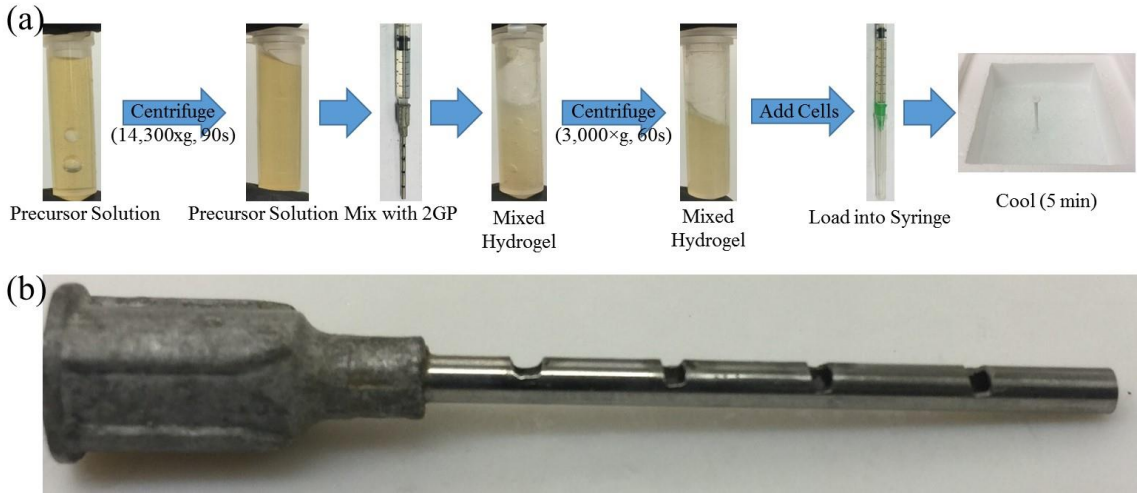

Figure 3.2. Solution Preparation. (a) Flow scheme various steps involved in preparing CG bio-inks for consistent printing. (b) Photograph of a custom needle used to increase homogeneity of mixing to distribute 2GP through the hydrogel during mixing. The needle was created by grinding slots into a 16g hypodermic needle.

python code. Finally, the Teflon disk was removed with sterile forceps and the code was executed via the computer interface.

3.2.5 Analysis of Preparation of Printability

The effect of each preparation step described on printability (which I define as a combination of the duration which a hydrogel can be printed without clogging and fiber continuity) in **Figure 3.2a** was determined by systematic selection of conditions for printing using solutions from each point in the process. Moreover, printability of the resultant hydrogels was quantitatively measured by the time during which the material printed (up to completion of one print) and the time at which pressure expelled the needle from the syringe. Three hydrogels were prepared and printed for each condition.

3.2.6 Rheological Analysis of the CG Hydrogel

Rheology was used to determine the gelation temperature of the hydrogel. Experiments were conducted on prepared hydrogels using a Discover DHR-3 rheometer (TA Instruments, New Castle, DE). A gap of 150μm was used with a 60mm parallel plate. Gelation was measured by temperature ramp, increasing the temperature from 4°C to 45°C at a rate of 1°C/min while taking oscillatory data at 10rad/s with 2% strain. Data collection continued for 130s after the final temperature was reached.

3.2.7 Heated Bed Temperature Distribution

To understand the temperature and its distribution on the print surface and ensure it reached the gelation temperature, a grid template was created, used for measurement by placing beneath i) the agarose substrate used during printing, or ii) 20 mL of water in a petri dish. The temperature at each grid point was measured with a Type K thermocouple connected to a digital display and an average was calculated for the grid. Temperature distribution of the water or agarose was evaluated using an IR camera (FLIR ONE). Thermographic images were captured at each temperature.

3.2.8 Morphological Analysis with Light and Scanning Electron Microscopy

Micrographs of printed structures were obtained using i) light microscopy (AMG EVOS AME-i2111, Life Technologies, Grand Island, NY) under hydrated conditions and ii) by scanning electron microscopy (SEM—JEOL 6360, JEOL USA Inc., Peabody, MA) under dry conditions. Samples observed by SEM were frozen by immersion in liquid nitrogen followed by lyophilization overnight sputter coated with gold for 60s. The SEM specimen stage was tilted at either a 0° or a 45° angle to obtain depth information for the formed fibers.

3.2.9 Evaluation of Feed Rate and Needle Height on Fiber Size

In order to evaluate the effect of feed rate on fiber size, a two-layer grid of fibers was printed with varying feed rates. Fibers were printed sequentially with feed rates of 10, 100, 240, and 480 cm/min on both the first and second layer with 3 cm long fibers, inter-fiber spacing of 1cm, and 70μm layer height through a 60 μm needle.

Similarly, a single layer of 3cm long fibers were printed with the needle 70, 140, 280, and 400 μm above the print surface to evaluate the effect of needle height on fiber size.

After printing, fibers were observed under a light microscope (AMG EVOS AME-i2111, Life Technologies, Grand Island, NY) and digital micrographs were captured at random locations using Micron software. Fiber sizes were measured using ImageJ (National Institutes of Health). A minimum of 30 measurements were performed per fiber. The average fiber size and standard deviation were calculated (values are reported as average ± standard deviation). In some cases, the morphology of dried fibers was also observed by SEM.

3.2.10 Culturing IMR-32 Neuroblasts

IMR-32 neuroblasts (CCL-127) were cultured in EMEM, according to the vendor's protocol. Medium was changed three days a week and cells were incubated in a humidified chamber at 37°C, 5% CO_2, 95% air. When confluent, cells were suspended using 0.5% trypsin-EDTA, pelleted by

centrifugation at 125×g for 5 minutes, and re-suspended in fresh medium. Viable cells were counted using a hemocytometer and trypan blue.

For printing cell-laden fibers, 2×10^6 cells were pelleted, vortexed, and transferred via pipette into 1 mL prepared CG solution. A pipette tip was used to distribute the cells throughout the solution. Care was taken not to introduce air bubbles during mixing.

3.2.11 Cellular Distribution and Viability Analysis

The distribution of cells in printed fibers was analyzed by pre-staining cells with carboxy-fluorescein diacetate, succinimidyl ester (CFDA), similar to our previous publication [57]. In brief, 2×10^6 cells were centrifuged (125xg, 5min), suspended in 5mL of 4µM CFDA in PBS, incubated at 37°C for 20 minutes, washed in 5mL of PBS and suspended in medium prior to disbursing in the CG solution. Florescent images were captured using Nikon Eclipse TE2000-U inverted microscope with attached CCD camera and Prior Scientific Lumen 200 florescence illumination system.

Separately, 2×10^6 cells were mixed into 1 mL of hydrogel and printed into cold (4°C) medium to determine viability. As a comparison, cells at the same concentration (2×10^6 cells/mL) were printed in cell culture medium. All cells were incubated for 5 days with medium changes at day 2 and day 4 and then suspended. The culture medium was retained to keep track of unattached cells. Cells were analyzed using the LIVE/DEAD assay kit according to the manufacturer's protocol, with minor modifications: Cells were spun down (125×g for 5 minutes) and the pellet was washed with sterile phosphate buffered saline (PBS). The cells were then suspended in 100µL of PBS containing 0.1% bovine serum albumin, 500nM C_{12}-resazurin dye, and 20nM SYTOX green dye. The cells were incubated for 15 minutes, transferred to ice, and analyzed immediately, via flow cytometry (FACSFlow, BD Biosciences). Obtained data for each sample were plotted as dot plots where the cell populations separate into three groups; Dead cells emit high-level green fluorescence and healthy, metabolically active cells emit high-level red fluorescence. However, injured cells exhibit

reduced red and green fluorescence. Based on this information, percentages of live, injured, and dead cells were obtained using a standard quadrant analysis. The same quadrants were used in all conditions.

3.3 RESULTS

3.3.1 Print Head Deflection

When printing solutions, many use pneumatic systems which require compressed air to be supplied to the print head. In order to minimize these requirements where additional pneumatic lines have to be constructed inside a biosafety cabinet, I used a printer that was applying a simple compressive force through a plate. Code was written where the presser movement is linearly related to the dispensed volume. However, for linear transfer of force from the presser to the solution, other resistances have to be minimized. In this regard, first I evaluated the initial presser plate that was provided by the vendor. When compressive force was applied, both the syringe plunger and presser plate experienced unwanted deflection (**Figure 3.3a**). The original presser plate (**Figure 3.3b)** had an open back that was intended to clip around linear bearings and lacked support for the syringe barrel. The force exerted on the plate by the plunger was sufficient to unclip the presser plate during printing. Even when secured with a zip tie, the presser plate rotated sufficiently to impart deflection to the plunger. Therefore, the print head was redesigned (**Figure 3.3c**) to completely encompass the linear bearings: the bearings are inserted from the bottom and held in place by a plate with three screws. In addition, the initial syringe retaining mechanism was too weak to hold the syringe when printing and was replaced with a binder clip which allowed for deflection. The second design incorporated a v-shaped channel with a spring loaded bar that retains the syringe orthogonal to the presser plate. Combined with the improved presser plate, the redesigned deposition tool held the syringe in a single plane and eliminated bow in the

syringe plunger (**Figure 3.3d**). The redesign eliminated the source of deflection that did not contribute to flow of the solution. Hence, it minimized the error related to the assumption that fluid flow is linearly proportional to the movement of presser plate.

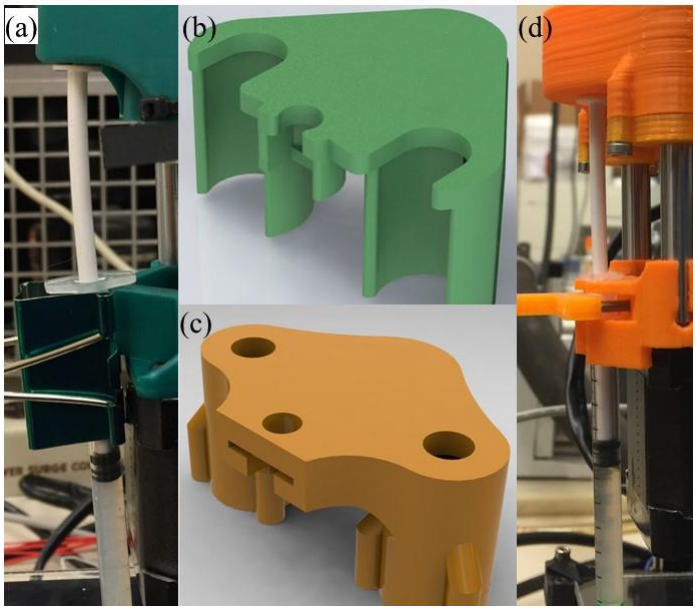

Figure 3.3. Comparison of the presser design on the syringe deflection. (a) Syringe loaded into the initial extruder design and clearly showing deflection of the plunger. (b) Original presser plate showing the design which allowed the plate to deflect. Redesigned presser plate (c) that, combined with the redesign of the mechanism that holds the syringe in place prevents deflection in the syringe (d).

3.3.2 Effect of Solution Preparation on Printability

Solution homogeneity is required to create continuous, uninterrupted fibers. Initially, hydrogel was mixed based on hand printing trials and loaded into a syringe. During printing, needles clogged after short dispensing times and fibers exhibited gaps created by air bubbles. I hypothesized that contaminant solids in the polymer stock solutions blocked the needle due to size mismatch or aggregation, and that prematurely gelled the solution, blocking the needle due to its proximity to the heated print surface. In support of my hypothesis, I observed undissolved particulates present in the precursor solution under a stereoscope (not shown) and improved outcomes at lower ambient

temperatures. I investigated centrifugation of the precursor solution to remove particles and cooling of the solution prior to printing to prevent premature gelation. Further, I investigated two degassing methods: vacuum degassing and centrifugation.

To evaluate the separate and combined effect of these methods I set up a series of experiments, shown in **Table 3.1**. I examined the general architecture of the structure printed for each condition (**Figure 3.4a**). I found that combining all of the processes created the structure with the fewest defects that was completed without loss of the needle to overpressure which I quantified by measuring both the time until flow stopped and the time until the needle was lost to overpressure (**Figure 3.4b**).

Centrifugation of the solution resulted in visible particulates at the base of the solution and improved print time in a few cases to an average of 98s, still insufficient to begin printing the scaffold itself. Cooling the solution prior to printing demonstrated a significant, positive effect on printability, increasing print time to an average of 238s, indicating premature gelation was a major factor in clogging.

Vacuum degassing using a vacuum desiccator had no visible effect on the solution and was abandoned. In contrast, centrifugation at 3,000×g for 60s succeeded in removing entrapped air bubbles, leaving a semitransparent solution.

Progressive improvement in fiber continuity and number of fibers that could be printed was observed when multiple processing steps were incorporated. The print time reached a maximum time of 325s as determined by a completed print. At least two of the three prints completed without interruption for conditions 6 and 8, indicating that cooling and particle removal prevented clogging. Degassing did not affect clogging. However, it improved the overall architecture as demonstrated by the scaffolds for conditions 6 and 8. Condition 8, a two stage centrifugation protocol with cooling resulted in an airless solution that printed consistently and was used throughout the work

conducted. Three prints were conducted for each condition

Table 3.1: **Effect of preparation steps on printability**.

COND.	PARTICLE CENTRIFUGATION	CENTRIFUGAL DEGASSING	GEL COOLING	REMARKS
1				No printing
2	X			No printing
3		X		No printing
4	X	X		Improved printing, inconsistent
5			X	Unreliable printing for short time periods
6	X		X	Improved printing, inconsistent
7		X	X	Improved printing, inconsistent
8	X	X	X	Improved, consistent printing

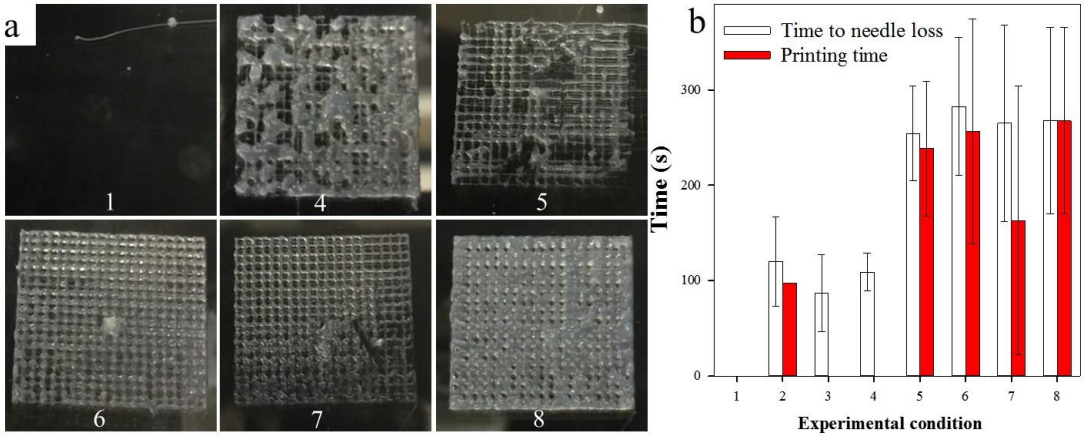

Figure 3.4: **Effect of solution preparation on printed fiber quality.** a) Photographs of printed scaffolds that show the importance of various preparation steps for printing. b) Printability based on print time based upon various preparation steps (n=3). Numbers correspond to preparations detailed in Table 3.1. Images from processes 2 and 3 did not result in significant printing and were omitted. Each printed scaffold is 2cm × 2cm.

3.3.3 Rheological Determination of Gelation Temperature

For successful printing of thermosensitive hydrogels, the phase transition must be accomplished without affecting cell viability. Hence, understanding the gelation characteristics is important to ensure solutions gel at a survivable temperature. In particular, addition of gelatin could affect the gelation characteristics. Hence, first I assessed the gelation by performing analysis in a larger sample of solution. When cold 3%-3% CG solution (3% w/v chitosan, 3% w/v gelatin) was warmed

to 37 °C (**Figure 3.5**), gelation was observed. The formed hydrogel can be manipulated, by hand, as a single piece and the hydrogel was pliable, similar to our previous publication [124].

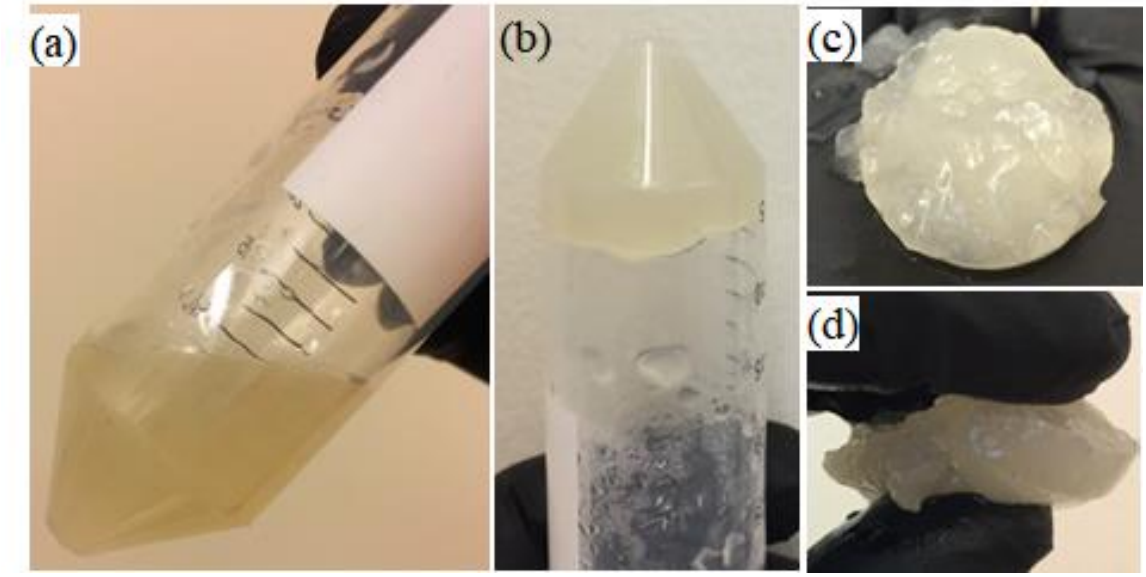

Figure 3.5: Photographs of 3% 3% CG solution and hydrogels. (a) Solution at 4°C. (b) gelation at physiological condition. (c) Formed hydrogel can be lifted by hand. (d) Appearance of the hydrogel along the thickness when held by fingers.

Next, the effect of chitosan concentration on gelation characteristics was evaluated. Increased chitosan and gelatin concentration proportionally increased the viscous modulus (**Figure 3.6a-c**), particularly at lower temperatures. When the temperature was increased, elastic modulus increased significantly suggesting occurrence of gelation. Similarly, viscous modulus also increased when the temperature raised above the gelation temperature, which ranges from 26°C to 32°C based on hydrogel composition. Increasing chitosan concentration decreased gelation temperature and increased the rate of gelation (**Figure 3.6d-e**), similar to published reports [127]. At 37 °C, rate of gelation was near 120s for 2%-2% CG while increasing the concentration to 3%-3% CG formulation gelation rate decreased to less than 60 s. Increase in rate of gelation with chitosan concentration is useful for bioprinting, as these factors together could decrease the fiber size. However, modification to the solution resulting in a gelation temperature at or near room temperature is likely

to increase the occurrence of premature gelation; this indicates the need for care when increasing the chitosan concentration.

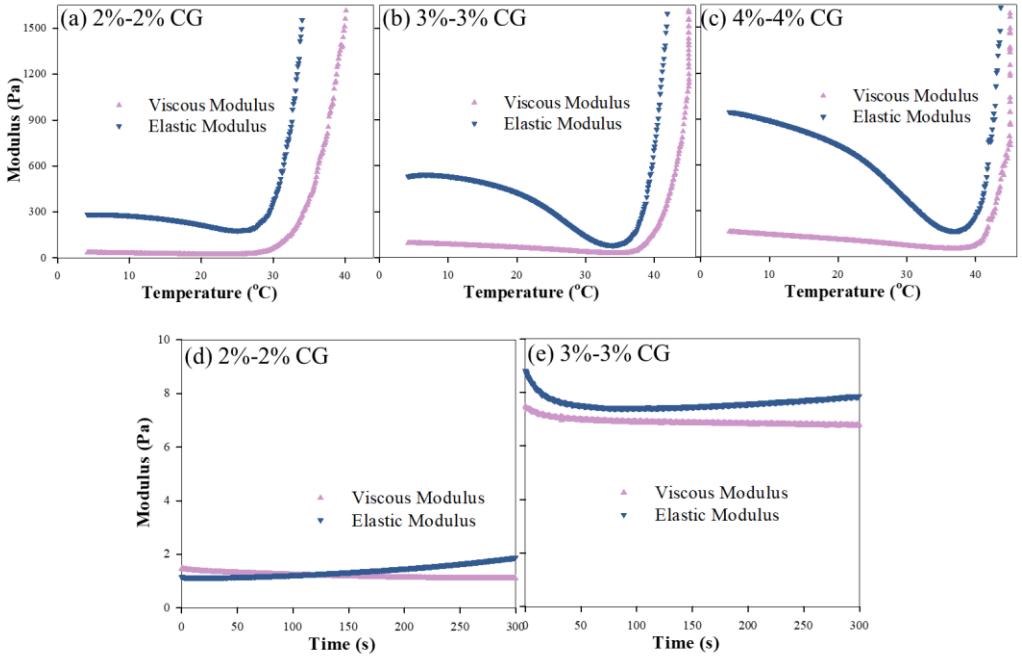

Figure 3.6: Effect of polymer concentration on gelation characteristics. (a-c) Experiment were performed using a temperature ramp run at 1°C/min from 4°C to 47°C with an initial 60s soak time and a final 130s soak time. Data demonstrates onset of gelation. (d-e) Experiment were performed using a constant temperature of 37°C to determine gelation time.

3.3.4 Bed Temperature and its Distribution

The bed temperature needs to be carefully maintained at the gelation temperature determined for each solution to allow for proper solution gelation. Using agarose as the print surface increased heat loss between the heating element and print surface. The temperature of the agarose print surface was approximately 30°C lower than the temperature set for the heated bed. **Figure 3.7a** shows that the temperature of 20mL of water was similar to that of 10mL of agarose in a 10cm petri dish. The temperature distribution (**Figure 3.7b**) demonstrates the temperature of agarose is more uniform across the surface than that of water. The average temperature of 20mL of deionized water (2.5mm thick) in a 10cm petri dish was 35.4°C, the average temperature of 10mL of agarose

(1.2mm thick) was 36.0°C. Irregularities in the temperature profile could attribute to variation in gelation rates and the fiber size distribution when thermosensitive hydrogels are used.

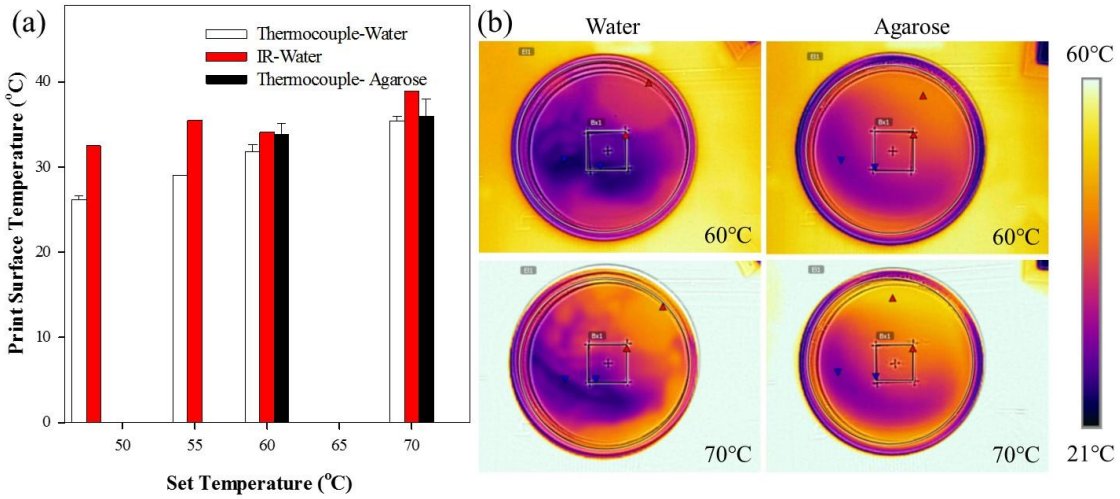

Figure 3.7: Bed temperature characterization. a) relationship between heat source temperature (measured by printer) and print surface temperature (measured by type k thermocouple). b) Thermal images of 10mL agarose print surface or 20mL water showing the distribution of temperature.

3.3.5 Effect of Feed Rate, Flow Rate, and Bed Temperature on Fiber Diameter

Understanding the alterations in fiber diameters while maintaining viability is a crucial goal for 3D bioprinters. I hypothesized that adhesion between the fiber and print surface combined with cohesion of the hydrogel may cause thinning as feed rate, the speed with which the needle moves parallel to the print surface, increases. To examine this hypothesis, fibers were printed at different feed rates. The maximum rate (480cm/min) was the manufacturer's recommendation for polymer printing. As the feed rate increased, fiber width decreased when fibers were printed on a surface maintained at 25°C (**Figure 3.8a**) or 37°C (**Figure 3.8b**). At the slowest feed rate (10cm/min), the movement of the print-head was too slow, causing solution to gel in blobs, as observed by large deviations indicating these fibers had significant variation in width compared to fibers tested at higher velocities. Blobbing disappeared as movement speed increased. At 480cm/min, the print head was moving fast enough to cause the fiber to lose cohesion and skip in places. In addition, I

observed that increasing the actual bed temperature from 25°C (**Figure 3.8a**) to 37°C (**Figure 3.8b**) decreased the variability of printed fibers at all feed rates and decreased the fiber diameter when printed at 100, and 240cm/min. However, varying the flow rate at 25°C did not cause any difference in fiber size. Temperature has a much greater effect on the fiber size than flow rate, indicating that the fiber sizes observed are determined by gelation.

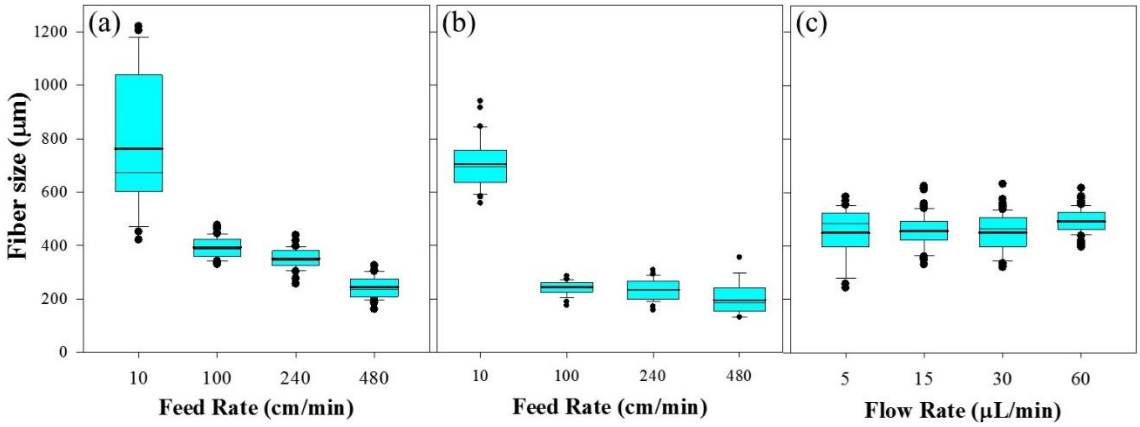

Figure 3.8: **Box plots showing the effect of printing parameters on fiber size distribution.** (a) feed rate on fiber size of 3%-3% CG hydrogels printed at a rate of 30µL/min with the agarose print surface at 25°C a), b) feed rate on fiber size of 3%-3% CG hydrogels printed at a rate of 30µL/min with the agarose print surface at 37°C. c) Effect of flow rate on fiber size at a feed rate of 100 cm/min. box represents the 25th and 75th percentiles, the thick line is the mean of the values, and the thin line is the median. n≥30 in each condition.

3.3.6 Effect of Needle gap

The distance between the needle and print surface strongly affects the completeness of the resulting print. Since petri dishes lack the flatness tolerance required for bioprinting, distance between the needle and print surface could vary significantly from location to location. In order to minimize this variability, agarose gels were formed in the petri dishes on a level surface. The agarose created a level surface and prevented damage to the needle upon contact with the print surface.

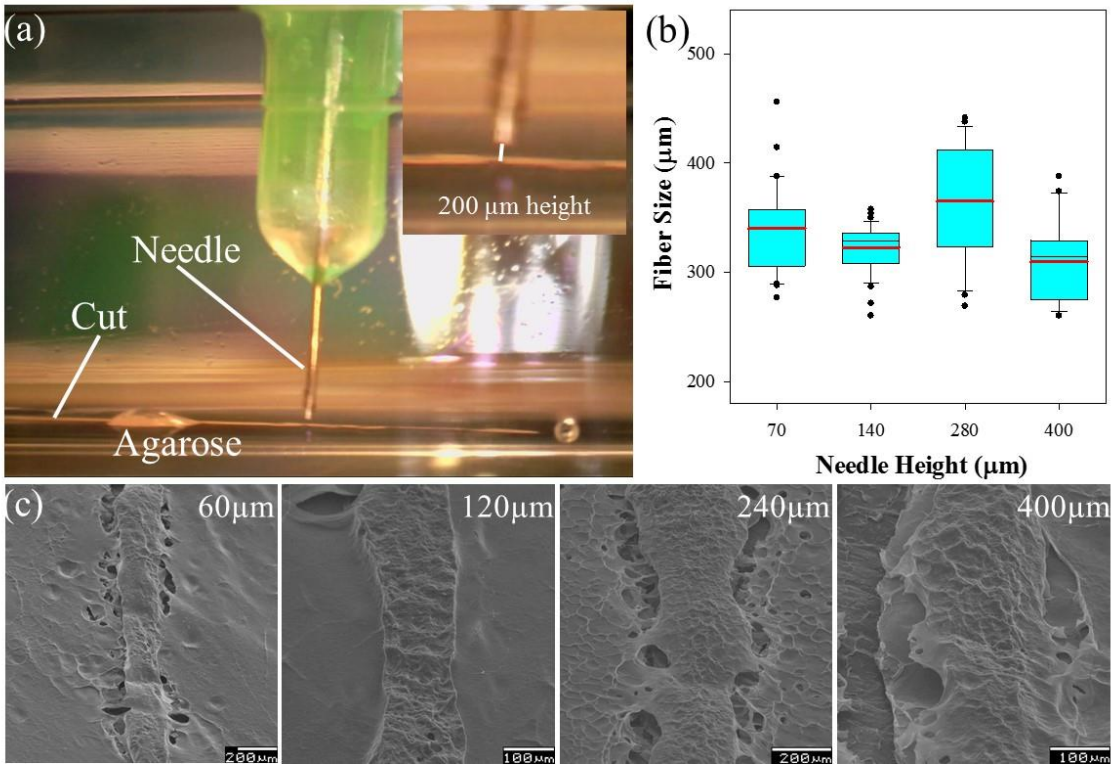

Figure 3.9: Effect of needle gap on fiber quality and size. a) photograph showing the needle (34g) position where it initially touches but does not enter the surface of the agarose. 1% DMEM powder with phenol red was added to the agarose for contrast. b) Box plots showing the effect of needle height on fiber size distribution. Box represents the 25th and 75th percentiles, the thick line is the mean of the values, and the thin line is the median. n≥30 in each condition. c) Scanning electron micrographs of fibers printed at different heights.

Setting the needle to touch the agarose on the first layer (**Figure 3.9a**) allowed printing of continuous fibers. However, setting the needle below the surface of the agarose causes injection of the solution into the agarose and may cause premature gelation within the needle. Setting the gap above the surface prevents adhesion between the hydrogel and agarose surface. Without adhesion, large droplets form before their weight overcomes adhesion to the needle and cohesion to the main body of hydrogel. No fibers form in this case. For traditional 3D printers, the height of the 'needle' above the print surface is normally fixed only infrequently. However, using slip tip disposable syringes with single use needles and agarose as a print surface, the gap between the needle and the surface varies with each newly loaded syringe. Therefore, the Z datum should be adjusted between

each print. This could be carried out either by changing the initial layer height in the software or by using a physical setscrew on the printer. I chose to use a small, sterilized teflon disk with known thickness placed on the agarose surface. I lowered the needle until contact was made with the Teflon disk to determine the height from the surface of the agarose. The printer was set to begin printing at the absolute height of the disk minus its thickness using a parameter within the custom code.

3.3.7 Sterile Printing in Petri Dishes, Viability.

When printing cell-laden structures, sterility is critical. My printer is small enough to be placed in a conventional 4-ft laminar biosafety cabinet used in routine cell culture. This allowed us the perform the printing process by placing the entire assembly within the biosafety cabinet. All surfaces were disinfected with 70% isopropanol, and irradiated for 20 minutes with the UV lamp present in the biosafety cabinet. A touch screen tablet was used to control the printer and it was mounted on the sash of the biosafety cabinet.

Cells were printed and incubated for five days with continuous monitoring. No bacterial or fungal contamination was observed, suggesting successful sterile printing. Morphology of cells was similar to the unprinted cells (**Figure 3.10a**). After five days, viability was analyzed using two-color flow cytometry. These results showed (**Figure 3.10b**) that neither the flow rates nor feed rates in the investigated range had a significant effect on live, dead, or injured cells. Cell viability with

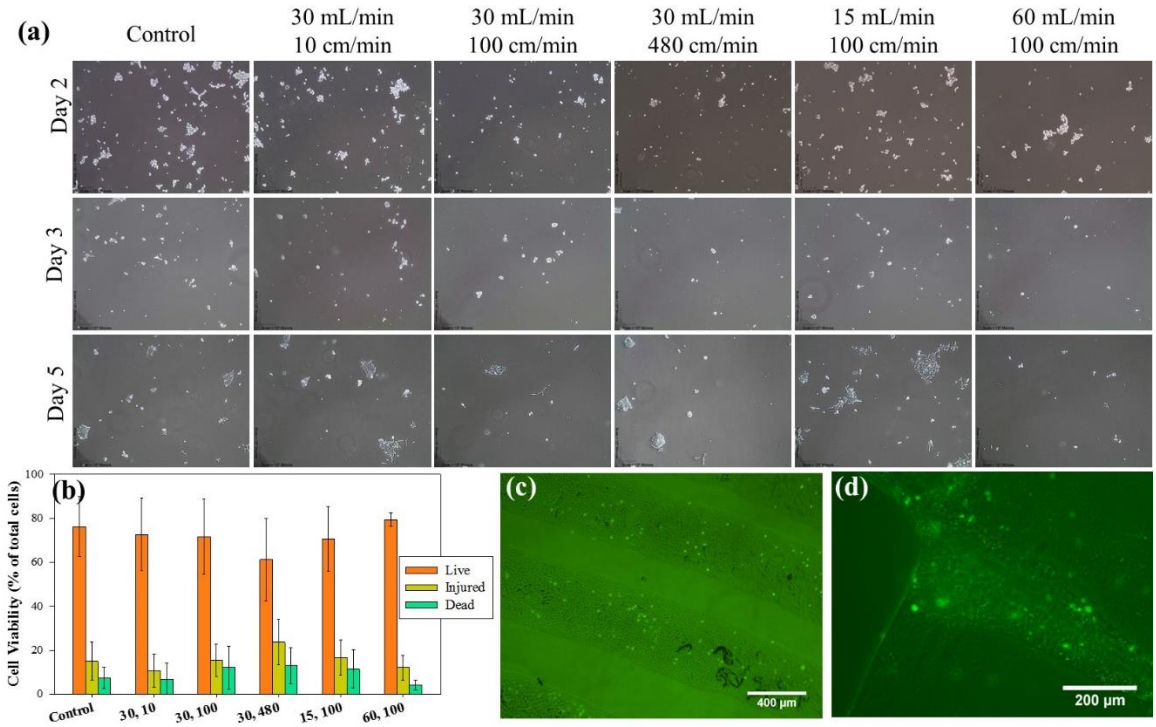

Figure 3.10: Effect of printing parameters on neuroblast morphology and viability. a) micrographs of cells printed in medium through the 34g needle showing changes in cell morphology when printed at different flow rates and feed rates. b) Changes in cell viability when printed at flow and feed rates conditions identical to micrographs shown in panel (a). Data represents average and standard deviations from four independent experiments. c) & d) Fluorescent micrographs showing CFDA-SE stained cells encapsulated in printed Hydrogel fibers. (c) is parallel fibers arranged concentrically one-layer high. d) 12 layers printed on top of one another.

30 mL/min flow rate and 100 cm/min velocity at 140 µm nozzle height was greater than 70%. In order to understand the presence of cells within the hydrogel, pre-stained cells were mixed with CG solutions and printed at 100 cm/min. Observation of those cells revealed successful gelation and presence of cells within the hydrogel (**Figure 3.10c&d)**. In addition, the cells were uniformly distributed throughout the printed fibers. Since staining required 20 min incubation of cells at 37°C, they had to be cooled for 5 min in the refrigeration (4°C) to lower their temperature. Addition of cells directly without cooling resulted in premature gelation which affected printability. This also suggested the need to ensure uniform temperature distribution to prevent localized heating and premature gelation.

3.3.8 Printed 3D Structure Architecture

Next, I evaluated the possibility of printing multiple layers. I successfully printed 13 layers using CG solution. When printed structures were observed under light microscopy in hydrated conditions, a nice grid structure mimicking the printed format was observed (**Figure 3.11a).** This suggested the possibility of printing multiple layers using CG solutions. In order to better understand the features of these printed structures and intersections where fibers crossed over, samples were analyzed by scanning electron microscopy. In order to not alter the morphology of the fibers, entire printed structure along with the agarose layer were analyzed. (**Figure 3.11b)**. Overall, similar patterns were observed along with the smooth agarose layer (**Figure 3.11c).** Variation in heights across cross-over regions was observed, which could be attributed to the sagging when fibers are printed over each other. Adding layers atop previously printed layers before they gel can cause them to sag or increase in width. This could be attributed to the delay in the increase in temperature to that needed for gelation. Increasing the layer height further results in a larger, spread profile and encapsulation of previously printed fibers. Hence, it was difficult to determine all the 13 layers (**Figure 3.11d)** even in the cross-sectional view. In addition, fibers appeared more flattened at some regions relative to other regions. As the rate of gelation decreases, the solution requires more time to transform into a hydrogel. This increases the spreading of the polymer solution thereby increasing fiber size. Further investigation of the polymer concentration and bed temperature used during printing is necessary[128].

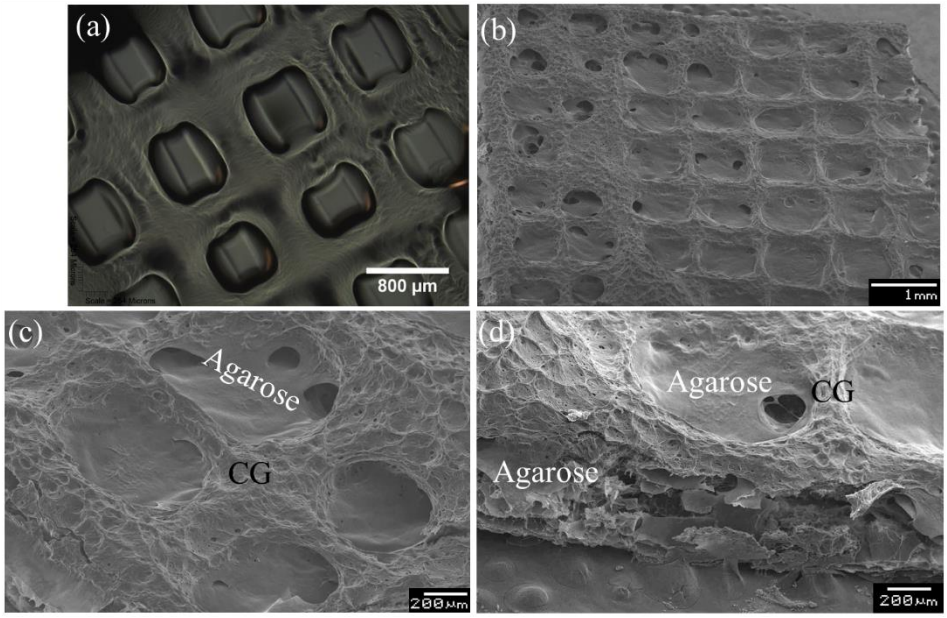

Figure 3.11: Morphology of printed 3D structures. a) Light micrograph of printed CF showing post-printing architecture. SEM micrographs taken at a tilt angle of 45° to show b) scaffold overall pore architecture and c) one junction within the architecture. d) Cross-sectional view of the scaffold showing the agarose and printed CG hydrogel

3.4 DISCUSSION

In this study, I show the possibility of using my inexpensive bioprinter in conjunction with CG hydrogels to print cell-laden structures with high viability. A number of bioprinters are commercially available. My printer cost is less than one-tenth the price of the least expensive commercial printer [129, 130]. The printer kit I obtained required user assembly and modification of the plunger to accommodate syringes. In addition, the use of commercially available, disposable hypodermic syringes and needles eliminates the need for rigorous cleaning and sterilization protocols to reuse expensive metal or glass syringes. The printer is also compact enough to be retrofitted in any sterile hood, easily transferrable when not in use, and is inexpensive at less than $1000 initial investment. Others have examined inexpensive printing systems. A printer from Makers Tool Works has previously been explored to print synthetic polyester, ε-polycaprolactone, with a modification to the extruder to use plastic beads instead of continuous filament [41]. Python code was used to create

custom structure without cells. Another low cost microextrusion bioprinter modified from a commercial printer was described to inject cells into prefabricated hydrogel using pulled glass pipettes [43]. Although this method could allow the precise placement of cells, there was no demonstration of controlling the overall hydrogel architecture and they did not investigate the use of hydrogel as inks. Using custom scripts to create scaffolds allowed us to design specific patterns of interest as well as control the printer in fine detail. However, the ease of converting 3D models to g-code and printing them directly is lost. Ideally, a custom slicer would be written that allows the fine control of scripting and converts 3D models to g-code. My results show that my printer is suited to initial evaluation of novel inks where a more expensive system represents too much risk. Our CG hydrogel has not previously been investigated as a bioprinter ink and did not justify significant investment in technology without evaluation of its suitability as an ink. Our system allowed that evaluation to be conducted without risky investment in more expensive technology.

I demonstrate a bioprinting technology using CG and β-glycerophosphate (2GP), which spontaneously forms hydrogels at 37°C [77] requiring no post-processing to obtain cell-laden structures. Using alginate-based hydrogels and a 210 μm nozzle, mesenchymal stem cells with high viability were printed [63]. Alginate forms hydrogels via crosslinking by calcium ions (Ca^{2+}) that are typically introduced by washing the printed structure with a solution of calcium chloride [60-63, 66]. There is limited understanding on the effects of modifications on cell processes, controlling the fiber size, and the effect of nutrient transport during sustained culture of cells. Many ink formulations use a combination of gelatin and alginate [67, 68], spider silk protein [74], and gelatin methacrylamide [10, 71, 72]. Most require a chemical or irradiative crosslinker. Spider silk protein, one of the few examples that did not require post-processing, demonstrated 70% viability when printed through a 300μm nozzle, while unprinted cell viability, with encapsulation in spider silk protein, was 97%. Our viability results are similar to those. Nevertheless, various formulations of CG can be developed to mimic other matrix elements and mechanical properties.

Printer resolution is critical to mimic the structures found in the human body [52]. Increasing resolution continues to be a goal for microextrusion bioprinters [131]. Material properties and temperature control whether a rounded fiber will slump or remain round. High viscosity has been found to be an important property that a hydrogel needs to possess to prevent slumping [131]. Thus I investigated the changes in rheology with concentration of chitosan and gelatin. Our results demonstrated that in CG hydrogels, thermal gelation mechanism needs a greater degree of control: ambient temperature, solution temperature, and friction within the needle may all contribute to temperature changes and affect gelation. In addition, presence of air bubbles and impurities affect the printability.

Fibers appear to experience some slumping or under-gelation in which the gelation is occurring too slowly to completely separate all fibers from one another, similar to the under-gelation case [128]. In CG hydrogels, in addition to increasing the polymer concentration, eliminating insulating factors to raise the fiber temperature more rapidly may improve the print resolution. This might be done by the addition of pre-warmed media or providing a buoyant force using poloxamers to counteract gravitation force. However, diffusion of the fiber into solution may be an issue. In addition, rheological studies are needed for any new polymer concentrations tested to determine the gelation temperature in order to prevent premature gelation, and the gelation temperature should also be kept above room temperature.

Overall, the need to pre-cool the syringe, heat loss at the print surface, concentration dependent gelation temperature, and temperature dependent gelation rate emphasize the importance of temperature control on fiber characteristics for thermogelling hydrogels. I expect these results will extend to other thermogelling hydrogels investigated as bioprinter inks which are currently underrepresented in bioprinting research.

Aguado et al. reported shear thinning hydrogels improved printed cell viability over that of cells printed in PBS. Their hydrogel had a calculated zero shear viscosity of 0.0846 Pa s whereas, my hydrogel has a calculated zero shear viscosity of 0.869, an order of magnitude greater [65]. Since viscosity is directly related to shear stress $\left(\tau = \eta \frac{dv}{dy}\right)$, the shear stress experienced at the wall of my needle for similar flow conditions is expected to be significantly greater. Therefore, a method of determining the viability of cells within printed hydrogels is of significant interest. I have shown in the past that gelatin can cleave CFDA and cause fluorescence that obscures any stained cells. Therefore, fluorescent microscopy using a LIVE/DEAD kit may not be a viable method of analysis. I attempted to analyze the cells and hydrogel via flow cytometry by printing cells within hydrogel without heating; intending to cause the dissolution of the hydrogel into medium without allowing it to gel. Printing into cold medium did not result in dissolution of the hydrogel, possibly due to gelation of the gelatin within the solution. Printing the structures and washing with room temperature medium is of interest. I need to further investigate the effect of flow rate on fiber size to determine if a lower flow rate will produce smaller fibers. Further, I will examine the functionality of printed cells by testing their alignment in an electrical field and the effect of co-culturing cells with known cell-cell interactions

As temperature control is the most important factor in my system, increasing the slope of the gradient between the stored and printed hydrogel is expected to improve the system. Ideally, the hydrogel within the needle would be maintained at 4°C, with the printed fiber directly below maintained at a consistent 37°C. I envision water circulated through an aluminum block or sterile tubing from an ice bath and isolated from the sterile environment inside the hood to negate heat transfer to the hydrogel in the syringe to move the system closer to the stated ideal. Alternatively, since the hydrogel exhibits a semi-gelled state at 4°C, I see maintaining the hydrogel at that temperature and then quickly raising the temperature to 37°C possibly using pre-warmed medium. However, I expect a loss of hydrogel integrity due to polymer diffusion into the medium. To prevent this, a dense,

pre-warmed biocompatible hydrophobic solution or polymer slurry might be used to quickly raise the temperature of the hydrogel, then washed away with PBS and replaced with medium.

3.5 CONCLUSION

In this study, I adapted a low cost 3D printer to obtain cell laden structures using CG injectable hydrogels. Further, I evaluated a hydrogel developed in our laboratory using the bioprinter. I demonstrated that solution preparation steps (centrifugation, mixing, and degassing) are important in obtaining consistent printability and fiber formation. Using agarose gel as a print surface allowed obtaining uniform print surface to maintain a constant gap with the needle tip. The fiber size decreased from 760µm to 243µm as the feed rate increased from 10cm/min to 100cm/min. Further, I can control the gelation of the hydrogel using heat and gelation process occurs over a short time period. The gel is shear thinning and may protect cells during printing, my printing system does not decrease the viability of cells printed in medium compared to the control, and cells were uniformly distributed throughout the hydrogel. I developed a low cost alternative to available bioprinters that will assist researchers in initial evaluation of novel materials for bioprinting without incurring the significant costs imposed by other systems. Using my inexpensive system, I have shown the novel CG hydrogel ink has significant potential for bioprinting various cell-laden structures.

CHAPTER IV

DESIGN AND VALIDATION OF A COMPACT DEVICE FOR *IN VITRO* ELECTRICAL STIMULATION OF MAMALLIAN CELLS

4.1 Introduction

Movement of cells due to electrical stimulus, known as galvanotaxis has long been investigated as an important factor in the emergence of cell patterns during fetal development [95]. However, galvanotaxis devices are bulky, and have multiple components that are difficult to transport while maintaining sterility [22-24]. Using one such chamber, and application of 100 mV/mm, rat-bone-marrow derived stem cells and adipose derived stem cells (hASCs) showed osteogenic differentiation [132]. Some used 200μA of direct current to convert hASCs into osteogenic cells [133]. Higher voltages applied to hASCs are shown to cause differentiation towards neuronal cells. hASCs exposed to an electrical field of nearly 2000mV/mm showed differentiation towards neuronal cells [25]. Cells respond faster and drastically to electrical stimulus than to chemical stimulus.

Some have converted a 6-well plate into a galvanotaxis device that uses platinum electrodes directly immersed into medium [134], or by using carbon electrodes in a petri dish [133]. However, direct immersion of electrodes in the vicinity of the cells raises concerns about their effect on cells and culture medium. I sought to engineer a compact device that has the same sterility and portability

advantages seen in newer technologies, while recreating the electric field gradient and uniformity observed in traditional devices. With the advances in additive manufacturing, adaptation of 3D printing processes in medical science is gaining significant attention. 3D printing technologies can be leveraged to create low cost, complex devices for laboratory use.

In this work, I designed a compact stimulator using computational simulation to obtain a uniform electrical field and 3D printed devices of interest. These devices were easy to transport and maintain sterility while performing experiments which required microscopic observation. I further tested the compact device using neuroblasts (NBs) and human adipocyte stem cells (hASCs). Since cells could behave differently, I evaluated the effect of culture duration prior to stimulation.

4.2 Materials and Methods

Agarose powder was purchased from Sigma Aldrich Chemical (St. Louis, MO). IMR-32 Neuroblasts, Eagle's minimum essential medium (EMEM), Fetal Bovine Serum, and 0.05% Trypsin-EDTA were purchased from The American Type Culture Collection (ATCC – Manassas, VA). StemPro Human Adipose-Derived Stem Cells, MesenPRO RS Medium, MesenPRO RS Growth Supplement, L-glutamine, Dulbecco's phosphate-buffered saline (DPBS), Alexa Fluor 488 goat-anti-mouse IgG2a antibodies (A-21131), 4',6-Diamidino-2-Phenylindole, Dihydrochloride (DAPI), and Alexa Fluor 546 Phalloidin were purchased from ThermoFisher Scientific (Waltham, MA). TUJ1 clone anti-β-III tubulin mouse primary IgG2a antibodies were purchased from Biolegend (801201; San Diego, CA). Ag/AgCl point electrodes were purchased from In Vivo Metrics (Healdsburg, CA). Ag/AgCl disk electrodes (9mm diameter and 1mm thick) were purchased from ALA Scientific Instruments (Farmingdale, NY). Polylactic acid (PLA) printer filament was obtained from MakerBot (New York City, NY). Silicone adhesive was obtained from Lowes (Stillwater, OK).

4.2.1 Galvanotaxis Device Development

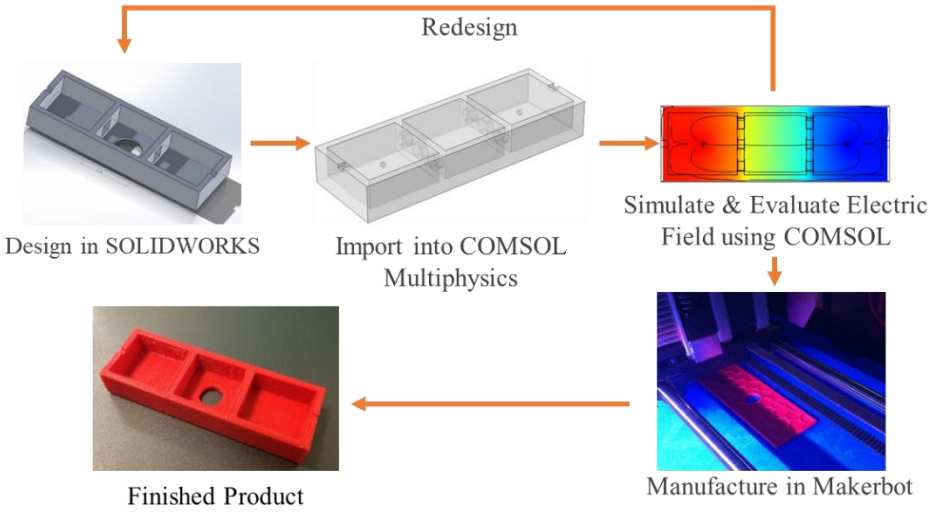

Figure 4.1: Flowchart of the compact device design process

The overall design process for the compact galvanotaxis device is detailed in **Figure 4.1.** First, a model was created in SolidWorks (Dassault Systems SolidWorks Corporation, Waltham, MA). The overall device dimensions were constrained to match the footprint of a standard microscope slide (75mm long×25 mm wide, and, 13mm height) so that the device is compatible with inverted microscopes. The device was divided into three chambers, the outer two chambers house the electrodes and a solidified agarose gel to chemically isolate the electrodes from the central chamber which houses a coverslip seeded with cells (or with adherent, bioprinted hydrogel) and a window for observation via light or fluorescent microscopy (**Figure 4.2a**). The central, cell-culture chamber was 25 mm in length. Two broad designs were considered to separate the cell-culture chamber from the two outer electrode chambers and confine agarose during cooling: i) with physical barriers (**Figure 4.2a**) and ii) without physical barriers (**Figure 4.2b**) to improve conductivity. Three designs were created with physical barriers and point electrodes (spheres with 2mm diameters) situated at the center of the outer chambers with holes in both barriers: i) one 3.81 mm hole (**Figure 4.4a**); ii) one 7.62 mm hole (**Figure 4.4b**); iii) three 5mm holes (**Figure 4.4c**).

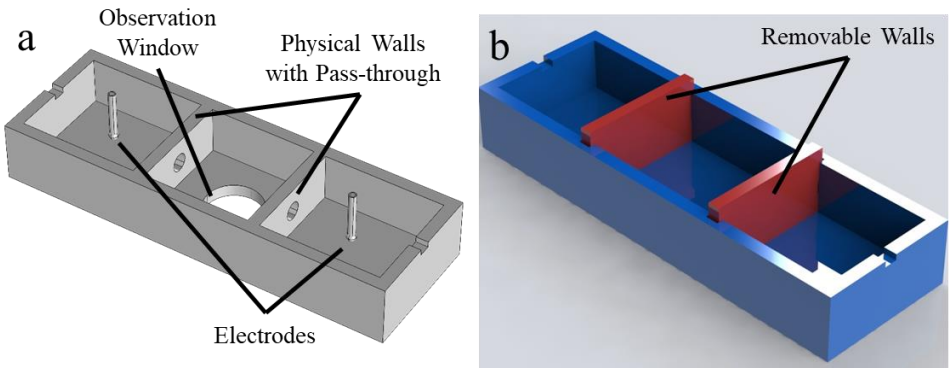

Figure 4.2: Two major compact stimulator designs. a) Model of the electrical stimulator with physical walls. b) Cartoon concept drawing of the open stimulator.

A single open design was considered with three different electrode placements: i) against the stimulator floor (**Figure 4.4d**) and ii) parallel at the same distance as the point electrodes (**Figure 4.4e**), and iii) electrodes located against the outer walls (**Figure 4.4f**). In these designs, disk electrodes, which spread the current over a larger area unlike the point electrodes, were considered to reduce localized heating (**Figure 4.3b**). Commercially available disk electrodes, 9mm-diameter and 1mm-thick, were used. All designs were imported into either COMSOL for simulation to evaluate the expected EF within each device or sent to a 3D printer to manufacture devices.

4.2.2 Computation Simulation of Electrical Field

Models were imported from SolidWorks into COMSOL as .stl files. Import limitations required that these devices be imported without holes in the barriers. After importing the device, holes were drawn within COMSOL. The agarose compartment was considered to have conductivity similar to culture medium. Hence, all chambers were considered to be filled with culture medium. These geometries were imported from SolidWorks to fill all three blocks. For comparison, I modeled a previously reported 3-component galvanotaxis device [23] (**Figure 4.4g**).

The electrical currents module within COMSOL was used to simulate the initial, steady state electric field (EF) in each device. This module was chosen based on COMSOL's recommendation and my interest in the EF generated in the highly conductive, liquid portion of the system. EF within

the system was obtained by considering current to be conserved throughout the model space using the Maxwell Equation $\nabla\bullet[-\sigma\nabla V] = 0$. Electric field was evaluated using the relation $E=-\nabla V$. The electric flux was obtained using Ohm's law for diffuse media: $\mathbf{J} = \sigma\mathbf{E} + \mathbf{J_e}$ where σ is electrical conductivity, $\mathbf{J}$ is electric flux, $\mathbf{J}_e$ is current flux generation (zero in my model), and $\mathbf{E}$ is the EF. Electrical field is related to electric displacement, $\mathbf{D}$, via $\mathbf{D} = \varepsilon_0\varepsilon_r\mathbf{E}$ where ε_r is the dielectric constant and ε_0 is permittivity in vacuum. A current flux boundary condition calculated to create a 23.4 mV/mm field across the cell culture portion of each device was assigned to the positive lead. The negative lead was assigned as a ground.

The electrical conductivity (σ) of cell culture medium was taken as 1.5 S/m and the dielectric constant (ε_r) as 80 [135]. The electrical conductivity of phosphate buffered saline (PBS) was 1.5 S/m [136] and the dielectric constant was assumed to also match that of medium. The agarose was assumed to have the same electrical properties as PBS. The conductivity and dielectric constant of PLA material were taken as 7×10^{-17} S/m and 3.25 respectively [137]. Ag/AgCl electrodes and leads were modeled as pure silver with σ as 61.6×10^6 S/m and the dielectric constant as one.

All models were meshed with an extra fine free tetrahedral mesh with a maximum element size of 0.889 mm, a minimum size of 0.22 mm, and a maximum growth rate of 1.35. The resulting mesh had approximately one million nodes. A mesh independence study was conducted on the electric potential at the center of the cell culture chamber, based on the number of mesh elements per volt, from 0.5 to 6.5 elements per volt at an interval of 1.0 (element size was defined as $\frac{l}{Vn}$, where l is the distance between electrodes, V is the voltage, and n is the number of elements per volt). Solutions were found using a well-preconditioned, iterative, conjugate gradients solver. For each device, electric potential and the EF lines were generated and all plots were set to the same scale for comparison.

Based on simulation results, a few prototypes were chosen and printed using polylactic acid (PLA) filament in a MakerBot Replicator 5. A layer height of 0.2mm, with a raft on an unheated build plate, with solid infill to decrease porosity and improve liquid retention was used. A circular transparent window was incorporated into the bottom of the device by attaching an 18mm round microscope coverslip with silicone adhesive. Electrode placement varied, however permanently placed electrodes were also secured with silicone adhesive and wires were insulated with silicone. Based on comparisons between multiple devices, a device without physical barriers was chosen for cell culture testing. Further, additional dams were added to mold micro wells around disc electrodes that were filled with medium and would allow gasses to escape without breaking the circuit **(Figure 4.3a**). Disc electrodes were placed against the walls with silicone adhesive and agarose was poured to isolate the electrode from culture medium. To evaluate the effect of agarose concentration in the outer chambers on the power required to run the device, 0.5%, 1.0%, and 2.0% (w/v) agarose concentrations were used. Dams were removed after agarose solidified.

4.2.3 Evaluating Galvanotaxis of Neuroblasts and Adipose Derived Stem Cells

IMR-32 neuroblasts (CCL-127) and StemPro hASCs were cultured according to the manufacturers' protocols. Briefly, NBs were cultured in EMEM with 10% FBS. Medium was changed three times per week. hASCs were cultured in MesenPRO RS medium with 10% Growth supplement and 2mM L-glutamine. Medium was changed every 3-4 days. Both cell types were incubated in a humidified chamber at 37°C, 5% CO2, 95% air. When confluent, NBs were suspended using 0.5% trypsin-EDTA, centrifuged at 125×g for 5 minutes, and re-suspended in fresh medium. When confluent, hASCs were rinsed with Dulbecco's Phosphate Buffered Saline, and suspended in pre-warmed TrypLE Express. Viable cells were counted using a hemocytometer and trypan blue. hASCs were used at passage 3. 18mm square microscope coverslips were coated with 0.1% gelatin, and air dried in a biosafety cabinet. After drying, each cover slip was placed in a 6-well plate. Both hASCs and NBs at 22.2×10^3 cells were pipetted onto the coverslips. On day 2 or 6 after seeding,

a coverslip was transferred into a prepared galvanotaxis device using sterile forceps, and the device was placed into a sterile petri dish and wrapped with parafilm. The stage ring of a Nikon Eclipse TE2000-U inverted microscope was replaced with a Nikon Thermo Plate, which was maintained at 37 °C. The galvanotaxis device was placed on the thermo plate and cells were continuously monitored using the attached CCD camera (**Figure 4.3c**). For stimulation, 3 mA direct current was applied using a PowerEase® 500 Power Supply (Invitrogen, Carlsbad, CA). Digital micrographs were acquired at 15 min intervals. Some cultures without pre-stained cells were evaluated via immunostaining using both fluorescent microscopy and flow cytometry.

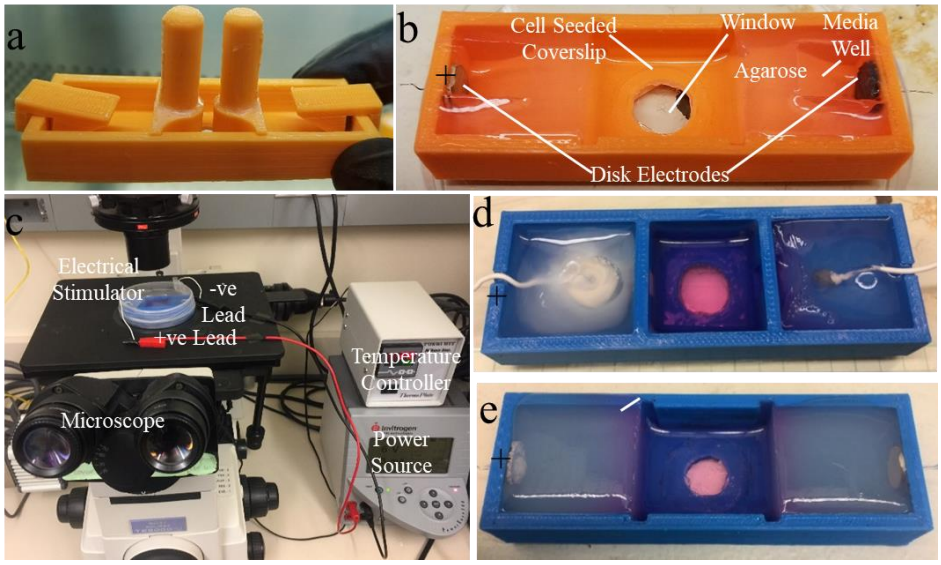

Figure 4.3: Testing novel galvanotaxis devices. a) Parts of the electrical stimulator prior to agarose pour. b) Various parts of the stimulator with electrodes and agarose. c) Assembled view of electrical stimulation setup. (d) Appearance of agarose after experimentation with point electrodes and one-hole configuration. (e) Appearance of agarose after experimentation with disc electrodes without physical barrier.

Using digital micrographs, the area, major axis length, minor axis length, and shape factor of individual cells were measured using Sigma Scan Pro (Systat Software, San Jose, CA), similar to our previous publication [138]. Cells with observable borders were analyzed manually. Also, cells suspended in cell culture medium were evaluated. For each condition, various numbers of cells

were analyzed. Obtained parameters were exported to Microsoft Excel (Redmond, WA) for statistical analysis. First, mean, standard deviation, variance and standard errors were calculated for each condition to determine significant differences between groups. Where the variance was homogenous, ANOVA analysis was used along with Tukey post hoc tests. In conditions, where variances were not homogenous, a Welch Test was performed along with Scheffé's post hoc tests.

4.2.4 Immunostaining

To understand the effect of stimulation, samples were immunostained for neurite outgrowth (β-III tubulin), nuclei (DAPI), and actin (Alexa Phalloidin), using previous published protocols [139]. In brief, samples were fixed in 3.7% formalin for 30 minutes, washed 3 times with PBS, and permeabilized in 0.1% Triton X-100 in PBS for 30 min at room temperature. Samples were blocked for 60 minutes using 2.5% nonfat milk (prepared in PBS), incubated in mouse anti β-III tubulin in 2.5% nonfat milk (1:500) for 60 minutes at room temperature, washed 3 times with Hepes Buffered Salt Solution (HBSS) for 5 minutes then incubated with goat anti mouse Alexa Fluor 488 (1:1000), DAPI (1:1000), and Alexa Fluor 546 Phalloidin (1:1000) in 2.5% nonfat milk. Samples were rinsed 3 times with HBSS for 5 min, prior to mounting the coverslip. Florescent images were captured using Nikon Eclipse TE2000-U inverted microscope with attached CCD camera and Prior Scientific Lumen 200 florescence illumination system, using Nikon UV, FITC, and TRITC filters.

4.3 Results and Discussion

4.3.1 A Compact Galvanotaxis Device

While mechanical stimulation devices have been miniaturized for use in sterile conditions, there are no miniaturized devices to study galvanotaxis. Currently available galvanotaxis devices have a custom made glass chamber for cell culture observation along with tubes filled with an agar solution (typically 1-2%), [22, 24, 140] and salt bridges connecting the electrodes, placed in glass beakers filled with isolated electrolytic solutions, and the cell culture chamber. These devices are

cumbersome and require biosafety cabinets to maintain sterility for long term culture post-stimulation. I sought to develop a compact device that would allow us to expose cells to a constant EF without compromising either sterility, or prevent us from observing cells during exposure via light or fluorescent microscopy. I coupled finite element analysis with 3D printing. Three criteria used in designing a galvanotaxis device were: i) obtaining a constant EF so that all cells are subjected to the same stimulus; ii) isolating ionic products generated by the electrodes; and iii) increasing portability while maintaining sterility. With the low of cost custom-printing devices using 3D printing, one could consider making these devices disposable.

Initial designs contained physical barriers to separate the cell culture chamber from electrodes. Since physical barriers are poor electrical conductors, holes were created to facilitate conductivity along the barrier. As can be seen in **Figure 4.4(a-c)**, non-uniformity in the voltage gradient and deformation of the EF lines (in black), caused by distortions of the EF near physical walls change the average EF across the chamber. Further analysis of the electrical potential across the cell chamber demonstrated this non-linearity (**Figure 4.4h**). This is unlike a galvanotaxis device, reported in literature, which creates a uniform EF, with parallel EF lines (**Figure 4.4g**). Nevertheless, I tested the prototype in **Figure 4.4a** and observed increases in resistance with time. Resistive heating (electrical heating is proportional to resistance $P \propto I^2R$) caused agarose to dry at the positive electrode (**Figure 4.3d)**. I considered altering the conductivity of agarose surrounding the electrodes. Agarose gels have decreased conductivity with increased polymeric concentration [141]. Although 2.0% (w/v) agarose is used for electrical stimulation of cardiac cells [140], this caused the run to end prematurely within 1 hour. I tested 0.5% and 1% agarose and prepared them in phosphate buffered saline to improve conductivity. With 0.5% agarose bubble formation near the electrode decreased and run time also extended. I needed to minimize resistance throughout the device. Since culture medium has essential electrolytes needed based on the extracellular fluid composition, there is little option in changing the conductive properties of cell culture medium.

However, the electric flux depends on the cross sectional area through which the current flows over cells. Therefore, with a constant EF, decreasing the media height or width of the stimulator chamber was an option. I reduced the volume in the stimulator to 2mL.

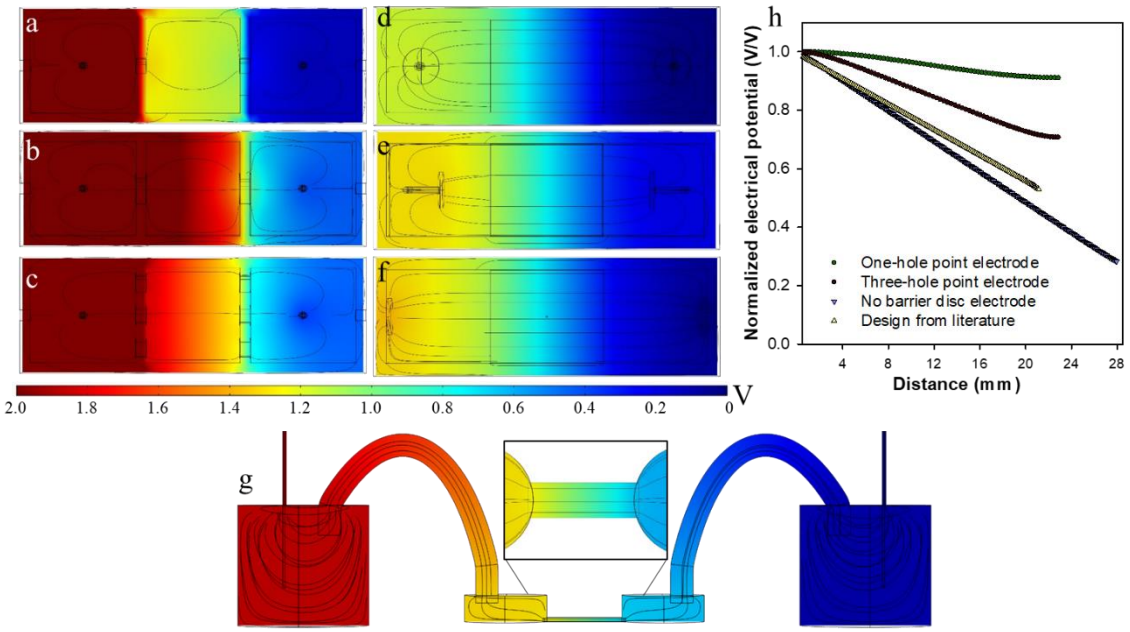

Figure 4.4: Various design patterns for galvanotaxis. (a-c) compact devices incorporating physical walls and point electrodes (2mm) with different hole configurations: a) a single 3.81mm hole, b) a single 7.62mm hole, and c) three 5.00mm holes located at the center and 3.15in (8.00mm) to either side. (d-f) A compact design without physical walls using disk electrodes located: d) against the stimulator floor e) parallel at the same distance as the point electrodes, and f) with the electrodes located against the outer walls. g) An example of a multicomponent galvanotaxis device similar to those commonly found in literature [23]. Rainbow graphs are electrical potential, in volts. Black lines are electrical field lines, in black. h) Changes in electrical potential (normalized to the maximum potential) across the cell culture chamber.

I considered developing devices without physical walls and using disk electrodes to further minimize resistance and spread the current over a larger area to reduce localized heating. These changes decreased the overall electric potential required to maintain the desired EF in the cell culture chamber, eliminated sharp changes in the voltage, and exhibited parallel EF lines (**Figure 4.4d-f**). In addition, the electric potential gradient across the cell chamber was linear and the slope (i.e. the EF) was similar to the galvanotaxis device used in literature (**Figure 4.4h**): since the input current

flux was calculated from the desired, constant EF, the electric potential gradient was constrained to a constant value in all designs. The orientation of the disk electrodes did not affect the EF significantly. I chose to place the electrodes at the ends of the chamber to i) increase path length of salt bridges, ii) fix the distance between electrodes, and iii) to ensure reproducible electrode placement. When testing this prototype, agarose drying decreased significantly **(Figure 4.3e)**, which improved run times to the required 3.5 hours. I isolated the electrode leads from the system by passing them through holes in the ends of the devices and placing electrodes with silicone adhesive. I also created small wells between the agarose and electrodes which I filled with medium to allow generated gasses to escape.

4.3.2 Galvanotaxis is Dependent upon Culture Duration

Electrical field measurements in wound healing demonstrate endogenous electric fields, up to 200 mV/mm. Based on these results, some have applied electrical fields to in vivo conditions to promote wound healing [142]. Further, rat dorsal root ganglia have been shown to align vertically in a DC electric field[23]. I questioned how this would translate to *in vitro* cultures. Unlike traditional galvanotaxis devices, my entire chamber fit inside a 100 mm petri dish wrapped with parafilm. The device was easy to transport and fit on the heated stage of an inverted microscope (**Figure 4.3c**). No contamination was observed 6 days after exposure when the coverslip was transferred to a 6-well plate following experimentation.

To test the influence of the compact device on cell orientation, I first stimulated NBs. NBs responded to a 23.4 mV/mm EF (calculated from a 3mA direct current supplied to the stimulator). However, NBs showed little reaction to electrical stimulation after culturing for one (**Figure 4.5a**) or two days (data not shown): there was no perceptible change in orientation or size of NBs over the 3.5 hr EF exposure period. However, when cells were cultured for 6 days prior to stimulation, cell response was perceptible after 60-90 min of stimulation. Many NBs seeded directly (Control group) responded by changing their orientation (**Figure 4.5b**) and aligning vertically as compared

to the unstimulated control after 6 days of culture. This result may indicate galvanotaxis in NBs is cell density dependent: cell-cell interactions may be required for NBs to detect and align to the EF. I quantified NB surface area, shape factor, major length and minor length to understand changes in cell phenotype. These results showed (**Figure 4.5c**) a reduction in surface area with a constant shape factor. After stimulation, cell surface area appeared to be similar to that of NBs suspended in cell culture medium. This could suggest that applied current causes cell detachment. However, comparison of the cell shape (**Figure 4.5c**) indicated a shape similar to that of adherent cells. Further, the major length of stimulated cells was significantly higher than suspended cells. However, the minor length was significantly smaller than the adherent cells. To better understand changes in cell thickness, I calculated cell volume from suspended cells using the equation of an ellipsoid and average minor length and major length values. NB volume was 2650 (±727) μm^3. Assuming NB volume remains constant (i.e., no change in osmotic pressure), I calculated cell thicknesses at various conditions using surface area. Adherent NBs had 7.4 (±2.00) μm thickness, significantly smaller than minor cell length in suspension. After electrical stimulation, NB thickness increased to 13.4 (±3.45) μm, which is still less than that of NBs in suspension. This suggested that the NBs are not detaching from the surface but their thickness increases. Nevertheless, I stained some samples with i) β-III-tubulin, an early intracellular marker indicating a neuron-like cell, ii) DAPI nucleic stain, and iii) phalloidin, an actin stain. Intracellular actin was observed in NBs, confirming cell attachment to the substrate after EF stimulation (**Figure 4.5d**). Moreover, cells lacked β-III tubulin prior to stimulation but expressed diffuse β-III tubulin expression after 3.5 hr of stimulation. These results indicate that NBs respond similar to other neural cells subjected to an EF [23] and that the application of an EF might cause NBs to become more neuron-like without causing depolymerization of actin.

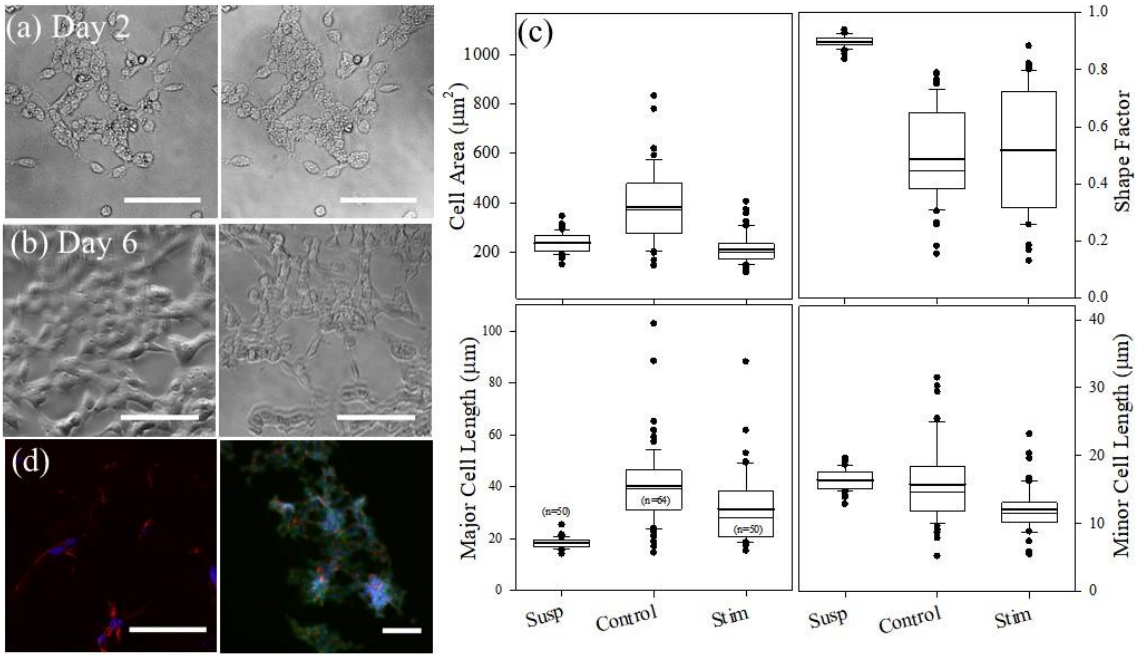

Figure 4.5: Effect of Stimulation and Culture Duration on NBs. The left image of each pair is before stimulation and the right after stimulation. NBs seeded onto coverslips and stimulated on a) day 1 and b) day 6. (c) Box and whisker plots showing the median, mean (thick line within the box), interquartile range box, and whiskers corresponding to 95 and 5 percentiles of area, shape factor, major length and minor length. n value corresponds to number of data points in each condition. Also, print condition corresponds to NBs printed through a 34g needle. (d) Immunostained for B-III tubulin (green), DAPI (blue), and actin (red). Scale bars are 100μm and current passes left to right (anode on left and on cathode right).

Since NBs are cancerous progenitor cells, I wanted to understand the effect on a cell lineage that could be used in clinical setting. For this purpose, I used hASC. Based on NB experiments, I first performed stimulation experiments after six days of incubation. I did not observe significant EF effect on hASC (**Figure 4.6a**). Further, on day 6, there was no change in spread or orientation due to stimulation. I questioned whether the long term culture could diminish sensitivity and stimulated the hASC after one day of incubation. These results (**Figure 4.6b**) showed significant EF effects, unlike NBs on day 1, suggesting a culture duration dependent cell response to galvanotaxis. Also, day one hASC responded within 15 min to EF, much faster than day 6 NBs, (60-90 min). To understand changes in hASC phenotype, I quantified the surface area, shape factor, major length and minor length from day one cultures. These results showed (**Figure 4.6c**) a reduction in surface area after EF stimulation while the shape remained the same; cell surface area reduced to nearly

that of cells in suspension in culture medium, similar to NBs. However, comparison of the cell shape indicated a shape similar to that of adherent cells, unlike cells in suspension, which is nearly circular. The reduction in cell area was primarily contributed by a significant reduction in major length, unlike NBs. Minor axis also decreased marginally relative to adherent cells. Similar to NBs, I calculated hASC volume when suspended. The average hASC volume was 21900 (±11000) μm^3, nearly 8.26 times larger than NB volume. Next, I calculated cell thickness when attached and after electrical stimulation using respective surface areas. These results showed that the adherent cells had 6.8 (±3.27) μm thickness, which is significantly smaller than minor cell length in suspension. With the electrical stimulation, cell thickness varied significantly in the population 35(±36.2) μm. NB and hASC shapes are significantly different based on Tukey post hoc test with $p<0.01$. Since the variances of cell area, major length and minor length between NB and hASC were non-homogenous, I performed Schiff tests. These analyses confirmed that there are significantly different with $p<0.01$.

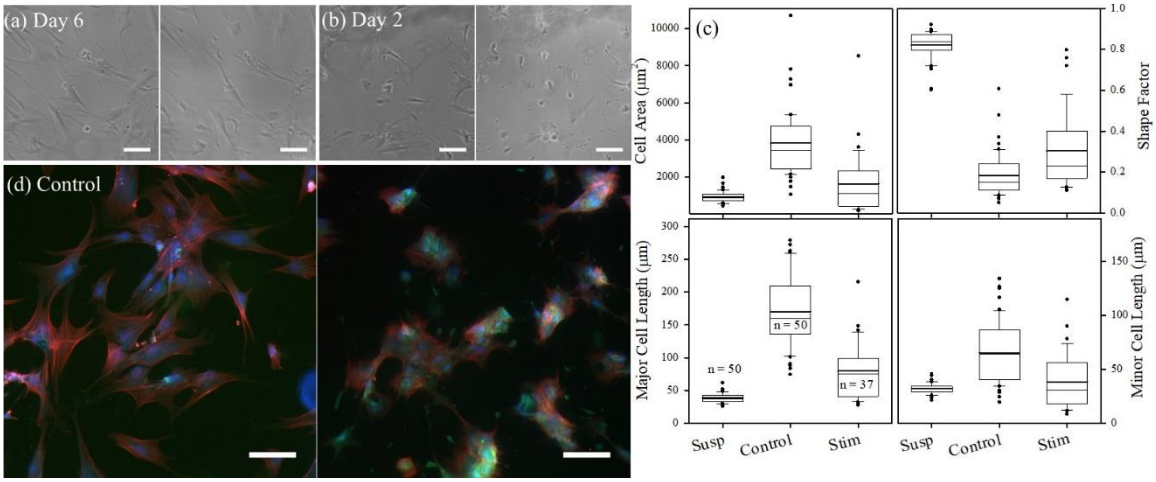

Figure 4.6: Effect of Stimulation and Culture Duration on hASCs. The left image of each pair is before stimulation and the right after the end of stimulation. hASCs seeded onto coverslips and stimulated on (a) day 2 and (b) day 6. (c) Box and whiskers plots showing the median, mean (thick line within the box), interquartile range box, and whiskers corresponding to 95 and 5 percentiles of area, shape factor, major length and minor length. n value corresponds to number of data points in each condition. (d) Day 1 cultures immunostained for B-III tubulin (green), DAPI (blue), and actin (red). Scale bars are 100μm and current passes left to right (anode on left and on cathode right).

I stained some samples with β-III-tubulin, DAPI, and phalloidin as before. Immunostained hASCs on day one, showed some diffuse expression of β-III tubulin without a loss of filamentous actin, immediately after the 3.5 hr exposure to EF, similar to NB response on day 6 (**Figure 4.6d**). This indicates that hASCs may be differentiating toward a neural lineage and change in cellular shape does not indicate a loss of attachment, supporting my conclusion that cells are not detaching due to EF exposure.

4.4 Discussion

My galvanotaxis device demonstrates how 3D printing technologies can be leveraged by researchers within the tissue engineering community to create devices that overcome the drawbacks of traditional laboratory setups. Moreover, these devices are inexpensive to produce. In addition, I utilized one model per design, which was imported into COMSOL for simulation and then directly printed using a 3D printer. Therefore, the entire design phase was conducted using a single model: I simulated the EF, rapidly printed and tested prototypes, refined my design via additional simulations and printing of prototypes and then printed multiple 'production' units. This approach could be applied to numerous devices used by tissue engineering researchers to replace cumbersome setups assembled from readily available laboratory materials and designs can be shared digitally between researchers, allowing custom devices to rapidly spread preventing other laboratories from conducting unnecessary design work.

I found a surprising dependence of cell function on culture time. Cell culture experiments tend to be conducted approximately 24 hr after seeding, if the culture time is reported at all. As mentioned previously, this difference is easily observed when exposing cells to EFs, however the dependence would be much less clear when exposing cells to chemical signals. Therefore, culture duration may also play a significant role in ADSC differentiation. I find a strong time-dependent difference in cell response with culture time post seeding, independent of passage number. In addition, I observed a distinctly different effect of culture time on the two cell types investigated. I cannot state

whether this is necessarily a concentration based or purely time-dependent phenomena. It is possible that galvanotaxis is dependent upon the growth phase in which the cell lines are found. However, NB carcinoma respond to an EF after 6 days, while ADSCs respond on day 2. NB do not respond noticeably to EF on day 2, and ADSCs do not respond noticeably on day 6. In addition, NB are not confluent on day 6, reducing the likelihood that the cellular response I are observing is due to a change in the growth regime.

It was interesting that I observed a lack of response from ADSCs with increased culture time and at a higher cell density. My micrographs did not show visual confluency, so I do not expect that contact inhibition is an issue. Moreover, it is known that the stem cell pool has increased cell number later in life with decreased functionality. I hypothesize that stem cell concentration may play an important role in the population's ability to differentiate.

While the evidence presented in this work suggests that culture time is important when considering cell responses, additional work may lead to a clearer understanding of what cells are experiencing. First, trypsin is well known to damage CAMs. Therefore, investigating the galvanotactic response of cells cultured on poly-NIPAM treated cell culture dishes to eliminate trypsin may be of interest. Poly-NIPAM is a thermally responsive polymer that has been shown to cause cell detachment when the temperature is lowered from 37°C to room temperature [143]. Use of this polymer coated cell culture dish is expected to prevent CAM damage from trypsin and will ensure that the responses I observe are not caused by trypsinization. Second, use of neural culture medium, instead of continuing to culture cells in hASC medium, might be expected to increase the number of cells that express β-III-tubulin.

4.5 Conclusions

In this work, I successfully developed a compact stimulator with uniform electrical field using computational simulation to obtain a uniform electrical field and 3D printed devices of interest. I

tested these devices on NB and hASC. I observed that NB and HADSCs respond to EFs with vastly different culture times. I demonstrated that β-III-tubulin expression and galvanotactic response is affected by the time in culture. Overall, I demonstrate that culture time is important when considering cell responses, and that the observed effect is not a function of increasing concentration for NB, which may be true for stem cell differentiation as well. My findings may tie in with others that the stem cell pool increases in population with age while their utility decreases and indicates that it is possible that the relationship between population and utility is causal.

CHAPTER V

BIOPRINTING CHANGES CELL MORPHOLOGY, EXPRESSION, AND RESPONSE TO AN ELECTRICAL FIELD

5.1 Introduction

Despite their acceptance by the medical community and use in clinical settings, premade scaffolds are difficult to shape into complex geometries and require random cell seeding—preventing control of the arrangement and distribution of different cell types. While some cell types may self-assemble into the proper spatial relation, this process does not always occur and is usually lengthy. Bioprinting provides a viable solution: it allows spatial location of multiple cell types in relation to one another and the creation of complex, multicellular tissue analogs and reduces reliance on cell self-assembly. However, bioprinting processes often damage cells, decreasing their viability and possibly altering cell functionality. There is limited understanding of the effects of crosslinking mechanisms on cell processes post-printing.

In this work, I investigated and compared the effect of bioprinting on neuroblasts (NBs) and human adipocyte stem cells (hASCs) in both cell culture medium and chitosan-gelatin (CG) hydrogel explored in Chapter 3. In order to test the effect of bioprinting, I used the compact galvanotaxis device, developed in Chapter 4. These results show that some human adipocyte stem cells differentiate towards neuron-like cells after bioprinting and culturing up to 6-days.

5.2 Materials and Methods

5.2.1 Materials

Low molecular weight chitosan (50 kDa and 75-85% deacetylation), gelatin (300 bloom, Type A, from porcine skin), and agarose powder were purchased from Sigma Aldrich Chemical (St. Louis, MO). β-glycerophosphate was purchased from Santa Cruz Biotechnology, Dallas TX. IMR-32 Neuroblasts, Eagle's minimum essential medium (EMEM), Fetal Bovine Serum, and 0.05% Trypsin-EDTA were purchased from The American Type Culture Collection (ATCC – Manassas, VA). StemPro Human Adipose-Derived Stem Cells, MesenPRO RS Medium, MesenPRO RS Growth Supplement, L-glutamine, Dulbecco's phosphate-buffered saline (DPBS), TrypLE Express, Carboxyfluorescein diacetate succinimidyl ester (CFDA), Live/Dead Cell Vitality Assay Kit (C_{12} Resazurin/SYTOX), Alexa Fluor 488 goat-anti-mouse IgG2a antibodies (A-21131), 4',6-Diamidino-2-Phenylindole, Dihydrochloride (DAPI), and Alexa Fluor 546 Phalloidin were purchased from ThermoFisher Scientific (Waltham, MA). TUJ1 clone anti-β-III tubulin mouse primary IgG2a antibodies were purchased from Biolegend (801201; San Diego, CA). Ag/AgCl point electrodes were purchased from In Vivo Metrics (Healdsburg, CA). Ag/AgCl disk electrodes (9mm diameter and 1mm thick) were purchased from ALA Scientific Instruments (Farmingdale, NY). Polylactic acid (PLA) printer filament was obtained from MakerBot (New York City, NY). Silicone adhesive was obtained from Lowes (Stillwater, OK).

5.2.2 Evaluating Galvanotaxis of Bioprinted Neuroblasts and Adipose Derived Stem Cells

IMR-32 neuroblasts (CCL-127) and StemPro human Adipocyte Stem Cells were cultured according to the manufacturers' protocols. Briefly, NBs were cultured in EMEM with 10% FBS. Medium was changed three times per week. hASCs were cultured in MesenPRO RS medium with 10% Growth supplement and 2mM L-glutamine. Medium was changed every 3-4 days. Both cell types were incubated in a humidified chamber at 37°C, 5% CO2, 95% air. When confluent, NBs were suspended using 0.5% trypsin-EDTA, centrifuged at 125×g for 5 minutes, and re-suspended in

fresh medium. When confluent, hASCs were rinsed with Dulbecco's Phosphate Buffered Saline, and suspended in pre-warmed TrypLE Express. Viable cells were counted using a hemocytometer and trypan blue. hASCs were used at passage 3. 18mm square microscope coverslips were coated with 0.1% gelatin, and air dried in a biosafety cabinet. After drying, each cover slip was placed in a 6-well plate. Both hASCs and NBs at 22.2×10^3 cells were added on to the coverslips in two different ways and incubated until further analysis

(i) *Printed using cell culture medium*: Cells suspended in cell culture medium (2×10^6 cells/mL) were printed directly on to the slides using a 34-g (60-μm nozzle diameter) or 32-g (102-μm nozzle diameter) needles. All bioprinting was done at the optimized condition described in Chapter 3: 30 μL/min flow rate and at a feed rate of 100cm/min using my custom-built bioprinter .

(ii) *Printed using CG hydrogel solution*: Cells were mixed with CG thermosensitive solution as described in the next section, and printed at conditions similar to the cell culture medium.

Printed constructs with cells were placed in an incubator for one hour, prior to adding 2mL of culture medium. On day 2 or 6 after seeding, a coverslip was transferred into a prepared galvanotaxis device using sterile forceps, and the device was placed into a sterile petri dish and wrapped with parafilm. The stage ring of a Nikon Eclipse TE2000-U inverted microscope was replaced with a Nikon Thermo Plate, which was maintained at 37 °C. The galvanotaxis device was placed on the thermo plate and cells were continuously monitored using the attached CCD camera (**Figure 2c**). For stimulation, 3 mA direct current was applied using a PowerEase® 500 Power Supply (Invitrogen, Carlsbad, CA). Digital micrographs were acquired at 15 min intervals. Cells stained with the non-toxic, cytoplasmic stain CFDA-SE were observed with the florescence illumination system. Stimulation periods were chosen based upon control cellular response. To avoid photo-bleaching, fluorescent images were acquired prior to stimulation, at 90min, and at the end of the stimulation. Some cultures without pre-stained cells were evaluated via immunostaining using both fluorescent microscopy and flow cytometry.

5.2.3 Printing Cells using CG hydrogel solution

3%-3%, 2%-8%, and 1%-8% chitosan-gelatin solutions (%chitosan-%gelatin, w/V) were prepared in deionized water, similar to Chapter 3. Briefly, the solutions were sterilized using dry heat at 120°C for 30 minutes in tightly sealed bottles. Then, 200µL of hydrochloric acid (37%) was added, per gram chitosan, in a sterile hood. The prepared mixture was stirred on a heated stir plate overnight at 58°C. Immediately prior to use, the solution was centrifuged and the supernatant transferred to a new tube to remove particulates. Then β-glycerophosphate was slowly added to the solution until it reached a pH of 7.20-7.40 and centrifuged again to remove bubbles. Then cells were added and the cell-hydrogel mixture was printed using my bioprinter, as described previously [144]: Cells were stained with 2-4 µM CFDA-SE in phosphate buffered saline (PBS), washed with PBS, mixed into prepared hydrogel at a concentration of 2×10^6 cells/mL, loaded into a 1-mL syringe and printed using either a 34-g or a 32-g needle. Since the intent was to test the effect of printing and then electrical stimulation, 1.8cm long fibers were printed in parallel with 2.0 mm spacing between them onto gelatin-coated coverslips placed inside 6-well plates. After printing, the plates were placed in an incubator for one hour to allow for gelation to complete, 2 mL of culture medium were added, and the plates were returned to incubation and routine culture until further analysis one or six days later.

5.2.4 Electrical Properties of Hydrogel and Cell Culture Medium

The electrical properties of hydrogel formulations and cell culture medium were measured using a Hach SensION5 (Loveland, CO). Hydrogel was mixed and transferred into the measurement chamber of the device's probe, wrapped in parafilm, and incubated at 37°C for 30 min to allow the hydrogel to gel. After the 30 min incubation, the parafilm was removed and the probe was placed in a 50 mL centrifuge tube with 20 mL of cell culture medium and equilibrated for 30 min before recording the conductivity value. Measurements were taken for three preparations of 1%-8%, 2%-8%, and 3%-3% hydrogel each. The average and standard deviation were calculated. Medium

electrical properties were measured by placing the probe into 20mL of medium pre-warmed to 37°C and immediately taking the measurement.

5.2.5 Immunostaining for Microscopy and Flow Cytometry and Viability Analysis

To understand the effect of stimulation or bioprinting, samples were immunostained for neurite outgrowth (β-III tubulin), nuclei (DAPI), and actin (Alexa Phalloidin), using previous published protocols [139]. In brief, samples were fixed in 3.7% formalin for 30 minutes, washed 3 times with PBS, and permeabilized in 0.1% Triton X-100 in PBS for 30 min at room temperature. Samples were blocked for 60 minutes using 2.5% nonfat milk (prepared in PBS), incubated in mouse anti β-III tubulin in 2.5% nonfat milk (1:500) for 60 minutes at room temperature, washed 3 times with Hepes Buffered Salt Solution (HBSS) for 5 minutes then incubated with goat anti mouse Alexa Fluor 488 (1:1000), DAPI (1:1000), and Alexa Fluor 546 Phalloidin (1:1000) in 2.5% nonfat milk. Samples were rinsed 3 times with HBSS for 5 min, prior to mounting the coverslip. Florescent images were captured using Nikon Eclipse TE2000-U inverted microscope with attached CCD camera and Prior Scientific Lumen 200 florescence illumination system, using Nikon UV, FITC, and TRITC filters.

Some samples were immunostained as described above, except cells were detached from the surface, then fixed and stained in suspension for flow cytometry (FACSFlow, BD Biosciences). Cells were stained at 4°C.

hASCs were printed using culture medium through a 32g needle followed by a 5-day incubation for viability analysis, similar to that used previously for NB viability [144]. Non-printed hASCs were used as controls. On day 5, the cells were stained with the C_{12} Resazurin/SYTOX live/dead assay kit according to the manufacturer's protocol and our previous work [144]. Briefly, cells were washed with DPBS then detached from tissue culture plastic using TrypLE express. Then hASCs were spun down at 210xg for 5 min and re-suspended in 100µL of PBS with 500nM C_{12} Resazurin

and 20nM STYOX green and incubated for 15 minutes. After incubation, hASCs were placed on ice and immediately analyzed by flow cytometry.

5.3 Results and Discussion

5.3.1 Bioprinting Affects Cellular Morphology and Expression Differently.

To understand the effect of shear stress during bioprinting on cell function, NBs suspended in culture medium were printed using 34g (60 μm internal diameter) and 32 g needle (120μm internal diameter). In Chapter 3, I reported that NBs printed through a 34g needle, in culture medium, maintain high cell viability, similar to that of unprinted NBs. To extend those analyses, I compared cell phenotypic characteristics. Interestingly, without stimulation, more NBs appeared to be aligned when printed through a 34g needle (**Figure 5.1b**) relative to printing through a 32 g needle (**Figure 5.1c**) or non-printed samples (**Figure 5.2a**). To understand the difference in shear stress experienced by the cells, I used the viscosity of water at 25 °C and the 30 μL/min flow rate used during bioprinting to calculate shear stresses for laminar conditions (the Reynolds number was approximately 15). In 34-g needles, the wall shear stress was 26.3 N/m^2. These values decreased by 8.7 fold in 32-g needles, where the wall shear stress was 3.01 N/m^2. Thus, the higher shear stress may assist cell alignment. In any case, bioprinting increased NB surface area (**Figure 5.1g**) significantly relative to stimulated or unstimulated cells. However, cell shape increased towards suspended cells. This increase in circularity was mainly due to increased minor length, which resulted in decreased cell thickness to 4.4 (±1.83) μm. Based on NB response to EF stimulation after a 6-day incubation in directly seeded cells (**Figure 5.1a**), I stimulated printed NBs 6 days post-printing (**Figure 5.1b and c**). EF stimulation had an opposite effect on NB morphology compared to stimulation of non-printed cells (**Figure 5.2g**). Bioprinted cells showed similar or marginal improvement in cell spreading area, which was due to increased minor length but almost no change in shape factor or major length. Overall, cell thickness reduced to 3.4 (±0.91) μm, which is significantly smaller than that of stimulated, non-printed NBs.

I questioned how bioprinting could affect a cell type that is more relevant to many synthetic tissue applications. Therefore, I printed hASCs, suspended in culture medium, using a 32g and a 34g needle. Before analyzing phenotypic changes, I performed cell viability analysis, similar to that performed on NBs (i.e., after five days of printing in cell culture medium using a live/dead assay) to ensure that the printing process was not causing cell death. Flow cytometry demonstrated that hASC viability was nearly 81% after printing, compared to a control viability of 88%. Moreover, the injured cell population was 16% for bioprinted cells, compared to 11% for controls. After confirming high viability, similar to my observations of NBs, I compared hASC phenotypic characteristics. Interestingly, bioprinting using a 34g needle (**Figure 5.1e)** or a 32 g needle (**Figure 5.1f**) increased hASC surface area significantly, relative to non-printed hASCs (**Figure 5.1d**), irrespective of stimulation (**Figure 5.1h**). However, hASC shape showed significant elongation concomitant with an increase in major length (**Figure 5.1e and f**). In particular, many cells printed through the 34g needle appeared to have long extruded cytoplasmic tails that had an axonal-like

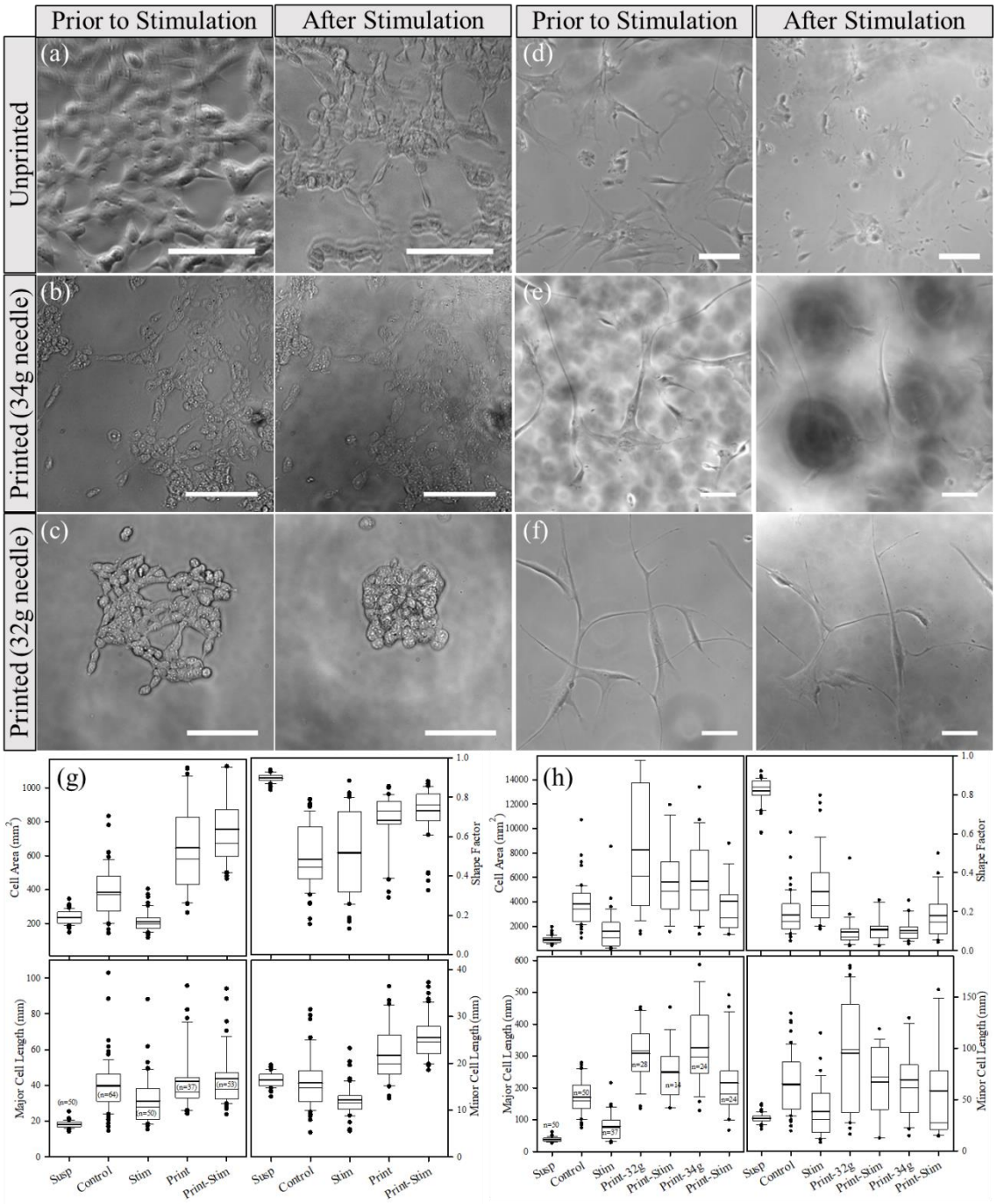

Figure 5.1: Effect of bioprinting in medium and electrical stimulation on cell morphology. The left image of each pair is before stimulation and the right after stimulation. Unprinted NBs (a), NBs printed through a 34g (b) and 32g (c) needle. All NBs were stimulated on day 6. Unprinted hASCs (d), hASCs printed through a 34g (e) and 32g (f) needle. All hASCs were stimulated on day 1. Scale bars are 100µm and current passes left to right (anode on left and cathode on right). Box and whisker plots for (g) NB and (h) hASCs showing the median, mean (thick line within the box), interquartile range box, and whiskers corresponding to 95 and 5 percentiles of area, shape factor, major length and minor length. n value corresponds to number of data points in each condition. Also, for (g), print condition corresponds to NBs printed through a 34g needle

appearance, which reduced the shape factor (**Figure 5.1e**). These variations contributed to the broader distribution of cell morphologies. These effects are opposite to those observed when stimulating NBs (**Figure 5.2g**), despite hASCs' significantly greater cell volume compared to NBs (~8.26 times greater). Nevertheless, increased area resulted in decreased cell thickness to 4.4 (±3.66) μm. Based on hASC response to EF stimulation after a one day incubation in directly seeded cells (**Figure 4.1d**), printed hASCs were stimulated one day post-printing through either a 34g (**Figure 5.1e**) or 32g (**Figure 5.1f)** needle. Unlike NBs, I observed a response similar to non-printed hASCs (**Figure 5.1h**). Bioprinted hASCs showed similar reduction in cell spreading area compared to non-printed hASCs (**Figure 5.1h**), which was due to reduced major length. Cell shape appeared to be similar to that of control cells. Overall, cell thickness did not change.

In addition to morphological evaluation, both NBs and hASCs were evaluated for β-III-tubulin expression (green), for polymerized actin (red), with cells located by nucleic DAPI staining (blue). When printed through a 34g needle, NB polymerized actin expression appeared to be decreased (**Figure 5.2d**) relative to NBs printed through a 32 g needle (**Figure 5.1c**) or non-printed NBs (**Figure 5.2a**). Concurrently, when stimulated, NBs that had been printed through a 34g needle did not express β-III-tubulin or polymerized actin (**Figure 5.2 d**). However, when NBs that had been printed through a 32g needle were stimulated, β-III-tubulin expression and polymerized actin were both expressed, although clearly to a lesser degree than in non-printed samples (**Figure 5.2a**). The partial recovery of expression in NBs printed through a 32g needle suggests that there could be a limit to the level of shear stress that NBs can tolerate. Because of hASCs greater volume, I printed hASCs through a 32g needle. Interestingly, I found that hASCs printed through a 32g needle exhibited no change in polymerized actin (**Figure 5.2f**), compared to non-printed hASCs (**Figure 5.2c**). However, unlike non-printed hASCs, hASCs printed through a 32g needle expressed β-III-tubulin, indicating the shear may induce hASC differentiation towards a neural phenotype.

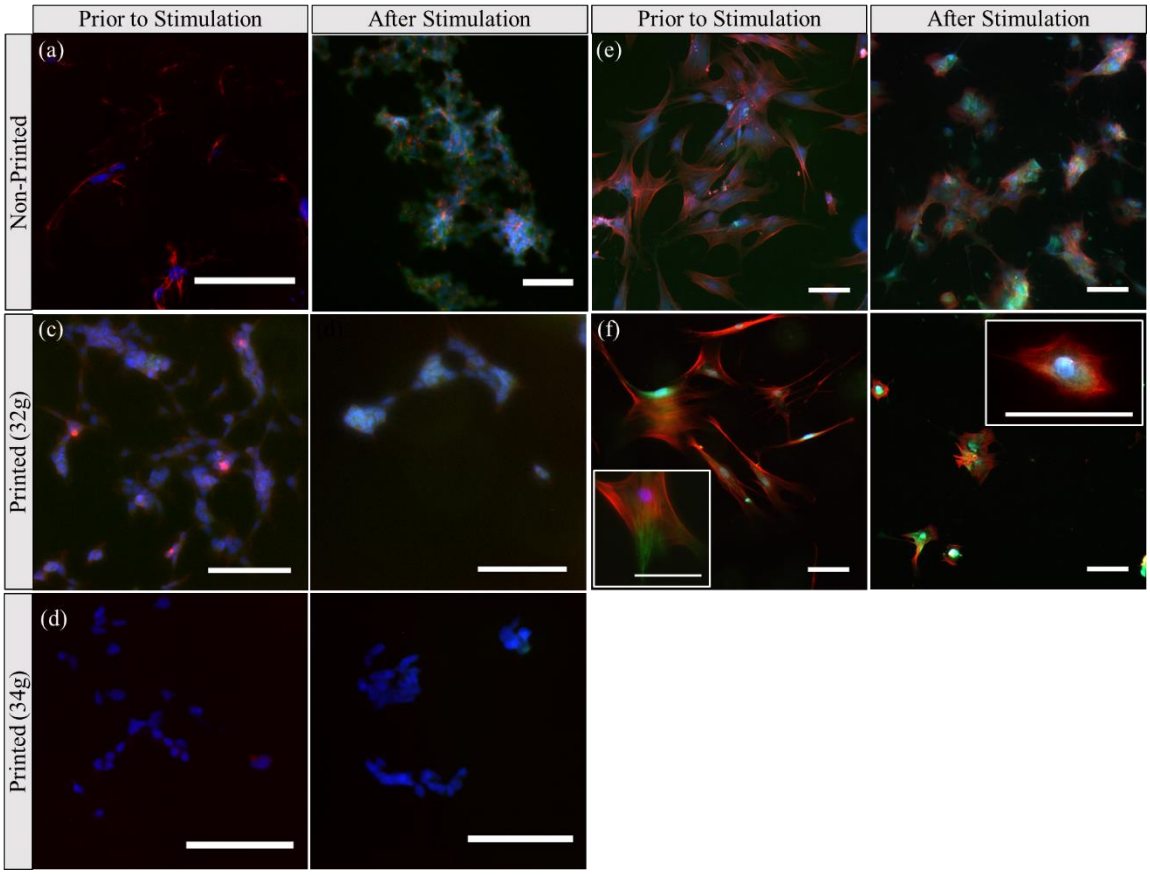

Figure 5.2: Immunocytometry of Printed and Non-Printed Cells. Cells were immunostained for B-III tubulin (green), DAPI (blue), and actin (red). The left image of each pair is before stimulation and the right after stimulation. Scale bars are 100µm and current passes left to right (anode on left and on cathode right). Unprinted NBs (a) compared to NBs printed through 32g (c) and 34g (d) needle. All NBs were stimulated on day 6 and stained immediately after stimulation. Non-stimulated NBs were stained concurrent with stimulated samples. Unprinted hASCs (e) compared to hASCs printed through a (32g) needle. All hASCs were stimulated one day after seeding and stained immediately after stimulation. Non-stimulated NBs were stained concurrent with stimulated samples.

To better understand potential cell differentiation in hASCs, I extended culture to 6 days after bioprinting or 6 days after stimulation. When printed through either a 32g needle (**Figure 5.3a**) or a 34g needle (**Figure 5.3b**), some hASCs exhibited β-III-tubulin across the entire cell surface. In hASC printed through a 34g needle and not stimulated, axonal-like structures containing increased expression of β-III-tubulin, with a very small cytoplasmic region appeared (**Figure 5.3b**, left). This suggests a short exposure to shear rate may be causing stem cell differentiation towards a neuronal phenotype. Interestingly, when EF stimulated cells were cultured for 6-days, many cells showed

increased expression of β-III-tubulin in both 32g and 34g needle printed conditions (**Figure 5.3a, r, right**). In addition, there were many axon-like structures in both conditions. This suggests that EF may influence stem cells to differentiate and that hASC may be subject to greater deformation than NB due to increased cell size. hASCs' relatively greater volume requires more of the needle cross section than NBs' volume and subjects them to higher shear stress nearer to the wall. Recently, higher shear stresses and shear rates, similar to those in a 34g needle, have been reported in bone marrow [145]. These results suggest that the shear rate could play a role in differentiation rather than shear stress. In all cases, there were hASC with abundant actin fibers and without β-III-tubulin expression. One has to evaluate whether non-β-III-tubulin expressing cells are non-differentiated, are muscle cells, or are other lineages. Also, cell wall pliability could decrease with lineage commitment. Showing that the β-III-tubulin cells behave similar to that of neurons would be valuable to confirm differentiation. Also, I cultured hASC in the same culture medium used for their propagation without differentiation i.e., there was no chemical stimulus added to the culture medium. Many have explored differentiating stem cells using various chemical stimulus. I need to test whether culturing hASCs in a lineage specific culture medium would promote faster and more uniform differentiation.

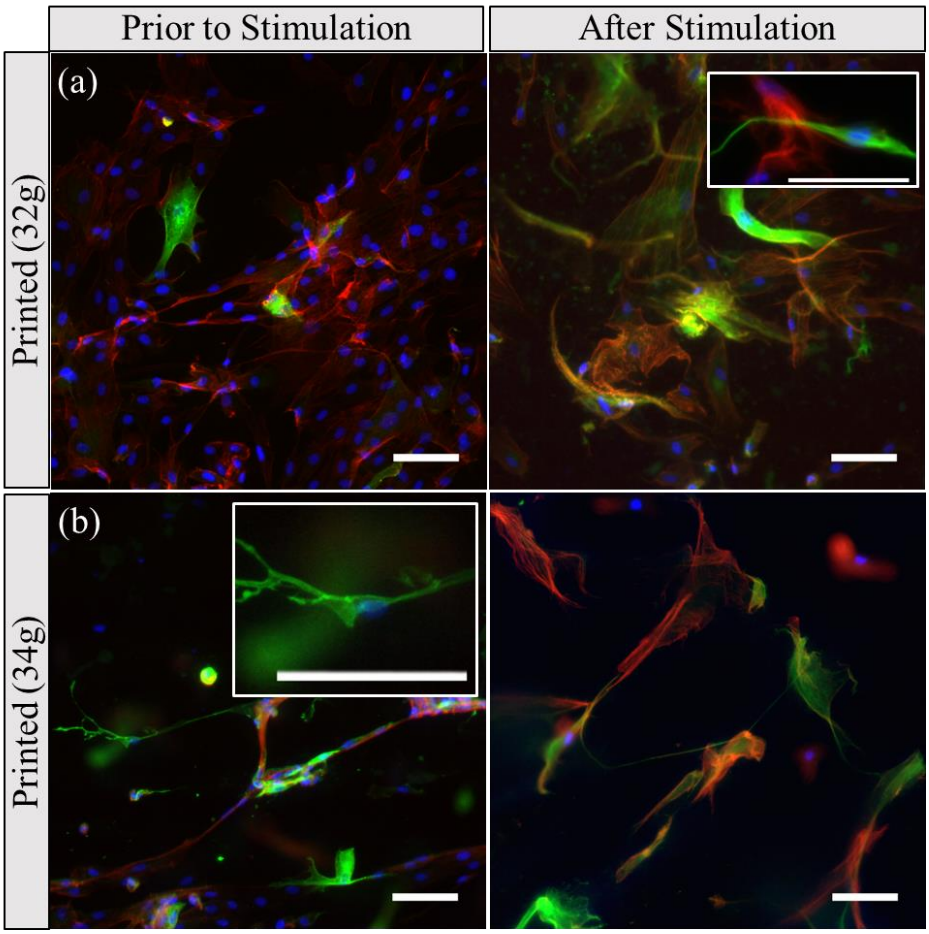

Figure 5.3: Immunocytometery of hASCs Cultured an Additional 6-Days. immunostained hASCs with B-III tubulin (green), DAPI (blue), and actin (red). The left image of each pair is before stimulation and the right after stimulation. Scale bars are 100μm and current passes left to right (anode on left and on cathode right). hASCs printed through a 32g needle (a, left) or 34g needle (b, left) then cultured for 6 days before staining. hASCs printed through a 32g needle (a, right) or 34g needle (b, right), stimulated one day after printing, then cultured for 6 days before staining.

5.3.2 Bioprinting Cell Laden Structures with Thermosensitive Gels Affects Cell Spreading

Bioprinting cell laden structures allows precise placement of cells and matrix elements in a desired location. During 3D bioink development, the focus has been the rapid gelation of fibers to obtain higher resolutions. In Chapter 3, I showed that chitosan-gelatin (CG) β-glycerophosphate (2GP) hydrogels are suitable inks for printing cell-laden structures. CG-2GP solutions spontaneously form hydrogels at 37°C without needing post-processing [146]; the solution (pH=7.4) remains in liquid phase at room temperature allowing the possibility of uniform mixture of cells. It is non-

immunogenic in a mouse-transdermal model [146], supports matrix synthesis by fibroblasts [78], and has tunable mechanical properties through alteration of chitosan and gelatin concentrations and by selectively cross-linking gelatin after gelation using transglutaminase (TG) [57]. NBs were printed as vertical lines perpendicular to the application of EF after suspending in 3%-3% CG solution on a 37 °C stage and allowed to gel. Formed fibers are porous, probably due to the leaching of β-glycerophosphate. One could observe formed 3%-3% hydrogels with 160 μm fibers within which cells were dispersed (**Figure 5.4a-b**), similar to results in Chapter 3. Although fibers were stable even after six days of culture post-printing, cells did not spread and appeared circular, similar to suspended cells. In order to understand how NBs would respond to changes after bioprinting, I tested the effect of EF on printed structures. These results showed no significant changes in cell morphology after EF stimulation either after one or six days of culture. I thought that reduced spreading could be attributed to increased mechanical stiffness of the fibers and a reduced number of cell-binding domains. To test this possibility, I printed cells using 2%-8% CG solution (**Figure 5.4c-d**). Reduction in chitosan concentration is known to decrease gelation rate; this increases solution spreading. 2%-8% fibers were larger than 3%-3% fibers, with a large number of cells in the field of view under the microscope. I observed some cell spreading in 2%-8% CG hydrogel on day 6 (**Figure 5.4d**). Previously I have observed cell spreading on the surface of CG hydrogels and alignment with applied hydrodynamic shear. Nevertheless, application of EF stimulation did not alter the cellular morphology of cells encapsulated in the CG hydrogel. This indicated more than formulation alone is responsible for the observed cell shape.

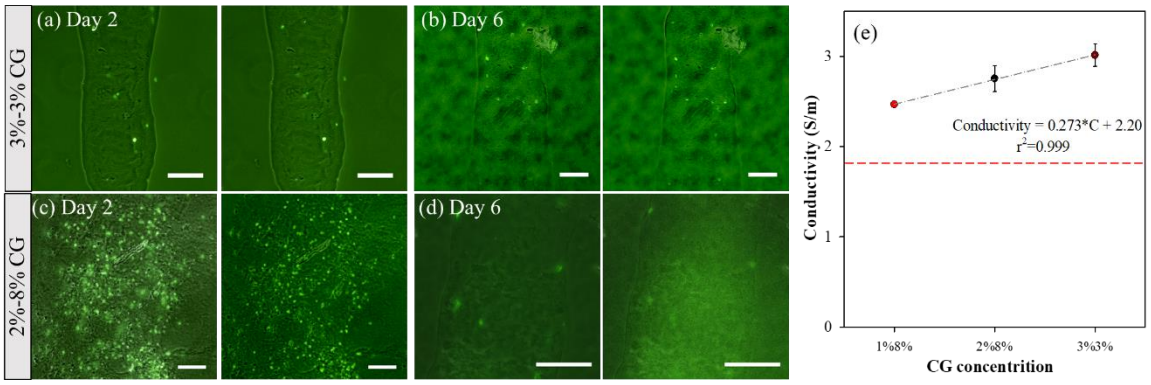

Figure 5.4: **Effect of encapsulating in the hydrogel on NB morphology**. Cells were pre-stained with non-toxic cytoplasmic stain CFDA-SE for identification within the fiber. The left image of each pair is before stimulation and the right after the end of stimulation. NB printed in 3%-3% CG hydrogel and stimulated on a) day 2 and b day 6, and NB printed in 3%-3% CG hydrogel and stimulated on c) day 2 and d) day 6. Scale bars are 100µm and current passes left to right (anode on left and on cathode right). (e) Change in conductivity for different CG formulations. Increasing concentrations of negatively charged chitosan change the conductivity of chitosan-gelatin hydrogels, while gelatin concentration does not. Data is shown as average with error bars equal to 1 standard deviation (n=3).

Since no effects were observed after EF stimulation, I questioned whether the conductive properties of the CG ink could affect the EF experienced by cells. I measured the conductivity for 1%-8%, 2%-8%, and 3%-3% CG hydrogels. A linear increase in conductivity with increased chitosan concentration was observed irrespective of gelatin concentration (**Figure 5.4e**). All concentrations of the CG hydrogels were at least 1 S/m more conductive than cell culture medium (**Figure 5.4e**). Hence, CG hydrogels are not isolating cells from the EF during exposure. These fibers are also very thin, and hence changes in EF should be negligible. In any case, the effect of altering the bioink formulation should to be tested. Laminin has been used to promote neuronal differentiation. Therefore, adding laminin to the hydrogel might demonstrate improved differentiation.

5.4 Discussion

In this work, I bioprinted neuroblasts and human adipocyte stem cells (hASC) using my custom-built bioprinter, described in Chapter 3. I printed both cells using 34g needle (60 µm internal diameter) and 32g needle (120 µm internal diameter) using culture medium and CG thermosensitive hydrogel described in Chapter 3. I cultured these cells up to six days and show that printed

hASC differentiation towards neurons using immunohistochemistry for β-III tubulin and actin. These cells are viable and there was a progressive increase in β-III tubulin expression. Printing hASC using 34g needle had more effect than 32g needle, which is remarkable given the cell size of hASC (32 to 38μm in diameter when suspended in culture medium) and short exposure time to such stress. Phenotypic changes corroborate such effects. I demonstrate that β-III-tubulin expression and galvanotactic response are affected by bioprinting. However, further studies are required to understand the functionality of differentiate stem cells via measurement of membrane potentials and the efficiency of differentiation. Needle diameter could be an important factor in cell differentiation caused by bioprinting. As new bioink formulations are explored, it might be possible to leverage bioprinting to differentiate cells in complex, printed architectures. However, it will be important to consider the nature of the inks used and post-processing effects.

I initially expected that, because there was very high cell viability, the lack of NB spreading and galvanotactic response after printing in hydrogels was a consequence of hydrogel stiffness. Supporting this hypothesis, I observed cell spreading with decreased chitosan concentration. However, I did not observe a galvanotactic response from NBs printed in hydrogel, which indicates that altered cell response caused by stresses imparted by the printing process likely impacts cell spreading, and may even be the dominant cause of the lack of galvanotaxis, not the hydrogel properties. However, exploring the hydrogel's osmolarity is also of interest: while the pH of the solution is adjusted to 7.4, which is physiologically normal, the concentration of glycerophosphate salt in the hydrogel may create a hyperosmotic environment. This may also contribute to or cause a lack of cell spreading and response due to transport of water from the cell to the hydrogel.

There is increasing interest in the use of small scale, pseudo organs for pharmacological, cancer, and functional models using bioprinting. I observe greater changes in cellular response, specifically the presence of polymerized actin, in NBs than hASCs. This indicates that post-printing functionality should be evaluated for specific cell types and applications. Moreover, contrary to

conventional wisdom, stem cells may not be the most sensitive and easily affected cell type. Considering the sensitivity of carcinoma cell lines may be important for tumor and other cancel models. This could be because time is required for cells to re-develop focal adhesions and polymerized actin filaments, possibly due to damage to integrins and other CAMs. It might also be because galvanotaxis in NBs is cell concentration dependent: cell-cell interactions may be required for NBs to detect and align to an applied EF.

5.5 Conclusions

Bioprinting research currently focuses on reducing negative impacts of the printing process on cell survival, without considering cell response as a separate evaluation criterion. In the context of my optimization of printing process in chapter 3, my results demonstrate that unwanted cell alterations (i.e. loss of response and changes expression) can be imposed upon cells by the bioprinting process, despite high cell viability. Unlike non-printed NBs, after printing in media through a 34g needle, NBs did not demonstrate polymerized actin. Nor did they express β-III-tubulin after stimulation. Moreover, while printing in media through a 32g needle demonstrated some polymerized actin and β-III-tubulin expression after printing, it appeared that expression was lower than unprinted cells. Interestingly, printing did not affect hASC actin polymerization. However, printing alone caused some hASCs to express β-III-tubulin. Based upon evidence from extended hASC culture, the printing process caused β-III-tubulin expression, which did not appear to increase with stimulation. When printed in 2%-8% CG hydrogel, cells spread very little and do not exhibit galvanotaxis. The lack of spreading and galvanotaxis may be due, in part, to shear based effects on cells. However, other factors, such as the hydrogel's stiffness and or osmolarity may also play a role.

Chapter VI

CONCLUSIONS AND RECOMMENDATIAONS

6.1 Conclusions

Bioprinting research has focused on the printability of new hydrogel-based inks, exploring the quality of 3D structures that can be produced and ensuring the processing parameters required do not adversely affect cell viability. However, there is very limited understanding of how bioprinting alters cell response; some assume that high viability infers normal function and unaltered stimulus response. Moreover, most inks require post-processing steps to stabilize the ink that may damage cells or alter their function. This work demonstrates a hydrogel that does not require post-processing and indicates that high viability does not imply unaltered stimulus response.

My work focused on bioprinting three dimensional structures from a novel chitosan-gelatin hydrogel with an unique gelation characteristic amongst explored inks, and evaluating bioprinting effects on electrical cell responses using a compact electrical stimulation device. The work was grouped into three aims: In aim 1 (Chapter III), I introduced a bioprinter ink and provided insight into the challenges and advantages of printing with an ink that has irreversible gelation with increasing temperature, neither which have been explored previously. In aim 2 (Chapter IV), I detailed the design of a compact electrical stimulation device which retains the structure of traditional stimulators while allowing sterile observation during stimulation, validated the responses of NBs in the context of work conducted in literature and further explored NB and hASC responses to a DC electrical signal and their changes in expression. In aim 3 (Chapter V), I explored how bioprinting

affected NB and hASC responses to electrical stimulation and, changes in expression of β-III-tubulin indicating differentiation towards a neural lineage.

6.1.1 Aim 1: Create a Bioprinting Process for Chitosan-Gelatin-β-glycerophosphate Thermogelling Hydrogel

In Chapter III, I described the printability of the chitosan-gelatin-β-glycerophosphate hydrogel and the effect of printing on cell viability. I developed a process to print the hydrogel using a low cost (<$800), compact 3D printer: I designed an extruder to use disposable syringes and hypodermic needles to print the hydrogel and utilized petri dishes with level cooled agarose print surfaces to overcome petri dish floor variation and maintain a constant gap with the needle tip. Further, I found that degassing and precooling the solution were necessary preparation steps to obtain continuous fibers. I found that the print surface temperature varied by up to 33°C compared to the heated plate and that the temperature profile was more constant across an agarose surface than water. While investigating fiber size parameters, I found that flow rates between 5 µL/min and 60 µL/min did not affect the fiber size. Fiber size decreased from 760µm, to 243µm as the feed rate increased from 10cm/min to 100cm/min with greater changes in fiber size at 25°C than 37°C. Increased needle height initially decreased fiber size but then increased showing an optimum. Overall, bed temperature played the greatest role in fiber size followed by feed rate. Structures approximately 1mm high were printed using 13 layers of hydrogel. Finally, cells were uniformly distributed within the fibers and exhibited high viability and no contamination after 5 days [23].

6.1.2 Aim 2: Develop a compact electric stimulation device and test the response of neuroblasts and human adipocyte stem cells

In chapter IV, I described the development of a compact electrical stimulation device that could be used to understand cell responses to electric fields after bioprinting. A compact device was developed that matches the footprint of a standard microscope slide and produces a uniform electric

field, similar to traditional electrical stimulation devices, was easy to transport, and could be observed via light microscopy during stimulation while maintaining sterility. Open devices with disk electrodes had less variation in EF and ran longer than devices with physical walls and point electrodes. Vertical NB alignment, similar to results obtained for other neural cells, was observed after six days of culture but not after one day. The electrical field effect was also evaluated on hASCs, which showed a decrease in cell area on day 1 but not day 6, indicating culture time affects cell response differentially by cell type. Further, I immunostained NBs and hASCs before and after stimulation for β-III-tubulin an early neural marker, for the cell nucleus (DAPI), and for actin (Phalloidin). I observed β-III-tubulin expression in both NBs and hASCs after stimulation. In summary, a compact device was developed to observe cells during electrical stimulation without sacrificing sterility and maintaining similarity to traditional devices. Further, the responses of NBs and hASCs demonstrate cells respond to stimulation differently based upon culture time and that electrical stimulation may differentiate both hASCs and NBs towards a neural lineage.

6.1.3 Aim 3: Evaluate the effect of bioprinting and electrical stimulation separately and jointly on NBs and hASCs

Described in chapter V, this aim sought to evaluate the combined and separate effect of bioprinting and electrical stimulation on NBs and hASCs. I demonstrated that the printing process alters cell morphology and response when printed in medium and hydrogel. When printed in medium, through a 34g needle, NBs had a shape factor closer to one with a correspondingly larger minor length, although they did not appear to be detaching because the cell height decreased. NBs did not respond to electrical stimulation; they had no significant change in any of the measured shape parameters compared to printing alone. However, when printed through a 32g needle, NBs showed some change in morphology with electrical stimulation. When printed, hASCs had significantly increased major length and responded to electrical stimulation with a decrease in area, similar to unprinted hASCs. Moreover, when stained with DAPI, phalloidin, and TUJ1, NBs did not exhibit

polymerized actin or β-III-tubulin either before or after stimulation when printed through a 34g needle. However, printing NBs in medium, through a 32g needle, restored some actin and β-III-tubulin expression, indicating that the printing process may be stripping cell adhesion molecules from the NBs during printing. Similar experiments with hASCs, showed no change in actin polymerization compared to non-printed samples before or after stimulation through both a 32g and 34g needle, despite a more than eight times greater cell volume. This indicates that bioprinting has a greater negative effect on NBs than hASCs. To explore printing in hydrogel, NBs and hASCs were printed in 2%-8% CG hydrogel due to earlier observations that cells fail to spread in 3%-3% CG hydrogels. While NB appear to spread in 2%-8% hydrogel, they do not respond to electrical stimulation. Similarly, hASCs did not show spreading in 2%-8% CG hydrogel. Finally, when I extended hASC culture to 6 days after printing or stimulation, I observed increased β-III-tubulin expression, indicating that bioprinting likely influences the differentiation of hASCs towards a neural lineage. In addition, some hASCs printed through a 34g needle exhibited a neuron-like cell morphology after 6 days. Overall, short exposure to shear stress may initiate differentiation of hASCs towards a neural lineage even without the use of neural culture or differentiation medium and a short overall culture time compared to typical two week differentiation protocols. However, either the printing process or hydrogel properties seems to prevent cell spreading in the CG hydrogel ink.

6.4 Recommendations

6.4.1 Decreasing or Eliminating Hydrogel Slumping During Bioprinting

As stated, I observed slumping in my bioprinted constructs. I envision two approaches that might eliminate or decrease this issue. If the temperature gradient can be increased the gel will move more quickly between temperatures, this is the basis of both approaches. The first approach involves the combination with a heated cell culture chamber maintained at or slightly above 37°C.

The use of a chamber would eliminate the issues with decreasing temperature in the z-axis. However, due to premature gelation concerns, a cooled syringe jacket would also be necessary to maintain the hydrogel in the syringe at a non-gelled temperature. This jacket would be more necessary with higher concentrations of chitosan and might be eliminated for gels with high gelatin content. The second approach is to take advantage of the gelation of gelatin at lower temperatures (See **Figure 3.6**) to maintain shape fidelity by printing the entire solution at or below room temperature then adding a pre-warmed, biocompatible, hydrophobic solution of medium to high viscosity. I expect that adding a pre-warmed liquid will induce a higher temperature gradient to assist gelation of the hydrogel as temperature conduction through a liquid medium is much higher than through a gas. The use of a hydrophobic liquid would prevent swelling of the hydrogel prior to gelation, while high viscosity would provide a buoyant force to counteract gravity. Post gelation, the solution would need to be removed and replaced with cell culture medium.

6.4.2 Improved Stimulation of Cells

While I was able to observe cells during stimulation, condensate accumulating on the observation window and the petri dish surfaces sometimes made observation difficult. This could be overcome by the introduction of a heated observation chamber instead of a heated build plate, which are commonly used for longer-term observation of cells.

6.4.3 Differentiation of hASCs

β-III-tubulin expression is widely used to indicate early neural differentiation. I observed β-III-tubulin expression in cells cultured for 6 days post printing. However, I did not use neurodifferentiation medium or neurobasal medium during culture. The hASCs were maintained in normal expansion medium. Utilization of a neurobasal medium might promote the growth of neuron-like cells. In addition, most neural differentiation protocols are a minimum of 2-weeks (**Table 2.5**). Hence, extending the culture to two weeks, especially in neurobasal medium would be of interest and might demonstrate an increase number of cells expressing neural markers. In addition, others

have stated that β-III-tubulin expression decreases in mature neurons and expression of other neural markers, such as PAX6 increases. Hence, immunostaining hASCs cultured for a longer duration for PAX6 expression would provide more insight into the potential of shear induced differentiation for neural culture.

6.4.4 Cell Spreading in CG Hydrogels

The lack of observed cell spreading in CG hydrogels is a limitation of the ink. I attempted to address the issue by exploring a 2%-8% chitosan-gelatin hydrogel in lieu of the 3%-3% hydrogel I initially investigated. Lowering the chitosan concentration and increasing gelatin concentration leads to larger fibers with lower shape fidelity. Moreover, I do not observe spreading of hASCs in these gels. Whether this is a result of the printing process or the properties of the gel is unclear. First, I recommend exploring large bore needles to further reduce stresses on printed cells and determine whether spreading occurs in these larger fibers and extending culture time to allow for some degradation of the gel to occur post printing. Based on previous work in our lab [147], which observed cell attachment and proliferation on CG hydrogels, the hydrogel likely does not lack attachment sites. It is also possible that my cell density is an issue and that exploring lower cell densities might result in spreading, especially for hASCs when some spreading may be observed by NB in 2%-8% hydrogel.

6.4.5 Early β-III-Tubulin Expression

The pathway responsible for β-III-tubulin expression due to bioprinting and electrical stimulation is unknown. While some central nervous system proteins experience rapid expression changes, in as little as 30 min [148], to my knowledge, the rapid expression of β-III-Tubulin (3.5 hr or 210 min), has not been explored. It is interesting that there is such early evidence of differentiation, which may warrant future exploration to understand the mechanism of expression.

REFERENCES

[1] W.H. Organization, Neurological disorders: public health challenges, World Health Organization2006.

[2] C.L. Gooch, E. Pracht, A.R. Borenstein, The burden of neurological disease in the United States: a summary report and call to action, Annals of neurology 81(4) (2017) 479-484.

[3] L.G. Griffith, M.A. Swartz, Capturing complex 3D tissue physiology in vitro, Nat Rev Mol Cell Biol 7(3) (2006) 211-24.

[4] B.C. Heng, T. Cao, L.W. Stanton, P. Robson, B. Olsen, Strategies for directing the differentiation of stem cells into the osteogenic lineage in vitro, J Bone Miner Res 19(9) (2004) 1379-94.

[5] D. Lo Furno, G. Mannino, V. Cardile, R. Parenti, R. Giuffrida, Potential Therapeutic Applications of Adipose-Derived Mesenchymal Stem Cells, Stem Cells Dev (2016).

[6] M. Mimeault, S.K. Batra, Recent progress on tissue-resident adult stem cell biology and their therapeutic implications, Stem Cell Rev. 4(1) (2008) 27-49.

[7] M. Lietz, L. Dreesmann, M. Hoss, S. Oberhoffner, B. Schlosshauer, Neuro tissue engineering of glial nerve guides and the impact of different cell types, Biomaterials 27(8) (2006) 1425-1436.

[8] N. Makdissy, K. Haddad, J.D. AlBacha, D. Chaker, B. Ismail, A. Azar, G. Oreibi, D. Ayoub, I. Achkar, D. Quilliot, Z. Fajloun, Essential role of ATP6AP2 enrichment in caveolae/lipid raft microdomains for the induction of neuronal differentiation of stem cells, Stem Cell Res Ther 9(1) (2018) 132.

[9] N.G. Durmus, S. Tasoglu, U. Demirci, Bioprinting: Functional droplet networks, Nat Mater 12(6) (2013) 478-479.

[10] T. Billiet, E. Gevaert, T. De Schryver, M. Cornelissen, P. Dubruel, The 3D printing of gelatin methacrylamide cell-laden tissue-engineered constructs with high cell viability, Biomaterials 35(1) (2014) 49-62.

[11] D.B. Kolesky, R.L. Truby, A.S. Gladman, T.A. Busbee, K.A. Homan, J.A. Lewis, 3D Bioprinting of Vascularized, Heterogeneous Cell-Laden Tissue Constructs, Advanced Materials 26(19) (2014) 3124-3130.

[12] T. Boland, T. Xu, B. Damon, X. Cui, Application of inkjet printing to tissue engineering, Biotechnology journal 1(9) (2006) 910-7.

[13] B.R. Ringeisen, C.M. Othon, J.A. Barron, D. Young, B.J. Spargo, Jet-based methods to print living cells, Biotechnology journal 1(9) (2006) 930-48.

[14] N.E. Sanjana, S.B. Fuller, A fast flexible ink-jet printing method for patterning dissociated neurons in culture, J Neurosci Methods 136(2) (2004) 151-63.

[15] R.K. Pirlo, D.M.D. Dean, D.R. Knapp, B.Z. Gao, Cell deposition system based on laser guidance, Biotechnol. J. 1 (2006) 1007-1013.

[16] S.N. Jayasinghe, P.A.M. Eagles, A.N. Qureshi, Electrohydrodynamic jet processing: an advanced electric-field-driven jetting phenomenon for processing living cells, Small 2 (2006) 216-219.

[17] J.E. Trachtenberg, P.M. Mountziaris, J.S. Miller, M. Wettergreen, F.K. Kasper, A.G. Mikos, Open-source three-dimensional printing of biodegradable polymer scaffolds for tissue

engineering, Journal of Biomedical Materials Research Part A 102(12) (2014) 4326-4335.
[18] J.D. Baranski, R.R. Chaturvedi, K.R. Stevens, J. Eyckmans, B. Carvalho, R.D. Solorzano, M.T. Yang, J.S. Miller, S.N. Bhatia, C.S. Chen, Geometric control of vascular networks to enhance engineered tissue integration and function, Proceedings of the National Academy of Sciences of the United States of America 110(19) (2013) 7586-91.
[19] S. Tasoglu, U. Demirci, Bioprinting for stem cell research, Trends Biotechnol 31(1) (2013) 10-19.
[20] N. Resnick, H. Yahav, A. Shay-Salit, M. Shushy, S. Schubert, L.C.M. Zilberman, E. Wofovitz, Fluid shear stress and the vascular endothelium: for better and for worse, Progress in Biophysics and Molecular Biology 81(3) (2003) 177-199.
[21] M.P. A. Meeson, M. Calfon, R. Lang, A relationship between apoptosis and flow during programmed capillary regression is revealed by vital analysis, Development 122(12) (1996) 3929-3938.
[22] A. Sebastian, F. Syed, D.A. McGrouther, J. Colthurst, R. Paus, A. Bayat, A novel in vitro assay for electrophysiological research on human skin fibroblasts: Degenerate electrical waves downregulate collagen I expression in keloid fibroblasts, Experimental dermatology 20(1) (2011) 64-68.
[23] L. Pan, R.B. Borgens, Strict perpendicular orientation of neural crest-derived neurons in vitro is dependent on an extracellular gradient of voltage, J Neurosci Res 90(7) (2012) 1335-46.
[24] H.F. Chang, Y.S. Lee, T.K. Tang, J.Y. Cheng, Pulsed DC Electric Field-Induced Differentiation of Cortical Neural Precursor Cells, PLoS One 11(6) (2016) e0158133.
[25] D.N. Heo, N. Acquah, J. Kim, S.J. Lee, N.J. Castro, L.G. Zhang, Directly Induced Neural Differentiation of Human Adipose-Derived Stem Cells Using Three-Dimensional Culture System of Conductive Microwell with Electrical Stimulation, Tissue Eng Part A (2017).
[26] H. Zhao, A. Steiger, M. Nohner, H. Ye, Specific intensity direct current (DC) electric field improves neural stem cell migration and enhances differentiation towards βIII-tubulin+ neurons, PloS one 10(6) (2015) e0129625.
[27] S.F. Badylak, The extracellular matrix as a biologic scaffold material, Biomaterials 28(25) (2007) 3587-3593.
[28] M. Farokhi, F. Mottaghitalab, M.A. Shokrgozar, D.L. Kaplan, H.-W. Kim, S.C. Kundu, Prospects of peripheral nerve tissue engineering using nerve guide conduits based on silk fibroin protein and other biopolymers, International Materials Reviews 62(7) (2016) 367-391.
[29] D. Arslantunali, T. Dursun, D. Yucel, N. Hasirci, V. Hasirci, Peripheral nerve conduits: technology update, Medical Devices (Auckland, NZ) 7 (2014) 405.
[30] D. Neubauer, J.B. Graham, D. Muir, Chondroitinase treatment increases the effective length of acellular nerve grafts, Experimental neurology 207(1) (2007) 163-170.
[31] M. Georgiou, S.C.J. Bunting, H.A. Davies, A.J. Loughlin, J.P. Golding, J.B. Phillips, Engineered neural tissue for peripheral nerve repair, Biomaterials 34(30) (2013) 7335-7343.
[32] A.M. McCormick, N.A. Jarmusik, N.D. Leipzig, Co-immobilization of semaphorin3A and nerve growth factor to guide and pattern axons, Acta Biomater 28 (2015) 33-44.
[33] M. Sarker, S. Naghieh, A.D. McInnes, D.J. Schreyer, X. Chen, Strategic Design and Fabrication of Nerve Guidance Conduits for Peripheral Nerve Regeneration, Biotechnol J (2018).
[34] J. Horvath, Mastering 3D Printing, Apress Media, New York, NY, 2014.
[35] J.R. Tumbleston, D. Shirvanyants, N. Ermoshkin, R. Janusziewicz, A.R. Johnson, D. Kelly, K. Chen, R. Pinschmidt, J.P. Rolland, A. Ermoshkin, Continuous liquid interface production of 3D objects, Science 347(6228) (2015) 1349-1352.
[36] G-code, 2015. http://reprap.org/wiki/G-code. (Accessed 11 Nov 2015.

[37] J. Zieverink, FDA approves the first 3D printed drug product, 2015. https://www.aprecia.com/pdf/2015_08_03_Spritam_FDA_Approval_Press_Release.pdf. (Accessed 11 Jan 2016 2016).
[38] 3D-printed skull implanted in patient, 2014. http://www.umcutrecht.nl/en/Research/News/3D-printed-skull-implanted-in-patient. (Accessed 1 Apr 2016 2016).
[39] F. Rengier, A. Mehndiratta, H. von Tengg-Kobligk, C.M. Zechmann, R. Unterhinninghofen, H.U. Kauczor, F.L. Giesel, 3D printing based on imaging data: review of medical applications, Int J Comput Assist Radiol Surg 5(4) (2010) 335-41.
[40] A. Dawood, B. Marti Marti, V. Sauret-Jackson, A. Darwood, 3D printing in dentistry, Br Dent J 219(11) (2015) 521-9.
[41] J.E. Trachtenberg, P.M. Mountziaris, J.S. Miller, M. Wettergreen, F.K. Kasper, A.G. Mikos, Open-source three-dimensional printing of biodegradable polymer scaffolds for tissue engineering, Journal of Biomedical Materials Research Part A 102(12) (2014) 4326-4335.
[42] J.Y. Kim, D.-W. Cho, Blended PCL/PLGA scaffold fabrication using multi-head deposition system, Microelectronic Engineering 86(4–6) (2009) 1447-1450.
[43] J.A. Reid, P.A. Mollica, G.D. Johnson, R.C. Ogle, R.D. Bruno, P.C. Sachs, Accessible bioprinting: adaptation of a low-cost 3D-printer for precise cell placement and stem cell differentiation, Biofabrication 8(2) (2016) 025017.
[44] Y. Zhao, Y. Li, S. Mao, W. Sun, R. Yao, The influence of printing parameters on cell survival rate and printability in microextrusion-based 3D cell printing technology, Biofabrication 7(4) (2015) 045002.
[45] W. Lee, J.C. Debasitis, V.K. Lee, J.-H. Lee, K. Fischer, K. Edminster, J.-K. Park, S.-S. Yoo, Multi-layered culture of human skin fibroblasts and keratinocytes through three-dimensional freeform fabrication, Biomaterials 30(8) (2009) 1587-1595.
[46] S. Moon, S.K. Hasan, Y.S. Song, F. Xu, H.O. Keles, F. Manzur, S. Mikkilineni, J.W. Hong, J. Nagatomi, E. Haeggstrom, A. Khademhosseini, U. Demirci, Layer by layer three-dimensional tissue epitaxy by cell-laden hydrogel droplets, Tissue engineering. Part C, Methods 16(1) (2010) 157-66.
[47] W. Lee, V. Lee, S. Polio, P. Keegan, J.H. Lee, K. Fischer, J.K. Park, S.S. Yoo, On-demand three-dimensional freeform fabrication of multi-layered hydrogel scaffold with fluidic channels, Biotechnology and bioengineering 105(6) (2010) 1178-86.
[48] K. Arcaute, B. Mann, R. Wicker, Stereolithography of Three-Dimensional Bioactive Poly(Ethylene Glycol) Constructs with Encapsulated Cells, Ann Biomed Eng 34(9) (2006) 1429-1441.
[49] B. Dhariwala, E. Hunt, T. Boland, Rapid prototyping of tissue-engineering constructs, using photopolymerizable hydrogels and stereolithography, Tissue engineering 10(9-10) (2004) 1316-1322.
[50] S.J. Bryant, C.R. Nuttelman, K.S. Anseth, Cytocompatibility of UV and visible light photoinitiating systems on cultured NIH/3T3 fibroblasts in vitro, Journal of Biomaterials Science, Polymer Edition 11(5) (2000) 439-457.
[51] F.P.W. Melchels, J. Feijen, D.W. Grijpma, A review on stereolithography and its applications in biomedical engineering, Biomaterials 31(24) (2010) 6121-6130.
[52] S.V. Murphy, A. Atala, 3D bioprinting of tissues and organs, Nat. Biotechnol. 32(8) (2014) 773-785.
[53] L. Koch, S. Kuhn, H. Sorg, M. Gruene, S. Schlie, R. Gaebel, B. Polchow, K. Reimers, S. Stoelting, N. Ma, Laser printing of skin cells and human stem cells, Tissue Engineering Part C: Methods 16(5) (2009) 847-854.
[54] A.S. Hoffman, Hydrogels for biomedical applications, Advanced Drug Delivery Reviews 64, Supplement (2002) 18-23.

[55] I. Levental, P.C. Georges, P.A. Janmey, Soft biological materials and their impact on cell function, Soft Matter 3(3) (2007) 299-306.
[56] K.J. Walker, S.V. Madihally, Anisotropic temperature sensitive chitosan-based injectable hydrogels mimicking cartilage matrix, Journal of Biomedical Materials Research Part B: Applied Biomaterials 103(6) (2015) 1149-1160.
[57] C.J. Tormos, C. Abraham, S.V. Madihally, Improving the stability of chitosan–gelatin-based hydrogels for cell delivery using transglutaminase and controlled release of doxycycline, Drug Delivery and Translational Research 5(6) (2015) 575-584.
[58] R. Landers, U. Hübner, R. Schmelzeisen, R. Mülhaupt, Rapid prototyping of scaffolds derived from thermoreversible hydrogels and tailored for applications in tissue engineering, Biomaterials 23(23) (2002) 4437-4447.
[59] X. Wang, Y. Yan, Y. Pan, Z. Xiong, H. Liu, J. Cheng, F. Liu, F. Lin, R. Wu, R. Zhang, Generation of three-dimensional hepatocyte/gelatin structures with rapid prototyping system, Tissue engineering 12(1) (2006) 83-90.
[60] R. Chang, J. Nam, W. Sun, Effects of dispensing pressure and nozzle diameter on cell survival from solid freeform fabrication-based direct cell writing, Tissue Engineering Part A 14(1) (2008) 41-48.
[61] Y. Yu, Y. Zhang, J.A. Martin, I.T. Ozbolat, Evaluation of cell viability and functionality in vessel-like bioprintable cell-laden tubular channels, Journal of biomechanical engineering 135(9) (2013) 91011.
[62] R. Gaetani, P.A. Doevendans, C.H. Metz, J. Alblas, E. Messina, A. Giacomello, J.P. Sluijter, Cardiac tissue engineering using tissue printing technology and human cardiac progenitor cells, Biomaterials 33(6) (2012) 1782-90.
[63] N.E. Fedorovich, W. Schuurman, H.M. Wijnberg, H.J. Prins, P.R. van Weeren, J. Malda, J. Alblas, W.J. Dhert, Biofabrication of osteochondral tissue equivalents by printing topologically defined, cell-laden hydrogel scaffolds, Tissue engineering. Part C, Methods 18(1) (2012) 33-44.
[64] N.E. Fedorovich, E. Kuipers, D. Gawlitta, W.J. Dhert, J. Alblas, Scaffold porosity and oxygenation of printed hydrogel constructs affect functionality of embedded osteogenic progenitors, Tissue engineering. Part A 17(19-20) (2011) 2473-86.
[65] B.A. Aguado, W. Mulyasasmita, J. Su, K.J. Lampe, S.C. Heilshorn, Improving viability of stem cells during syringe needle flow through the design of hydrogel cell carriers, Tissue Engineering Part A 18(7-8) (2011) 806-815.
[66] K.H. Kang, L.A. Hockaday, J.T. Butcher, Quantitative optimization of solid freeform deposition of aqueous hydrogels, Biofabrication 5(3) (2013) 035001.
[67] L. Ouyang, R. Yao, X. Chen, J. Na, W. Sun, 3D printing of HEK 293FT cell-laden hydrogel into macroporous constructs with high cell viability and normal biological functions, Biofabrication 7(1) (2015) 015010.
[68] Y. Zhao, R. Yao, L. Ouyang, H. Ding, T. Zhang, K. Zhang, S. Cheng, W. Sun, Three-dimensional printing of Hela cells for cervical tumor model in vitro, Biofabrication 6(3) (2014) 035001.
[69] Y. Yan, X. Wang, Y. Pan, H. Liu, J. Cheng, Z. Xiong, F. Lin, R. Wu, R. Zhang, Q. Lu, Fabrication of viable tissue-engineered constructs with 3D cell-assembly technique, Biomaterials 26(29) (2005) 5864-5871.
[70] F. Pati, J. Jang, D.-H. Ha, S. Won Kim, J.-W. Rhie, J.-H. Shim, D.-H. Kim, D.-W. Cho, Printing three-dimensional tissue analogues with decellularized extracellular matrix bioink, Nat Commun 5 (2014).
[71] D.B. Kolesky, R.L. Truby, A.S. Gladman, T.A. Busbee, K.A. Homan, J.A. Lewis, 3D bioprinting of vascularized, heterogeneous cell-laden tissue constructs, Advanced materials 26(19) (2014) 3124-30.

[72] L.E. Bertassoni, J.C. Cardoso, V. Manoharan, A.L. Cristino, N.S. Bhise, W.A. Araujo, P. Zorlutuna, N.E. Vrana, A.M. Ghaemmaghami, M.R. Dokmeci, A. Khademhosseini, Direct-write bioprinting of cell-laden methacrylated gelatin hydrogels, Biofabrication 6(2) (2014) 024105.
[73] J.H. Shim, J.Y. Kim, M. Park, J. Park, D.W. Cho, Development of a hybrid scaffold with synthetic biomaterials and hydrogel using solid freeform fabrication technology, Biofabrication 3(3) (2011) 034102.
[74] K. Schacht, T. Jungst, M. Schweinlin, A. Ewald, J. Groll, T. Scheibel, Biofabrication of cell-loaded 3D spider silk constructs, Angewandte Chemie 54(9) (2015) 2816-20.
[75] S. Feske, Calcium signalling in lymphocyte activation and disease, Nature Reviews Immunology 7(9) (2007) 690-702.
[76] H.W. Kang, S.J. Lee, I.K. Ko, C. Kengla, J.J. Yoo, A. Atala, A 3D bioprinting system to produce human-scale tissue constructs with structural integrity, Nat Biotechnol 34(3) (2016) 312-9.
[77] A. Chenite, C. Chaput, D. Wang, C. Combes, M.D. Buschmann, C.D. Hoemann, J.C. Leroux, B.L. Atkinson, F. Binette, A. Selmani, Novel injectable neutral solutions of chitosan form biodegradable gels in situ, Biomaterials 21(21) (2000) 2155-61.
[78] P. Iyer, K.J. Walker, S.V. Madihally, Increased matrix synthesis by fibroblasts with decreased proliferation on synthetic chitosan-gelatin porous structures, Biotechnol Bioeng (2011).
[79] J.T. Podichetty, P.R. Bhaskar, K. Singarapu, S.V. Madihally, Multiple approaches to predicting oxygen and glucose consumptions by HepG2 cells on porous scaffolds in an axial-flow bioreactor, Biotechnol Bioeng 112(2) (2015) 393-404.
[80] E.P. Broderick, D.M. O'Halloran, Y.A. Rochev, M. Griffin, R.J. Collighan, A.S. Pandit, Enzymatic stabilization of gelatin-based scaffolds, Journal of biomedical materials research. Part B, Applied biomaterials 72(1) (2005) 37-42.
[81] M.K. McDermott, T. Chen, C.M. Williams, K.M. Markley, G.F. Payne, Mechanical properties of biomimetic tissue adhesive based on the microbial transglutaminase-catalyzed crosslinking of gelatin, Biomacromolecules 5(4) (2004) 1270-9.
[82] S.C. Wang, T.Y.F. Low, Y. Nishimura, L. Gole, W. Yu, F. Motegi, Cortical forces and CDC-42 control clustering of PAR proteins for Caenorhabditis elegans embryonic polarization, Nat Cell Biol 19(8) (2017) 988-995.
[83] M. Levesque, R. Nerem, The elongation and orientation of cultured endothelial cells in response to shear stress, Journal of biomechanical engineering 107(4) (1985) 341-347.
[84] A.A. Lee, D.A. Graham, S.D. Cruz, A. Ratcliffe, W.J. Karlon, Fluid shear stress-induced alignment of cultured vascular smooth muscle cells, Journal of biomechanical engineering 124(1) (2002) 37-43.
[85] N.L. Tulloch, V. Muskheli, M.V. Razumova, F.S. Korte, M. Regnier, K.D. Hauch, L. Pabon, H. Reinecke, C.E. Murry, Growth of engineered human myocardium with mechanical loading and vascular coculture, Circ Res 109(1) (2011) 47-59.
[86] K.A. Barbee, P.F. Davies, R. Lal, Shear stress-induced reorganization of the surface topography of living endothelial cells imaged by atomic force microscopy, Circulation research 74(1) (1994) 163-171.
[87] H. Aubin, J.W. Nichol, C.B. Hutson, H. Bae, A.L. Sieminski, D.M. Cropek, P. Akhyari, A. Khademhosseini, Directed 3D cell alignment and elongation in microengineered hydrogels, Biomaterials 31(27) (2010) 6941-6951.
[88] C. Miller, S. Jeftinija, S. Mallapragada, Micropatterned Schwann cell-seeded biodegradable polymer substrates significantly enhance neurite alignment and outgrowth, Tissue Eng 7(6) (2001) 705-15.

[89] F. Yang, R. Murugan, S. Wang, S. Ramakrishna, Electrospinning of nano/micro scale poly(l-lactic acid) aligned fibers and their potential in neural tissue engineering, Biomaterials 26(15) (2005) 2603-2610.
[90] B. Chelli, M. Barbalinardo, F. Valle, P. Greco, E. Bystrenova, M. Bianchi, F. Biscarini, Neural cell alignment by patterning gradients of the extracellular matrix protein laminin, Interface Focus 4(1) (2014) 20130041.
[91] S. Tasoglu, U. Demirci, Bioprinting for stem cell research, Trends Biotechnol 31(1) (2013) 10-9.
[92] B. Engebretson, Z.R. Mussett, V.I. Sikavitsas, Tenocytic extract and mechanical stimulation in a tissue-engineered tendon construct increases cellular proliferation and ECM deposition, Biotechnol J 12(3) (2017).
[93] P. Mozetic, S.M. Giannitelli, M. Gori, M. Trombetta, A. Rainer, Engineering muscle cell alignment through 3D bioprinting, J Biomed Mater Res A 105(9) (2017) 2582-2588.
[94] P. Limousin, P. Krack, P. Pollak, A. Benazzouz, C. Ardouin, D. Hoffmann, A.-L. Benabid, Electrical stimulation of the subthalamic nucleus in advanced Parkinson's disease, New England Journal of Medicine 339(16) (1998) 1105-1111.
[95] K.R. Robinson, The responses of cells to electrical fields: a review, J Cell Biol 101(6) (1985) 2023-2027.
[96] K.B. Hotary, K.R. Robinson, Endogenous electrical currents and the resultant voltage gradients in the chick embryo, Developmental biology 140(1) (1990) 149-60.
[97] B. Song, M. Zhao, J. Forrester, C. McCaig, Nerve regeneration and wound healing are stimulated and directed by an endogenous electrical field in vivo, J Cell Sci 117(Pt 20) (2004) 4681-90.
[98] S.J. Pelletier, M. Lagace, I. St-Amour, D. Arsenault, G. Cisbani, A. Chabrat, S. Fecteau, M. Levesque, F. Cicchetti, The morphological and molecular changes of brain cells exposed to direct current electric field stimulation, Int J Neuropsychopharmacol 18(5) (2014).
[99] S.D. Angelov, S. Koenen, J. Jakobi, H.E. Heissler, M. Alam, K. Schwabe, S. Barcikowski, J.K. Krauss, Electrophoretic deposition of ligand-free platinum nanoparticles on neural electrodes affects their impedance in vitro and in vivo with no negative effect on reactive gliosis, J Nanobiotechnology 14 (2016) 3.
[100] A. Opitz, A. Falchier, G.S. Linn, M.P. Milham, C.E. Schroeder, Limitations of ex vivo measurements for in vivo neuroscience, Proc Natl Acad Sci U S A 114(20) (2017) 5243-5246.
[101] W. Zhu, T. Ye, S.J. Lee, H. Cui, S. Miao, X. Zhou, D. Shuai, L.G. Zhang, Enhanced neural stem cell functions in conductive annealed carbon nanofibrous scaffolds with electrical stimulation, Nanomedicine (2017).
[102] S.N. Charoensook, D.J. Williams, S. Chakraborty, K.W. Leong, G. Vunjak-Novakovic, Bioreactor model of neuromuscular junction with electrical stimulation for pharmacological potency testing, Integr Biol (Camb) 9(12) (2017) 956-967.
[103] H. Clevers, K.M. Loh, R. Nusse, An integral program for tissue renewal and regeneration: Wnt signaling and stem cell control, science 346(6205) (2014) 1248012.
[104] S. Jang, H.S. Jeong, Histone deacetylase inhibition-mediated neuronal differentiation via the Wnt signaling pathway in human adipose tissue-derived mesenchymal stem cells, Neurosci Lett 668 (2018) 24-30.
[105] P.H. Ashjian, A.S. Elbarbary, B. Edmonds, D. DeUgarte, M. Zhu, P.A. Zuk, H.P. Lorenz, P. Benhaim, M.H. Hedrick, In vitro differentiation of human processed lipoaspirate cells into early neural progenitors, Plast Reconstr Surg 111(6) (2003) 1922-31.
[106] D.N. Heo, N. Acquah, J. Kim, S.J. Lee, N.J. Castro, L.G. Zhang, Directly Induced Neural Differentiation of Human Adipose-Derived Stem Cells Using Three-Dimensional Culture System of Conductive Microwell with Electrical Stimulation, Tissue Eng Part A 24(7-8) (2018) 537-545.

[107] R. Avola, A.C.E. Graziano, G. Pannuzzo, V. Cardile, Human Mesenchymal Stem Cells from Adipose Tissue Differentiated into Neuronal or Glial Phenotype Express Different Aquaporins, Mol Neurobiol 54(10) (2017) 8308-8320.
[108] N. Amirpour, S. Razavi, E. Esfandiari, B. Hashemibeni, M. Kazemi, H. Salehi, Hanging drop culture enhances differentiation of human adipose-derived stem cells into anterior neuroectodermal cells using small molecules, Int J Dev Neurosci 59 (2017) 21-30.
[109] S.Y. Park, J. Park, S.H. Sim, M.G. Sung, K.S. Kim, B.H. Hong, S. Hong, Enhanced differentiation of human neural stem cells into neurons on graphene, Adv Mater 23(36) (2011) H263-7.
[110] Y.C. Chan, S. Ting, Y.K. Lee, K.M. Ng, J. Zhang, Z. Chen, C.W. Siu, S.K. Oh, H.F. Tse, Electrical stimulation promotes maturation of cardiomyocytes derived from human embryonic stem cells, J Cardiovasc Transl Res 6(6) (2013) 989-99.
[111] M. Yamada, K. Tanemura, S. Okada, A. Iwanami, M. Nakamura, H. Mizuno, M. Ozawa, R. Ohyama-Goto, N. Kitamura, M. Kawano, K. Tan-Takeuchi, C. Ohtsuka, A. Miyawaki, A. Takashima, M. Ogawa, Y. Toyama, H. Okano, T. Kondo, Electrical stimulation modulates fate determination of differentiating embryonic stem cells, Stem Cells 25(3) (2007) 562-70.
[112] L. Jaatinen, S. Salemi, S. Miettinen, J. Hyttinen, D. Eberli, The combination of electric current and copper promotes neuronal differentiation of adipose-derived stem cells, Ann Biomed Eng 43(4) (2015) 1014-23.
[113] K.H. Bae, L.-S. Wang, M. Kurisawa, Injectable biodegradable hydrogels: progress and challenges, Journal of Materials Chemistry B 1(40) (2013) 5371-5388.
[114] T. Billiet, M. Vandenhaute, J. Schelfhout, S. Van Vlierberghe, P. Dubruel, A review of trends and limitations in hydrogel-rapid prototyping for tissue engineering, Biomaterials 33(26) (2012) 6020-6041.
[115] Z. Xia, M. Patchan, J. Maranchi, J. Elisseeff, M. Trexler, Determination of crosslinking density of hydrogels prepared from microcrystalline cellulose, Journal of Applied Polymer Science 127(6) (2013) 4537-4541.
[116] K. Pataky, T. Braschler, A. Negro, P. Renaud, M.P. Lutolf, J. Brugger, Microdrop Printing of Hydrogel Bioinks into 3D Tissue-Like Geometries, Advanced materials 24(3) (2012) 391-396.
[117] E. Hoch, T. Hirth, G.E.M. Tovar, K. Borchers, Chemical tailoring of gelatin to adjust its chemical and physical properties for functional bioprinting, Journal of Materials Chemistry B 1(41) (2013) 5675-5685.
[118] A. Tirella, A. Orsini, G. Vozzi, A. Ahluwalia, A phase diagram for microfabrication of geometrically controlled hydrogel scaffolds, Biofabrication 1(4) (2009) 045002.
[119] S. Khalil, W. Sun, Bioprinting Endothelial Cells With Alginate for 3D Tissue Constructs, Journal of Biomechanical Engineering 131(11) (2009) 111002-111002.
[120] L.S. Moreira Teixeira, J. Feijen, C.A. van Blitterswijk, P.J. Dijkstra, M. Karperien, Enzyme-catalyzed crosslinkable hydrogels: Emerging strategies for tissue engineering, Biomaterials 33(5) (2012) 1281-1290.
[121] W. Schuurman, P.A. Levett, M.W. Pot, P.R. van Weeren, W.J.A. Dhert, D.W. Hutmacher, F.P.W. Melchels, T.J. Klein, J. Malda, Gelatin-Methacrylamide Hydrogels as Potential Biomaterials for Fabrication of Tissue-Engineered Cartilage Constructs, Macromolecular Bioscience 13(5) (2013) 551-561.
[122] Y. Huang, S. Onyeri, M. Siewe, A. Moshfeghian, S.V. Madihally, In vitro characterization of chitosan–gelatin scaffolds for tissue engineering, Biomaterials 26(36) (2005) 7616-7627.
[123] Y. Huang, S. Onyeri, M. Siewe, A. Moshfeghian, S.V. Madihally, In vitro characterization of chitosan-gelatin scaffolds for tissue engineering, Biomaterials 26(36) (2005) 7616-27.

[124] K.J. Walker, S.V. Madihally, Anisotropic temperature sensitive chitosan-based injectable hydrogels mimicking cartilage matrix, Journal of biomedical materials research. Part B, Applied biomaterials (2014).
[125] S.V. Murphy, A. Atala, 3D bioprinting of tissues and organs, Nature biotechnology 32(8) (2014) 773-85.
[126] Epoxy Technology, Removing Bubbles from Epoxy, 2009. http://www.epotek.com/site/files/Techtips/pdfs/tip4.pdf. (Accessed 13 June 2016).
[127] J. Ngoenkam, A. Faikrua, S. Yasothornsrikul, J. Viyoch, Potential of an injectable chitosan/starch/β-glycerol phosphate hydrogel for sustaining normal chondrocyte function, International Journal of Pharmaceutics 391(1–2) (2010) 115-124.
[128] L. Ouyang, R. Yao, Y. Zhao, W. Sun, Effect of bioink properties on printability and cell viability for 3D bioplotting of embryonic stem cells, Biofabrication 8(3) (2016) 035020.
[129] BioBots, What will you build?, 2016. https://www.biobots.io/biobot-1/. (Accessed 17 Jun 2016 2016).
[130] I.T. Ozbolat, Y. Yu, Bioprinting toward organ fabrication: challenges and future trends, Biomedical Engineering, IEEE Transactions on 60(3) (2013) 691-699.
[131] N.A. Sears, D.R. Seshadri, P.S. Dhavalikar, E. Cosgriff-Hernandez, A Review of Three-Dimensional Printing in Tissue Engineering, Tissue Engineering Part B: Reviews (2016).
[132] S. Mobini, L. Leppik, V. Thottakkattumana Parameswaran, J.H. Barker, In vitro effect of direct current electrical stimulation on rat mesenchymal stem cells, PeerJ 5 (2017) e2821.
[133] J. Zhang, M. Li, E.-T. Kang, K.G. Neoh, Electrical stimulation of adipose-derived mesenchymal stem cells in conductive scaffolds and the roles of voltage-gated ion channels, Acta biomaterialia 32 (2016) 46-56.
[134] S. Mobini, L. Leppik, J.H. Barker, Direct current electrical stimulation chamber for treating cells in vitro, BioTechniques 60(2) (2016) 95-98.
[135] Y. Huang, X.B. Wang, F.F. Becker, P.R. Gascoyne, Introducing dielectrophoresis as a new force field for field-flow fractionation, Biophysical Journal 73(2) (1997) 1118-1129.
[136] W.Y. Gu, H. Yao, A.L. Vega, D. Flagler, Diffusivity of Ions in Agarose Gels and Intervertebral Disc: Effect of Porosity, Ann. Biomed. Eng. 32(12) (2004) 1710-1717.
[137] T. Oi, K. Shinyama, S. Fujita, Electrical properties of heat-treated polylactic acid, Electrical Engineering in Japan 180(1) (2012) 1-8.
[138] Y. Huang, M. Siewe, S.V. Madihally, Effect of spatial architecture on cellular colonization, Biotechnology and Bioengineering 93(1) (2006) 64-75.
[139] A.N. Koppes, K.W. Keating, A.L. McGregor, R.A. Koppes, K.R. Kearns, A.M. Ziemba, C.A. McKay, J.M. Zuidema, C.J. Rivet, R.J. Gilbert, D.M. Thompson, Robust neurite extension following exogenous electrical stimulation within single walled carbon nanotube-composite hydrogels, Acta Biomaterialia 39 (2016) 34-43.
[140] N. Tandon, C. Cannizzaro, P.-H.G. Chao, R. Maidhof, A. Marsano, H.T.H. Au, M. Radisic, G. Vunjak-Novakovic, Electrical stimulation systems for cardiac tissue engineering, Nature protocols 4(2) (2009) 155.
[141] R. Pomfret, K. Sillay, G. Miranpuri, Investigation of the electrical properties of agarose gel: characterization of concentration using nyquist plot phase angle and the implications of a more comprehensive in vitro model of the brain, Ann Neurosci 20(3) (2013) 99-107.
[142] B. Song, Y. Gu, J. Pu, B. Reid, Z. Zhao, M. Zhao, Application of direct current electric fields to cells and tissues in vitro and modulation of wound electric field in vivo, Nature Protocols 2 (2007) 1479.
[143] M. Krishnamoorthy, S. Hakobyan, M. Ramstedt, J.E. Gautrot, Surface-Initiated Polymer Brushes in the Biomedical Field: Applications in Membrane Science, Biosensing, Cell Culture, Regenerative Medicine and Antibacterial Coatings, Chemical Reviews 114(21) (2014) 10976-11026.

[144] K.D. Roehm, S.V. Madihally, Bioprinted chitosan-gelatin thermosensitive hydrogels using an inexpensive 3D printer, Biofabrication 10(1) (2018) 015002.
[145] M.G. Bixel, A.P. Kusumbe, S.K. Ramasamy, K.K. Sivaraj, S. Butz, D. Vestweber, R.H. Adams, Flow Dynamics and HSPC Homing in Bone Marrow Microvessels, Cell Reports 18(7) (2017) 1804-1816.
[146] K.J. Walker, S.V. Madihally, Anisotropic temperature sensitive chitosan-based injectable hydrogels mimicking cartilage matrix, Journal of biomedical materials research. Part B, Applied biomaterials 103(6) (2015) 1149-60.
[147] P. Iyer, K.J. Walker, S.V. Madihally, Increased matrix synthesis by fibroblasts with decreased proliferation on synthetic chitosan–gelatin porous structures, Biotechnology and bioengineering 109(5) (2012) 1314-1325.
[148] K.R. Mifsud, E.A. Saunderson, H. Spiers, S.D. Carter, A.F. Trollope, J. Mill, J.M. Reul, Rapid down-regulation of glucocorticoid receptor gene expression in the dentate gyrus after acute stress in vivo: role of DNA methylation and microRNA activity, Neuroendocrinology 104(2) (2017) 157-169.

APPENDIX A

OVERVIEW OF MATTER CONTROL SOFTWARE

The Maker's Tool Works MiniMax is operated by the MatterControl Software found on the desk-top. Below is the screen first seen when the software is opened. Note that a print is already queued for printing; it is important this print is removed from the print queue. If the software does not automatically connect to the printer the power button will say "CONNECT" instead of "DISCONNECT" and the user needs to connect the printer.

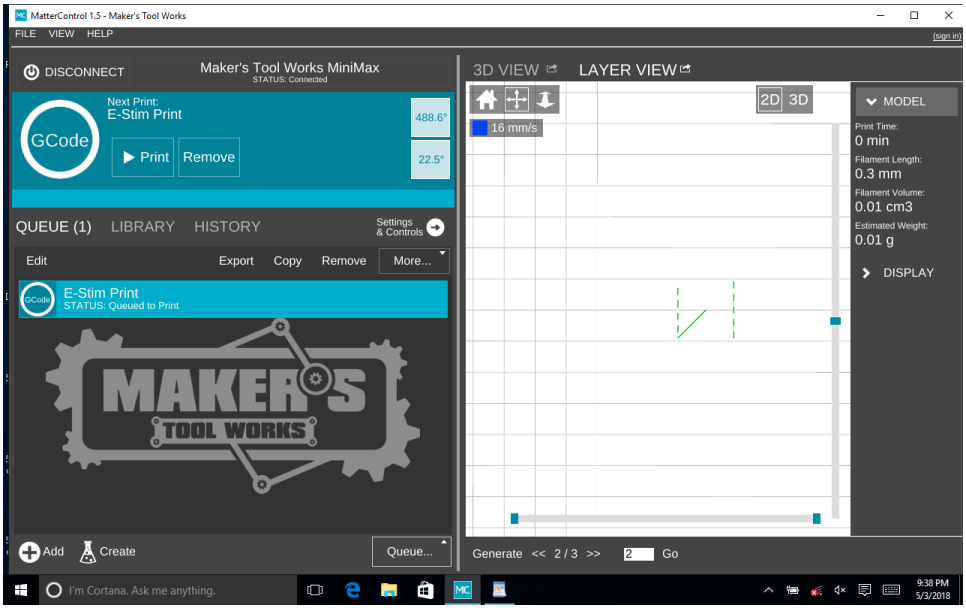

Tap “Settings and Controls” to display the screen below

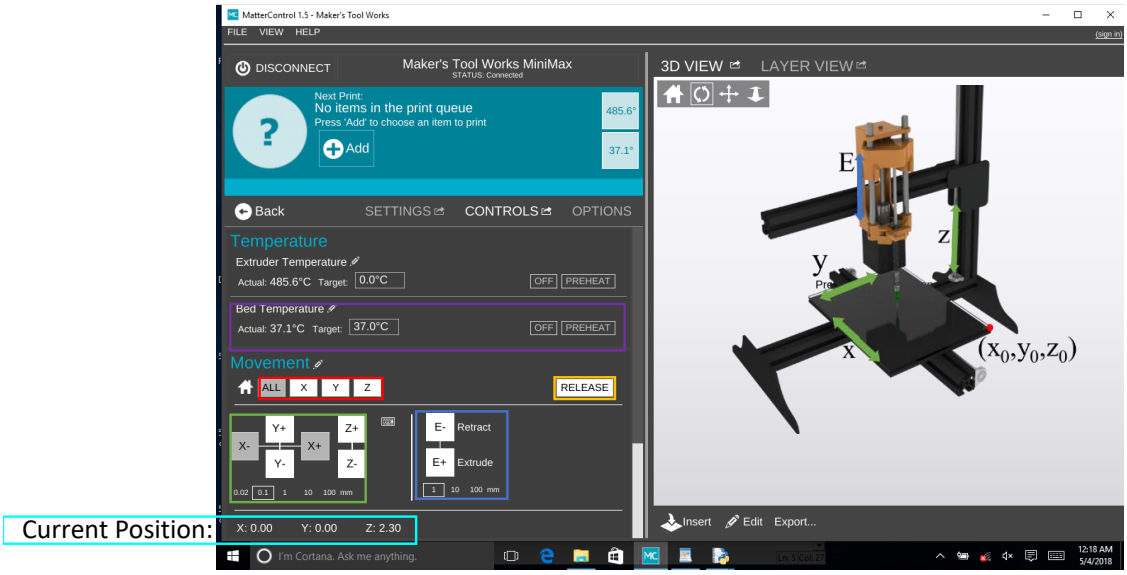

Current Position:

The manual controls are outlined in colored boxes:

- Red: Home to origin
- Green: Controls for movement of the print head in the y and z axis and the build plate in the x-axis, at bottom is the movement resolution per button press (Currently set to 0.1mm movement per press).
- Blue: Controls movement of the presser plate (**CAUTION**: The presser plate motor does not have hard or soft stops—nothing prevents the user, or control program, from damaging the extruder—make sure to never move the presser plate up or down further than physically possible. Pay special attention to the movement resolution and immediately cut power to the printer if the plate looks like it is going to run into the surrounding material)
- Yellow: removes power from the stepper motors allowing the user to move components by hand (useful if you cannot move the extruder or .
- Purple: Hotplate/Bed Temperature controls: preheat sets the temperature to 37°C, any temperature can by typed into the target box. Printing will **not** begin until the printer has reached the set temperature called for by g-code.
- Cyan: The current position of the print head. This is only accurate after homing the respective axis (ie, if you press the Z home to origin, once the print head moves to the stop and stops moving, then the z axis measurement position will be reported correctly)

APPENDIX B

CREATING STRUCTURES WITH THE PYTHON SCRIPT

The latest Python scripts are located on the desktop in the "New G-Code Generator 3" folder. "Runner.py" and "E-Stim Scaffold.py" can be run to directly create a scaffold. Other files are called by these main scripts and cannot be run directly, separating these python files is likely to break the system and cause errors. To open a file, right click on it and select "Edit with IDLE."

Within the "runner.py" file, numerous code blocks create many different gcode files. You can comment out or uncomment blocks you are interested in using Format->Comment out Region and Format->Uncomment Region. Commented regions appear in red and will be ignored by the code. Also, be aware that white space is important in Python, altering the number of spaces or tabs within files can cause compiler issues (the program won't run).

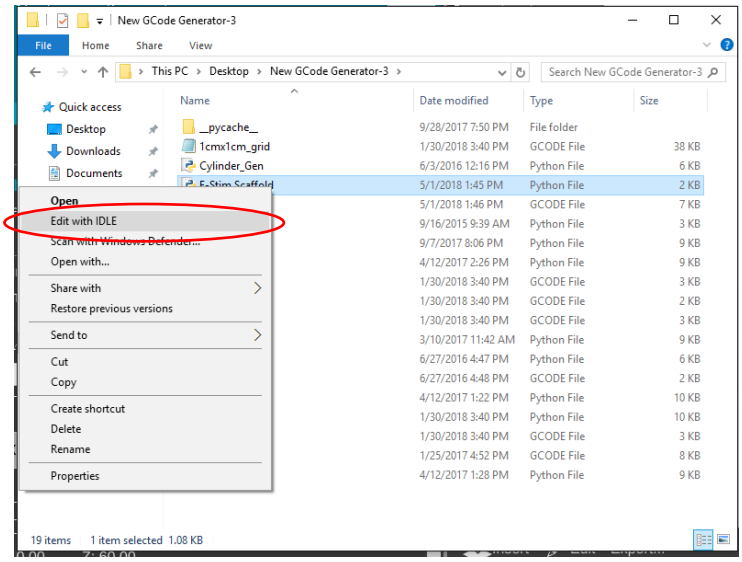

Once a file is opened, text will be presented to the user as shown below:

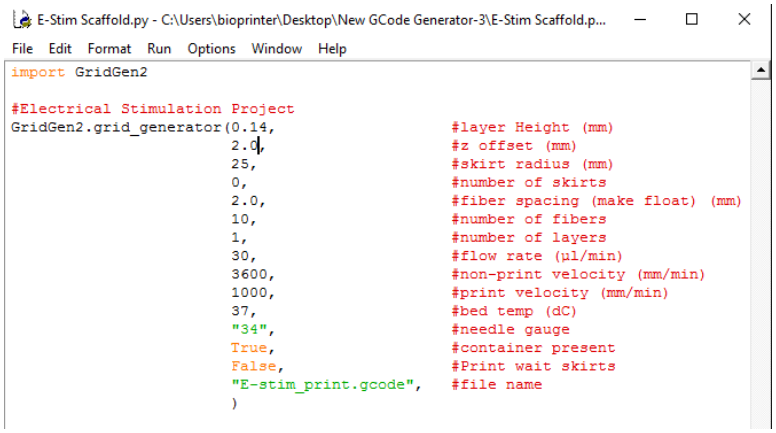

Here various parameters can be changed based on printing needs (make sure not to enter integers for floats, ie 2.0, not 2). Typically, only the z offset will need to be changed. To create the scaffold, either press F5, or choose Run->Run Module. This will create a g-code file with the given name (bottom input in figure above). You should see an additional window with the following information:

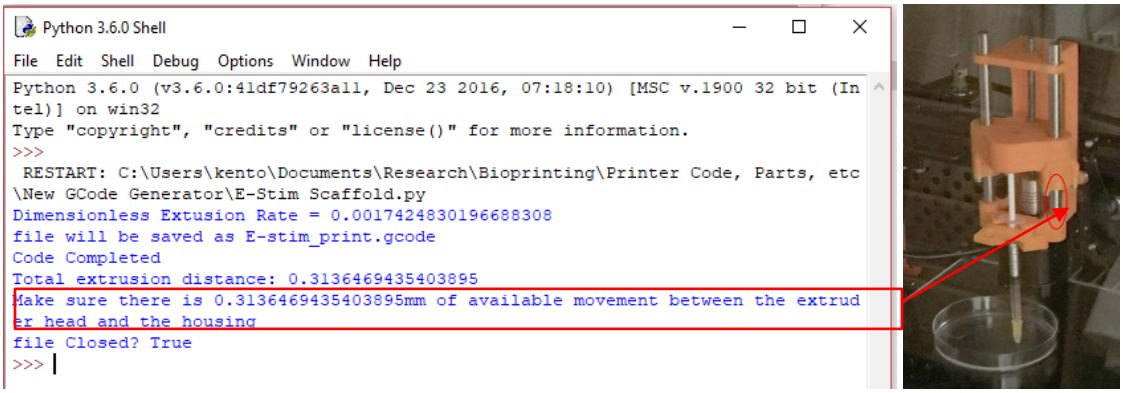

If you don't see "Code Completed" and " File Closed? True," something likely went wrong in the code.

CAUTION: Ensure that the amount of silver rod showing is greater than the total extrusion distance given in the code output (as shown in the figures above). Nothing will prevent the printer from running the presser plate into the housing and damaging the printer! **A collision will occur well before the syringe is empty**.

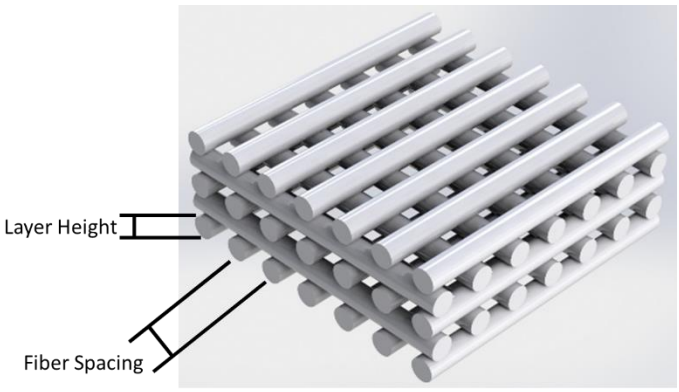

Property	Function
Layer height	Tells the print head how much to move in the z-axis between layers (does not equal the fiber height due to gelation and settling)
Z offset	Moves the Z=0 plane by the offset amount, critical for ensuring the needle is barely above the print surface (petri dish or 6 well plate)
Skirt radius	Radius of concentric circle to print before printing the scaffold. Used to ensure flow is initiated and consistent prior to printing
Number of skirts	How many of the concentric circles to print, increased skirts increases the amount of printing done before printing the actual scaffold.
Fiber spacing	The center to center distance between fibers (shown in figure above)
Number of fibers	The total number of lines to print per layer (7 in the example cartoon above)
Number of layers	the number of consecutive layers, 5 in the example cartoon. Each successive layer will print fibers orthogonal to the previous layer
Flow rate	The flow rate of hydrogel through the needle
Non-print velocity	The velocity the print head (feed rate) moves across the bed when not printing (eg between printing each fiber layer)
Print velocity	The velocity the print head (feed rate) moves across the bed when printing (eg when printing each fiber layer)
Bed temp	The temperature to set the bed/hotplate
Needle gauge	Not important, legacy parameter
Container present	Boolean (T/F) whether to move up and down to avoid the walls of a container
Print wait skirts	Will print skirts after printing each layer. Intended to decrease slumping by increasing the time before more material is deposited on the structure.
File name	Output filename, make sure it has .gcode. File will always output to the location of the python file.

APPENDIX C

PRINTING PROTOCOL

To print a structure, follow the following protocol: This protocol includes steps for printing cells in sterile conditions.

Make sure all needles have been autoclaved and that plates have been prepared to print on according to previous papers etc.

1. Place the printer into the laminar, cell culture hood. And start the hood according to lab protocol (**Do not plug the printer into power to prevent electrocution in following steps**).
2. Thoroughly mist the printer and cell culture floor with 70% isopropanol (IPA), do not un-screw the spray cap too far or it will spray a jet which may cause damage to components.
3. Leave the printer under UV for 40min to allow complete evaporation of IPA and for better 'sterilization'
4. Plug the printer in, zero the z-axis, then raise the print head ~60mm
5. Subculture and count cells as per manufacturer protocol, aliquot $2x10^6$ cells/ml to match final prepared hydrogel volume. For example, for a 2-8 gel use 0.9mL of precursor solution and add 0.4mL of β-glycerophosphate (2GP)

$$0.9mL + 0.4mL = 1.3mL$$

$$2 \times 10^6 \frac{cells}{ml} \cdot 1.3mL = 2.6 \times 10^6 cells$$

6. Pellet aliquotted cells as per manufacturer protocol, then mix hydrogel:
    a. Aliquot ~2mL of precursor solution and centrigure for 90s at 14,600xg
    b. Remove supernatant to new tube with 1mL syringe (do this slowly)
    c. Mix 2Gp into precursor solution with custom sprinkler needle
    d. Centrifuge at 3000xg for 3-3/4-4 hydrogel, or 14,600xg for a 2-8 gel if lab temp is low, for 60s
7. Aspirate media from pellet using a 1000µL pipetted, then use the mini-vortexer with a ribbed plate to re=suspend the minimum volume cell pellet.
8. Add the pellet to the hydrogel with a 100µL pipette, pellet volume should be ~30µL (be careful not to create bubbles)
9. Load the hydrogel into a syringe (do this very slowly so that the hydrogel is continuous without breaks), add a needle and either heat the solution for 5min for a 2-8 gel with cool ambient temperature, or cool the solution for 5 min for a 3-3 or 4-4 hydrogel with warm ambient temperatures in the lab.

10. Pre-Heat the Print Bed (See Appendix A for a description of the hotplate controls)
11. Place the syringe into the print head and prime the syringe
    a. In the MatterControl software, ensure the extruder step is set to 1mm (lower red circle in following image; see Appendix A for a more detailed explanation of the software)
    b. Press the "E+" extrude button until the presser plate moves down and into contact with the syringe plunger
    c. Press the "E+" extrude button a few more times, pausing for at least 1s between presses. When flow is observed from the needle, press the "E-" retract button once to remove pressure from the syringe

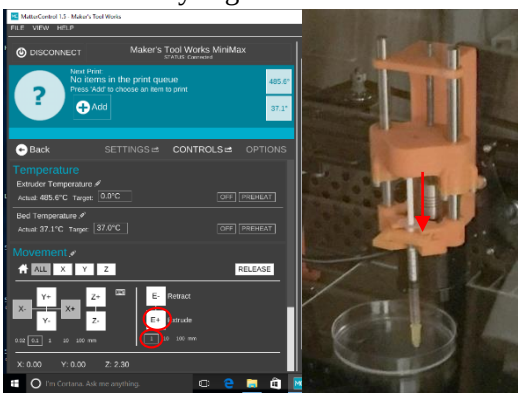

12. By hand, position the print head over either an agarose filled petri dish, 6-well plate with coverslip, etc. (if the print head and bed won't move, press the release button) use the "Z-" button to move the print head down.
    a. Move the print head down to 10mm then move it down 1mm at a time (by changing the movement resolution; see Appendix A for explanation) until the needle is close to the print surface, then change the resolution to 0.1mm.
    b. Lower the print head until the syringe needle barely moves across the print surface without either cutting into the agarose or getting caught/scratching the coverslip.
    c. When the needle cuts into the agarose or catches, raise the print head with the "Z+" command until it no longer does so.
13. Use the current z position (shown at the bottom of the matter-control screen) to set the z-offset in the python script and run the script to create g-code for the current print (See Appendix B).
    a. Note: when first learning I recommend you use the "print minimum of 300,000 cells (greater size and extrusion amnt)" code section which generates the file "1cmx1cm_grid.gcode." This file will work with an agarose filled 10cm petri dish.
14. Drag and drop the file you just created into the MatterControl software (you should see the filename as shown below), move the print head up to clear whatever dish is being used (>20mm), and home the x and y axes:

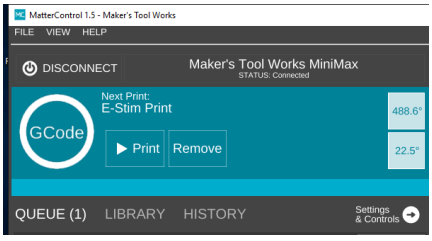

CAUTION: Ensure that the amount of silver rod showing is greater than the total extrusion distance given in the code output (see Appendix B for a more detailed explanation)

15. Re-prime the syringe as described above, EXCEPT do not retract the presser plate, allow the syringe to continue flowing as you begin the print.
16. Press Print. The printer should begin moving immediately if you pre-heated the bed per step 10

CAUTION: Be careful where you put your hands when the printer is moving.

17. Align the printing dish under the needle when it centers and begins lowering and tape the dish in place (if necessary)
18. Once the print completes, place the structure in the incubator to allow gelation (30-60min) then add medium and place the structure back into the incubator for further experimentation/analysis.

APPENDIX D

TROUBLESHOOTING

Issue	Solution
Flow stops during printing	• Solution may be too cold/hot, remove syringe and cool or heat • Needle likely also clogged or may be clogged independently. Attempt printing with a new needle.
3%-3% or 4%-4% solution will not print	• Solution too warm, cool
2%-8% solution will not print	• Solution too cool, warm in incubator
2%-8% solution too viscous to uptake with syringe after mixing 2GP	• Ambient temperature not conducive to printing, preheat 2%-8% precursor solution prior to mixing
Needle cuts or runs into print surface for part of print	• Printer bed may not be level, re-level bed • Agarose may not have been poured on a level surface, ensure agarose cools on level plate.

VITA

Kevin D. Roehm

Candidate for the Degree of

Doctor of Philosophy

Thesis: BIOPRINITNG CELL LADEN STRUCTURES WITH CHITOSAN GELATIN FOR NUERAL TISSUE APPLICATIONS

Major Field: Chemical Engineering

Biographical:

Education:

Completed the requirements for the Doctor of Philosophy in Chemical Engineering at Oklahoma State University, Stillwater, Oklahoma in July, 2018.

Completed the requirements for the Master of Science in Chemical Engineering at Oklahoma State University, Stillwater, Oklahoma in 2014.

Completed the requirements for the Bachelor of Science in Biosystems Engineering at Oklahoma State University, Stillwater, Oklahoma in 2013.

Experience:

- Teaching Assistant, Oklahoma State University, 2013-2018
- Research Assistant, Oklahoma State University, August-December 2016
- Engineering Intern, Orthocare Innovations LLC, May-August 2012

Professional Memberships:

- Tissue Engineering and Regenerative Medicine International Society
- Society for Biomaterials
- Phi Kappa Phi Honor Society
- Omega Chi Epsilon Honor Society
- Alpha Epsilon Honor Society
- Graduate and Professional Student Government Association
- Chemical Engineering Graduate Student Association